



저작자표시-비영리-변경금지 2.0 대한민국

이용자는 아래의 조건을 따르는 경우에 한하여 자유롭게

- 이 저작물을 복제, 배포, 전송, 전시, 공연 및 방송할 수 있습니다.

다음과 같은 조건을 따라야 합니다:



저작자표시. 귀하는 원저작자를 표시하여야 합니다.



비영리. 귀하는 이 저작물을 영리 목적으로 이용할 수 없습니다.



변경금지. 귀하는 이 저작물을 개작, 변형 또는 가공할 수 없습니다.

- 귀하는, 이 저작물의 재이용이나 배포의 경우, 이 저작물에 적용된 이용허락조건을 명확하게 나타내어야 합니다.
- 저작권자로부터 별도의 허가를 받으면 이러한 조건들은 적용되지 않습니다.

저작권법에 따른 이용자의 권리는 위의 내용에 의하여 영향을 받지 않습니다.

이것은 [이용허락규약\(Legal Code\)](#)을 이해하기 쉽게 요약한 것입니다.

[Disclaimer](#)

Doctoral Thesis

Learning-based Reconfigurable Readout Integrated  
Circuit and Interface for Multi-Sensor Systems

Kyeonghwan Park

Department of Electrical Engineering

Graduate School of UNIST

2019

# Learning-based Reconfigurable Readout Integrated Circuit and Interface for Multi-Sensor Systems

Kyeonghwan Park

Department of Electrical Engineering

Graduate School of UNIST

# Learning-based Reconfigurable Readout Integrated Circuit and Interface for Multi-Sensor Systems

A thesis/dissertation

submitted to the Graduate School of UNIST

in partial fulfillment of the

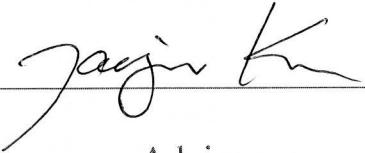
requirements for the degree of

Doctor of Philosophy

Kyeonghwan Park

06/04/2019 of submission

Approved by



---

Advisor

Jae Joon Kim

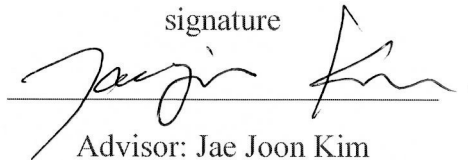
# Learning-based Reconfigurable Readout Integrated Circuit and Interface for Multi-Sensor Systems

Kyeonghwan Park

This certifies that the thesis/dissertation of Kyeonghwan Park is  
approved.

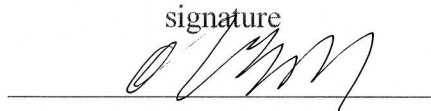
06/04/2019 of submission

signature



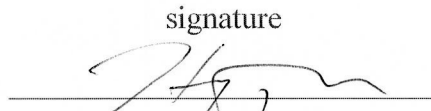
Advisor: Jae Joon Kim

signature



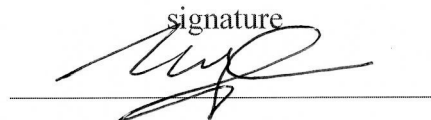
Thesis Committee Member #1: Yunsik Lee

signature



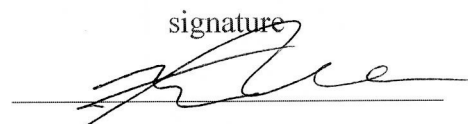
Thesis Committee Member #2: Heungjoo Shin

signature



Thesis Committee Member #3: Jeong Min Baik

signature



Thesis Committee Member #4: Hoon Eui Jeong

## Abstract

A Sensor system is advanced along sensor technologies are developed. The performance improvement of sensor system can be expected by using the internet of things (IoT) communication technology and artificial neural network (ANN) for data processing and computation. Sensors or systems exchanged the data through this wireless connectivity, and various systems and applications are possible to implement by utilizing the advanced technologies. And the collected data is computed using by the ANN and the efficiency of system can be also improved.

Gas monitoring system is widely need from the daily life to hazardous workplace. Harmful gas can cause a respiratory disease and some gas include cancer-causing component. Even though it may cause dangerous situation due to explosion. There are various kinds of hazardous gas and its characteristics that effect on human body are different each gas. The optimal design of gas monitoring system is necessary due to each gas has different criteria such as the permissible concentration and exposure time. Therefore, in this thesis, conventional sensor system configuration, operation, and limitation are described and gas monitoring system with wireless connectivity and neural network is proposed to improve the overall efficiency.

As I already mentioned above, dangerous concentration and permissible exposure time are different depending on gas types. During the gas monitoring, gas concentration is lower than a permissible level in most of case. Thus, the gas monitoring is enough with low resolution for saving the power consumption in this situation. When detecting the gas, the high-resolution is required for the accurate concentration detecting. If the gas type is varied in the above situation, the amount of calculation increases exponentially. Therefore, in the conventional systems, target specifications are decided by the highest requirement in the whole situation, and it occurs increasing the cost and complexity of readout integrated circuit (ROIC) and system. In order to optimize the specification, the ANN and adaptive ROIC are utilized to compute the complex situation and huge data processing.

Thus, gas monitoring system with learning-based algorithm is proposed to improve its efficiency. In order to optimize the operation depending on situation, dual-mode ROIC that monitoring mode and precision mode is implemented. If the present gas concentration is decided to safe, monitoring mode is operated with minimal detecting accuracy for saving the power consumption. The precision mode is switched when the high-resolution or hazardous situation are detected. The additional calibration circuits are necessary for the high-resolution implementation, and it has more power consumption and

design complexity. A high-resolution Analog-to-digital converter (ADC) is kind of challenges to design with efficiency way. Therefore, in order to reduce the effective resolution of ADC and power consumption, zooming correlated double sampling (CDS) circuit and prediction successive approximation register (SAR) ADC are proposed for performance optimization into precision mode.

A Microelectromechanical systems (MEMS) based gas sensor has high-integration and high sensitivity, but the calibration is needed to improve its low selectivity. Conventionally, principle component analysis (PCA) is used to classify the gas types, but this method has lower accuracy in some case and hard to verify in real-time. Alternatively, ANN is powerful algorithm to accurate sensing through collecting the data and training procedure and it can be verified the gas type and concentration in real-time. ROIC was fabricated in complementary metal-oxide-semiconductor (CMOS) 180-nm process and then the efficiency of the system with adaptive ROIC and ANN algorithm was experimentally verified into gas monitoring system prototype. Also, Bluetooth supports wireless connectivity to PC and mobile and pattern recognition and prediction code for SAR ADC is performed in MATLAB. Real-time gas information is monitored by Android-based application in smartphone. The dual-mode operation, optimization of performance and prediction code are adjusted with microcontroller unit (MCU). Monitoring mode is improved by x2.6 of figure-of-merits (FoM) that compared with previous resistive interface.

**Keywords:** Gas-sensor system, Learning-based optimization, Prediction SAR ADC, Self-calibration scheme, CDS zooming, Resistive sensor.





## Contents

I. Introduction .....	1
1.1 Sensor System .....	1
1.2 Artificial neural network and Learning-based algorithm .....	4
II. Background .....	6
2.1 Reconfigurable Display-based system .....	8
2.1.1 Reconfigurable multi-sensor readout structure .....	8
2.1.2 Multiple digital conversion methodology .....	10
2.1.3 Summary .....	14
2.2 Analog-to-digital Converter .....	16
2.2.1 ADC overview .....	17
2.2.2 Architecture .....	23
2.2.3 Improvement methodologies of SAR ADC .....	34
2.3 Prior arts of gas sensor system .....	39
III. Readout Integrated Circuit and system implementation .....	43
3.1 Successive Approximation Register Analog-to-Digital Converter .....	45
3.2 Correlated Double Sampling .....	48
3.3 Resistance-to-Digital Converter .....	50
3.3.1 Resistive DAC .....	52
3.3.2 Current DAC .....	53

3.4 Proposed Gas monitoring system .....	54
3.4.1 System Architecture.....	56
3.4.2 Dual-mode ROIC implementation .....	59
3.4.3 Prediction SAR algorithm .....	65
3.4.4 Pattern recognition .....	67
IV. Experimental Results .....	69
4.1 System prototype .....	70
4.2 Dual-mode ROIC performance.....	72
4.3 Prediction SAR algorithm with gas injection .....	76
4.4 Pattern recognition with artificial neural network .....	79
4.5 Summary .....	81
V. Conclusion .....	83

## List of Figures

- Fig. 1.** Conventional sensor system configuration with application devices.
- Fig. 2.** Requirement of reconfigurable gas sensor system for efficient operation.
- Fig. 3.** Artificial neural network computation algorithm.
- Fig. 4.** A block diagram of the proposed reconfigurable readout integrated circuit.
- Fig. 5.** Amplifier-based multi-sensor interface configuration.
- Fig. 6.** Oscillator-based multi-sensor interface configuration.
- Fig. 7.** Alternate sampling algorithm for SAR ADC.
- Fig. 8.** Alternate-sampling error correction scheme with example data.
- Fig. 9.** Measured 262144-point FFT spectrums at 1.777 kHz input (a) without / (b) with alternate sampling and error correction scheme.
- Fig. 10.** The block diagram of the analog-to-digital converter system.
- Fig. 11.** The characteristics of each ADC architecture: sampling rate vs resolution.
- Fig. 12.** The DC characteristics of ADC: Differential nonlinearity and Integral nonlinearity.
- Fig. 13.** The main conversion errors : (a) offset error (b) gain error.
- Fig. 14.** (a) The case of satisfied the monotonicity and (b) not satisfied the monotonicity.
- Fig. 15.** Aperture error by clock jitter or noise.
- Fig. 16.** Block diagram of dual-slope ADC.
- Fig. 17.** Integrator's output waveform of dual-slope ADC.
- Fig. 18.** Flash ADC structure with thermometer detection logic.
- Fig. 19.** Pipelined ADC block diagram.
- Fig. 20.** MDAC operations: (a) sampling mode, and (b) amplification mode.

**Fig. 21.** Time-interleaved ADC and its clock timing diagram.

**Fig. 22.** Conversion flow chart of cyclic ADC.

**Fig. 23.** Simple block diagram of cyclic ADC.

**Fig. 24.** Block diagram of SAR ADC.

**Fig. 25.** 5 bits' SAR ADC conversion procedure (a) sampling, (b) hold, and (c) redistribution mode.

**Fig. 26.** Split DAC simulation results depending on combinations of MSB and LSB array.

**Fig. 27.** Effect of parasitic capacitance of split Capacitive DAC.

**Fig. 28.** The accurate split C-DAC mismatch calibration.

**Fig. 29.** SAR ADC with Noise shaping.

**Fig. 30.** The example of electrochemical gas sensing method.

**Fig. 31.** The example of catalyst gas sensing method.

**Fig. 32.** The example of photoionization gas sensing method.

**Fig. 33.** The example of semiconductor gas sensing method.

**Fig. 34.** Conceptual diagram of proposed gas sensor system.

**Fig. 35.** Proposed prediction-based SAR ADC.

**Fig. 36.** Split-capacitor array and mismatch simulation with (a) 5:5 case, and (b) 6:4) case.

**Fig. 37.** Two phase operations of correlated double sampling.

**Fig. 38.** Conventional block diagram of resistance-to-voltage and resistance-to-frequency converter.

**Fig. 39.** RDC with resistive DAC circuit and divided output voltage.

**Fig. 40.** Operation of RDC with current DAC.

**Fig. 41.** Proposed gas sensor system block diagram.

**Fig. 42.** Definition of the time weighted average and the short time exposure limits.

**Fig. 43.** Operational flow for performance optimization and self-calibration.

**Fig. 44.** Proposed oscillation-based RDC block diagram.

**Fig. 45.** Block diagram of precision mode and CDS zooming scheme.

**Fig. 46.** Effect and Operation principle of CDS zooming.

**Fig. 47.** ANN-based prediction SAR conversion algorithm.

**Fig. 48.** Principle component analysis without artificial neural network.

**Fig. 49.** Proposed pattern recognition with artificial neural network.

**Fig. 50.** Gas monitoring system prototype and microphotographs of the designed ROIC.

**Fig. 51.** Real-time monitoring in smart phone.

**Fig. 52.** The range and accuracy of proposed dual-mode ROIC : (a) monitoring mode and (b) precision mode.

**Fig. 53.** Voltage and temperature characteristics in monitoring mode.

**Fig. 54.** MEMS sensors' characteristics measurements with five types of hazardous gases and temperature variation.

**Fig. 55.** Efficiency of prediction-based SAR ADC and error with (a) sine input and (b) CO-gas sensor input.

**Fig. 56.** Measured characteristics of prediction-based SAR ADC: (a) spectrum analysis and (b) DNL/INL.

**Fig. 57.** Confusion matrix in training step of pattern recognition.

**Fig. 58.** Optimization procedure of the number of hidden layers.

**Table I.** Performance summary in prior arts.

**Table II.** Performance summary and comparison with recent works.

## Nomenclature

<b>IoT</b>	internet of things
<b>ANN</b>	artificial neural network
<b>ROIC</b>	readout integrated circuit
<b>MCU</b>	microcontroller unit
<b>ADC</b>	analog-to-digital converter
<b>RDC</b>	resistance-to-digital converter
<b>CDC</b>	capacitance-to-digital converter
<b>TWA</b>	time-weighted average
<b>STEL</b>	short time exposure limits
<b>MLP</b>	multi-layer perceptron
<b>TSP</b>	touch screen panel
<b>ECG</b>	electrocardiogram
<b>BI</b>	body impedance
<b>UI</b>	user interface
<b>SNR</b>	signal-to-noise ratio
<b>TX</b>	transmit line
<b>RX</b>	receive line
<b>XDC</b>	X-to-digital converter
<b>SAR</b>	successive approximation register
<b>AS</b>	alternate-sample

<b>ENOB</b>	effective number of bits
<b>MRI</b>	magnetic resonance imaging
<b>CT</b>	computed tomography
<b>CDS</b>	correlated double sampling
<b>DNL</b>	differential nonlinearity
<b>INL</b>	integral nonlinearity
<b>LSB</b>	least significant bit
<b>DAC</b>	digital-to-analog converter
<b>SFDR</b>	spurious free dynamic range
<b>SNDR</b>	signal-to-noise and distortion ratio
<b>FFT</b>	fast Fourier transform
<b>SHA</b>	sample and hold amplifier
<b>S/H</b>	sample and hold
<b>MDAC</b>	multiplying DAC
<b>MSB</b>	most significant bit
<b>C-DAC</b>	capacitive-digital-to-analog converter
<b>FIR-IIR</b>	finite impulse response-infinite impulse response
<b>NDIR</b>	non-dispersive infrared
<b>MEMS</b>	microelectromechanical systems
<b>CAGR</b>	global annual growth rate
<b>AI</b>	artificial intelligence
<b>PCA</b>	principle component analysis

**SPI** serial peripheral interface

**CMOS** complementary metal-oxide-semiconductor



## Chapter I

### Introduction

#### 1.1 Sensor System

A Sensor system has been developed with advanced sensor researches in various fields such as the biomedical diagnosis and the environmental monitoring application. For example, a gas monitoring system can prevent unexpected accidents from hazardous substances, and bio-medical diagnosis system can be utilized for the overall health management of our body in factor environment and daily life. In addition, internet of things (IoT) which are connected to the internet through the embedded communication function gathers the transduced electrical signal from the sensors, and useful information is reinvented by the complex computing process like artificial neural network (ANN). Furthermore, the user who is used the sensor system has experience the quality of life [1].

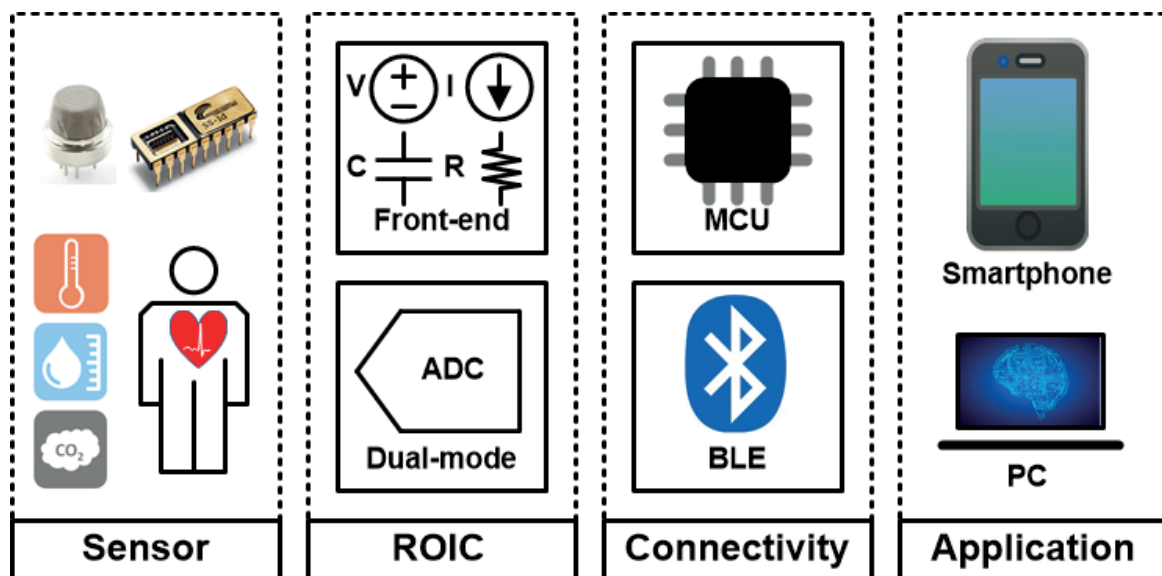


Fig. 1. Conventional sensor system configuration with application devices.

In Figure 1, a conventional sensor system consists of a suitable sensor, readout integrated circuit (ROIC), control and communication modules such as microcontroller unit (MCU) and Bluetooth. It can be interworked with a smartphone and applied to various applications through communication function. Thus, the smartphone or laptop illustrates the user-friendly information by the communication module. Each sensor converts the variation of electrical signals as voltage, current, resistance, and capacitance. In the case of voltage and current types, a high-performance analog-to-digital converter (ADC) can convert to a digital code that utilized to control and communicate for MCU. To process the resistance and capacitance information, specific voltage or current that is transformed from reference source as resistive or capacitance digital-to-analog converter can be converted using a specialized circuits such as resistance-to-digital converter (RDC) [2] and capacitance-to-digital converter (CDC) [3], which directly generate a digital code without ADC, have been researched.

The ROIC consists of a front-end and an ADC that includes the signal acquiring, processing, and converting the sensor signals. Therefore, specific ROIC functionally is necessary to process the variation of its sensor in the system. In the order words, the reconfigurable ROIC has advantages that support the IoT compatibility and save the cost for ROIC fabrication. However, different toxic gases kinds affect different exposure time and concentration. For example, the hydrogen sulfide ( $H_2S$ ) is critically toxic to give immediate fatal injury, and the carbon monoxide (CO) is chronically toxic to become serious when exposed for a long time [4]. The environmental standards in government express with two indexes that include time-weighted average (TWA) and short time exposure limits (STEL) [5]. Two conditions are decided by the exposure level and permissible concentration following each gas. Thus, the power consumption is wasted due to higher specification design for satisfying the highest requirement.

Also, sensor systems are usually processed with an ADC after conversion. For instance, most of the time for sensing the gas concentration is a little gas concentration and no precise resolution is required in Figure 2. The sensitivity is different depending on the types of gas and it occurs a complex decision situation [6]. In other words, useless power consumption is wasted, and the conventional sensor system is necessary to improve a learning-based algorithm and a reconfigurable ROIC that operates through low-power monitoring mode as RDC. Therefore, reconfigurable ROIC requires research on multi-mode sensing methods and algorithms that can determine the risk according to gas concentration and exposure time, and then change to high-resolution mode. Also, artificial intelligence technology that learns functions based on collected data and operates into efficient way and advanced works can be combined in conventional sensor systems.



**Fig. 2.** Requirement of reconfigurable gas sensor system for efficient operation.

## 1.2 Artificial neural network and learning-based algorithm

Recently, the ANN introduces one of the computing systems inspired by the biological neural networks in brains as seen in Figure 3. The ANN has ‘learning step’ which is called training and ‘decision step’ through the optimized layer. Many different machine learning algorithms have been actively researched, and this algorithm is helping to operate efficiently through optimization. Learning algorithms are divided into supervised learning that objectives are set as input and unsupervised learning that goals are not defined. Unsupervised learning is mainly used for clustering because there is no objective in the learning process. A hybrid paradigm is used depending on its application, it sets goals at an initial stage and carries out the classification learning process and proceeds with the rest to unsupervised learning. The ANN architecture is divided into feed-forward networks and recurrent/feedback networks. The neuromorphic system using ANN imitates synaptic biological functions and overcomes the limitations of conventional storage devices. It also studies the possibility of low-power and high-integration.

In addition, ANN is called a multi-layer perceptron (MLP) that composed of input layer, hidden layer, and output layer. The weights of hidden layers are optimized to refer to the characteristics of data and patterns. The layers can be extended to process the complex data and system easily. Thus, the ANN is not only processed linear system, but also non-linear or complex relationship is realized. It can reflect most of real-life situations. Data that is not included during the training process through the generalization can be decided. Therefore, ANN can be a powerful model widely used in various fields such as image processing, character recognition, and forecasting.

Conventional sensor systems only process and analyses the output of the system. However, by designing a ROIC that can be reflected by feedback the information from the analysis, the overall system performance can be improved efficiently. This thesis explains the previous reconfigurable system, gas sensor system and ADC in chapter II, and the detailed implementation of the gas monitoring system is shown in chapter III. Measurement results of the proposed system prototype are illustrated in chapter IV, and conclusions are drawn in chapter V.

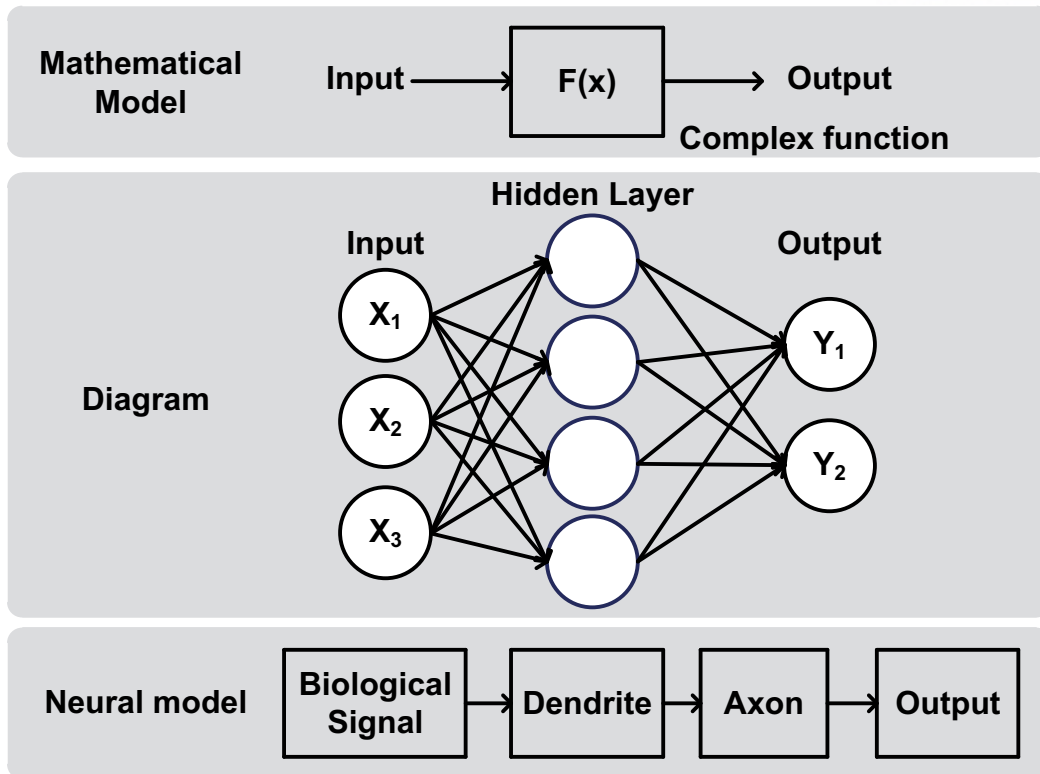


Fig. 3. Artificial neural network computation algorithm.

## Chapter II

### Background

Different kinds of sensors are needed suitable readout interfaces, and also different application fields require each interface to comply with application-specific inherent characteristics. However, simple integration of various sensor interfaces into single ROIC is not meaningful and does not reflect different kinds of requirements effectively. Another remarkable trend is that they are increasingly embedding more different functions, processing of data collected from multiple sensors. It is not easy to design an appropriate ROIC and it may be inefficient in terms of the overall system implementation. Therefore, it is necessary to implement a multi-functional ROIC for sensing multiple sensor's signal.

The most of sensors transform the sensing signal into electrical signals which are express with one of voltage, current, resistance and capacitance. In the other word, similar sensor which has same electrical characteristic can be process through similar ROIC. Each ROIC has different performance that range, resolution, conversion rate and etc. For example, the touch screen panel (TSP) and electrocardiogram (ECG) can be processed using a switched-capacitor amplifier depending on the variation of capacitance, and the sensing can be performed using the same circuit if only the required gain or electrode capacitance is adjusted. Therefore, for supporting two heterogeneous interfaces of the stretchable and the bio-signal, various sensor readout circuits are re-organized and effectively consolidated into two proposed basis readout topologies of the oscillator-based and the amplifier-based. The oscillator-based readout circuit is reconfigured to support low-power multi-sensor interfaces for the BI and resistive/capacitive stretchable sensors, and the amplifier-based is designed to support noise-immune multi-sensor interfaces for the touch and the ECG.

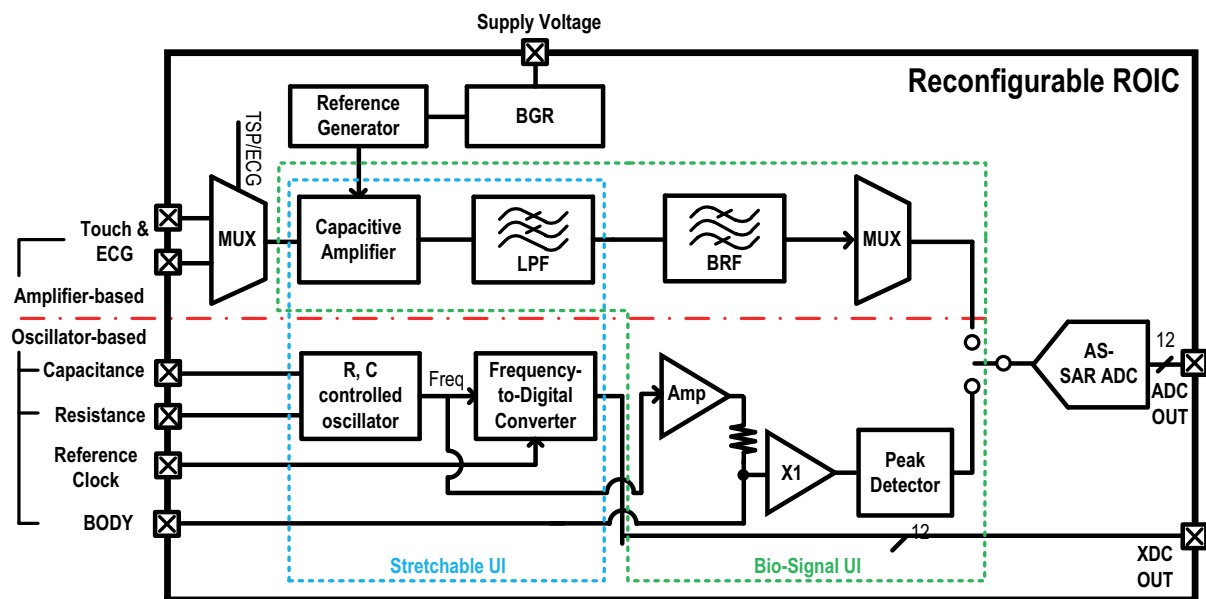
In order to control into processor and wireless communication, the acquisition signals from the front-end circuit are digitized by ADC. Power consumption and resolution have a trade-off relationship. A reconfigurable ADC is utilizing to adjust the resolution. Moreover, the noise shaping technique give an additional resolution through the quantization error reduction and effective conversion algorithm or switching algorithm are also introduced in the recent low-power application.

In this chapter 2, my previous works that are related with multi-functional ROIC implementation and ADC are described. In addition, the drawback of the previous system and prior-arts of gas sensor system are presented and it overcomes the several design issues into the proposed monitoring system.

## 2.1 Reconfigurable Display-based System

This work proposed a new interface architecture to accommodate different kinds of sensors on a TSP [7]. For this purpose, in addition to the touch sensing itself, bio-signal sensing interfaces for the ECG and the body impedance (BI) are newly proposed to utilize the TSP cells as capacitive coupling electrodes or channels. For flexible or wearable user interface applications, this work also includes low-power readout interface for various resistive or capacitive sensors that is effectively implemented by the oscillator-based readout circuits. The detailed of display-based heterogeneous multi-sensor interface architecture is presented sub-chapter of 2.1.

### 2.1.1 Reconfigurable multi-sensor readout structure



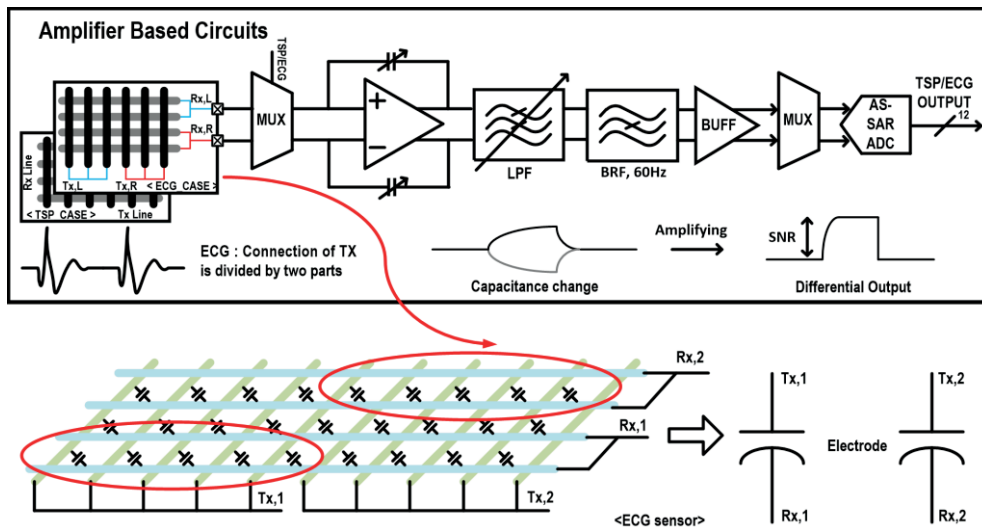
**Fig. 4.** A block diagram of the proposed reconfigurable readout integrated circuit.

Figure 4 presents the proposed ROIC [7] that supports a stretchable user interface (UI) and bio-signal UI, and also including a system prototype for display-based multi-sensor interface. In the previous researches, TSP focuses on the improvement of specification as the high signal-to-noise ratio (SNR) or



effectively driving algorithm for the transmit line (TX) and receive line (RX). Touch sensitivity and immunity against noise are improved to effort those of research [8,9]. In the recent work [10], the fingerprint technique has been embedding inside the TSP. The fingerprint detecting is similar sensing type and necessary to enhance the sensitivity. The stretchable or the foldable TSP are one of future trend in the display application and its technical functionality is utilized for the convenient to the user. Also, the display is important part of electrical devices. The research of the reconfigurable ROIC which is processed the accommodate signals on the TSP is needed.

First of all, for this purpose, in addition to the touch sensing itself, bio-signal sensing interfaces for the ECG and the body impedance (BI) are newly proposed to utilize the TSP cells as capacitive coupling electrodes or channels. For the flexible applications, this work also includes low-power readout interface for various resistive or capacitive sensors that is effectively implemented by the oscillator-based readout circuits.



**Fig. 5.** Amplifier-based multi-sensor interface configuration.

Secondly, the proposed reconfigurable readout structure can support various different kinds of sensors effectively, not requiring many individual sensor readout circuits. For supporting two heterogeneous interfaces of the stretchable and the bio-signal, various sensor readout circuits are reorganized and effectively consolidated into two proposed basis readout topologies of the oscillator-based and the amplifier-based. The oscillator-based readout circuit is reconfigured to support low-power multi-sensor interfaces for the BI and resistive/capacitive stretchable sensors, and the amplifier-based

readout is designed to support noise-immune multi-sensor interfaces for the touch and the ECG. Figure 5 illustrates the amplifier-based readout circuit and the TSP configuration is shown that the panel is used two electrodes for measurement of ECG. In this way, two kind of sensing for the touch and the ECG are cost-efficiently working by utilizing the same amplifier-based readout circuit.

Lastly, the low-power oscillator-based readout adopts the X-to-digital-converter (XDC) whose digital conversion is performed by combining the oscillator and the counter, not requiring additional ADCs. For the noise-immune amplifier-based readout, the successive approximation register (SAR) ADC is designed to support the error-correction capability by including the proposed alternate-sample (AS) scheme. Through this AS-SAR ADC, instant digital errors can be recovered, and its effective number of bits (ENOB) improvement are experimentally verified. The related explanations of the XDC and AS-SAR ADC will be described in chapter 2.1.2 later.

## 2.1.2 Multiple digital conversion methodology

An ADC is essential circuit and it transforms the analog signal to digital signal. When implementing the ADC, power consumption, resolution and conversion rate are mainly considered along their application. Especially, the power consumption and resolution have a trade-off relationship, thus ultra-low power designs are possible if high-resolution ( $>10$ ) is not required. Therefore, the low-power oscillator-based readout adopts the XDC whose digital conversion is performed by combining the oscillator and the counter, not requiring additional ADCs. Figure 6 presents oscillator-based multi-sensor interface and TSP configuration for BI measurement. The oscillator is composed of resistance and capacitance-controlled circuit, delay cell and counter. Different frequency is produced from the variation of resistance or capacitance. Therefore, XDC is utilized the resistive or capacitive sensor. Also, its frequency is sweep by resistance or capacitance and the generated frequency is used to measure the body impedance. The BI measures through the multi-frequency bioelectrical impedance analysis [11].

For the noise-immune amplifier-based readout, the SAR ADC is designed to support the error-correction capability by including the proposed AS scheme. Through this AS-SAR ADC, instant digital errors can be recovered. As seen in figure 7, the proposed alternate-sampling error-correction scheme starts from the alternate sampling. Then, its acquired differential data are compared with its interpolated values. The error correction process judges that an instant error has occurred by

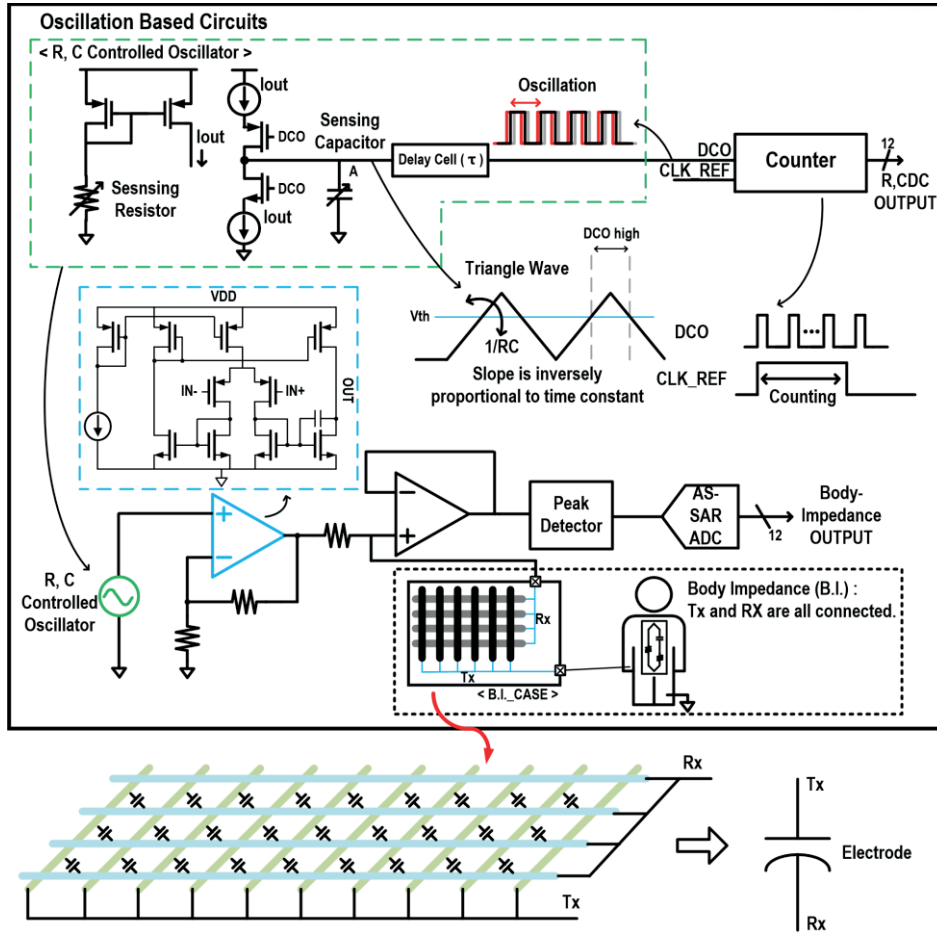


Fig. 6. Oscillator-based multi-sensor interface configuration.

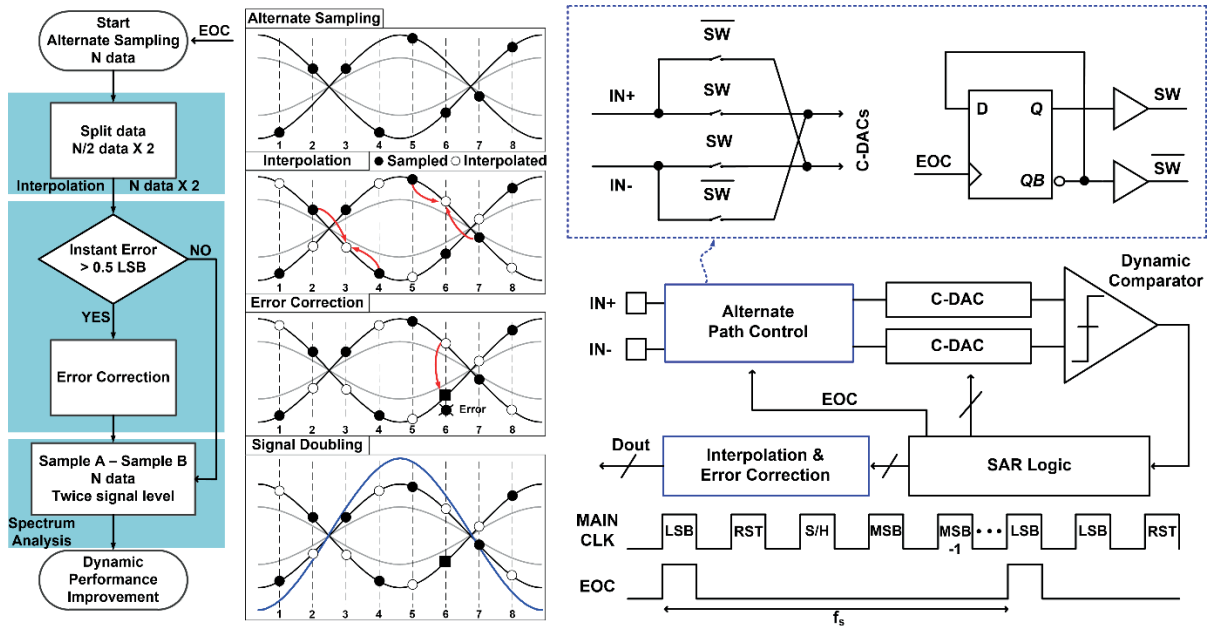


Fig. 7. Alternate sampling algorithm for SAR ADC.

the equation (2.1) that sum of same timing sampled and counterpart interpolated values is larger than 0.5 LSB or not. Ideally, sum of in-phase and anti-phase sampled data becomes equal to maximum code. If not, complement code of interpolated value is corrected to conversion results. Through these comparisons between the sample data and the interpolated values, instant error in each sample can be detected as:

$$D_{SampleA}(i) + D_{SampleB}(i) = D_{maxcode}(i) + e_{instant} \quad (2.1)$$

Where  $D_{sampleA}(i)$  and  $D_{sampleB}(i)$  are  $i$ -th differentially-sampled data, and instant errors of  $e_{instant}$  occur along to their peak-to-peak amplitude of  $D_{maxcode}(i)$ .

The proposed scheme can correct consecutive errors also thanks to inherent splitting operation of the alternate sampling. If there are two consecutive errors, the proposed work can correct them by alternating two sampled values and comparing them with their corresponding interpolated values. However, from three consecutive errors, the capability of error correction degrades seriously because the comparing references of interpolated values are also corrupted. This limited capability would be improved through our upcoming works.

For further understanding, graphical description with example data are given below as Figure 8. Sampled data are split into two parts by the alternate sampling. Then, they are compared with its corresponding interpolated value, and the instant error by equation (2.1) is detected. Since second sample is detected to be wrong conversion, and it becomes replaced by 2's complement value of 580 that is equal to 3515.

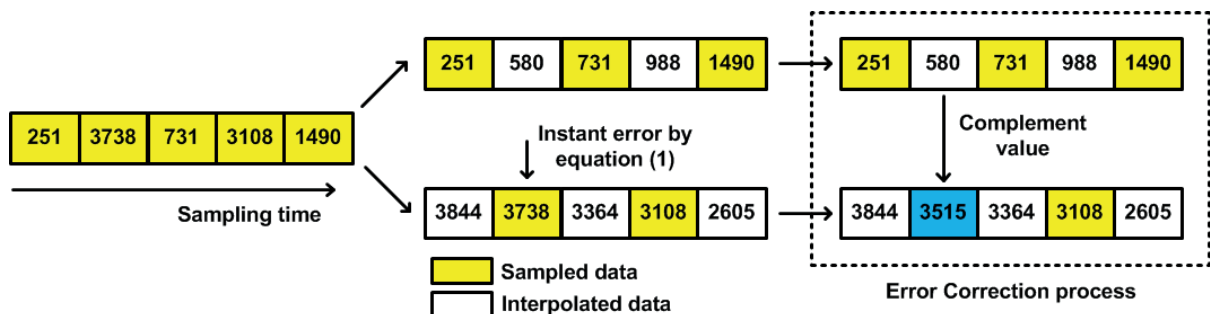
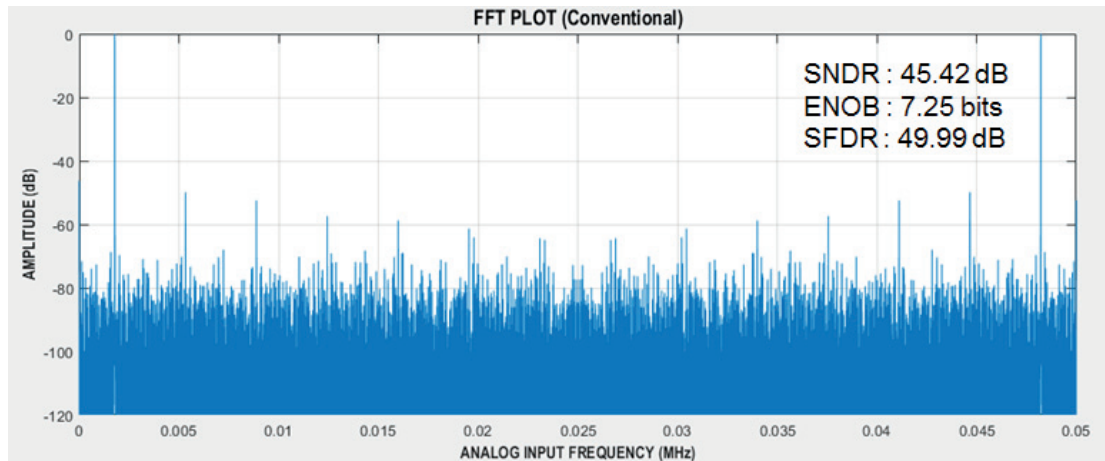
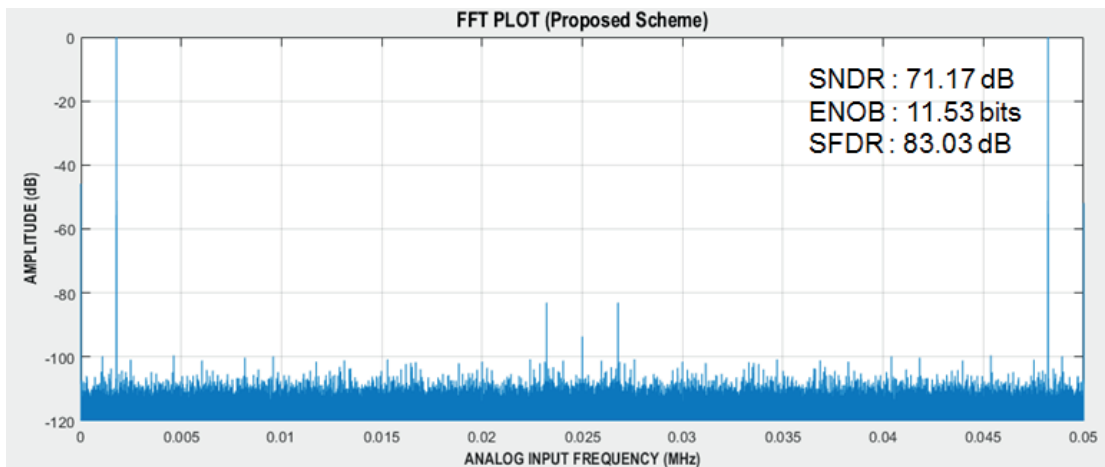


**Fig. 8.** Alternate-sampling error correction scheme with example data.

Also, figure 9 shows its resulting ENOB improvement in measured ADC dynamic performance. Figure 9 (a) is from conventional SAR ADC conversion without the AS scheme, where many harmonics occurred repeatedly and the ENOB degraded. After activating the proposed AS scheme, most of harmonic and common-mode noise are eliminated and ENOB improved by 4.28 bits in the figure 9 (b).



(a)



(b)

**Fig. 9.** Measured 262144-point FFT spectrums at 1.777 kHz input (a) without / (b) with alternate sampling and error correction scheme.

### 2.1.3 Summary

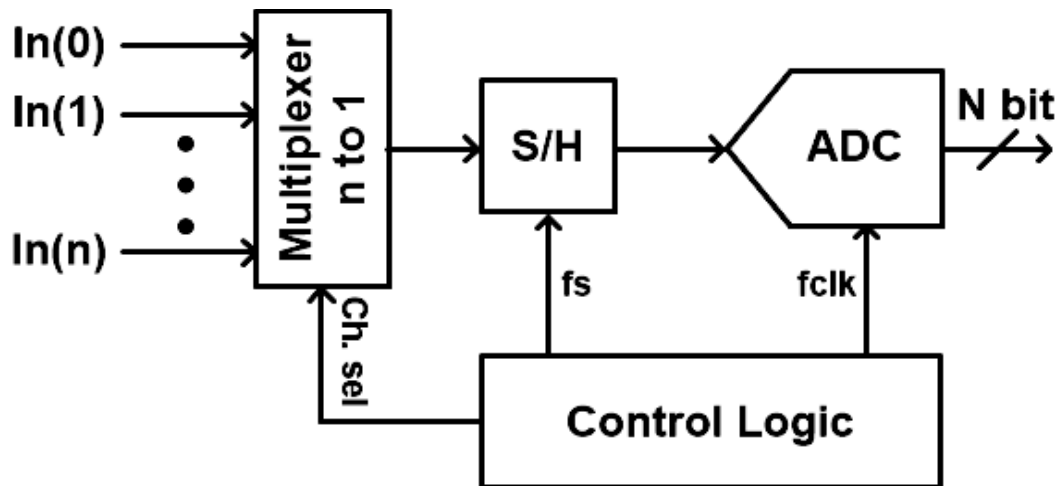
Heterogeneous sensor interfaces that including TSP, resistive, capacitive, BI and ECG was proposed in previous work [7]. A reconfigurable ROIC architecture supports the various application and operation-based design and core block sharing are cost-efficient implementation. Table I is shown that the performance summary and comparison [2, 12-14]. In case of the error correction capability, previous ADC works requires complex additional circuits or conversion like [15,16]. This work was integrated the various sensor types and moderate performance. However, this approach has shortcoming which the restricted performance and efficiency of the system. ROIC is necessary to cover the worst case of the system operation and it occurs more higher specification with wasted power consumption and resolution during some case. Therefore, the performance and efficiency of system will be improved by neural network and MCU and the details of proposed works will describe in the next chapters.

Table I. Performance summary in prior arts.

Parameter	This Work	[12]	[13]	[14]	[2]
Process	0.18 um	0.18 um	0.18 um	0.16 um	0.18 um
Supported sensor types	TSP, R/C type, BI, ECG	TSP	BI, ECG	C type	R type
Power consumption (mW)	1.163 (TSP/ECG+ADC) 0.202 (XDC) 0.271 (BI+ADC)	6.26 (TSP)	0.233 (3 chanel BI + ECG )	0.014 (CDC)	0.0017 (RDC)
Area (mm <sup>2</sup> )	0.67 (TSP/ECG) 0.057 (XDC) 0.223 (BI) 0.95 (ADC)	2.2	8.17(estimated per channel) 49(ROIC+ MCU)	0.05	1.23
Application	Bio-signal aquasition, TSP, R & C type sensor	TSP	Bio-signal aquasition	C type sensor	R type sensor
Supply (V)	1.8	2.1 - 3.3	1.2	1	1.2 / 0.6
Resolution (bits)	12	N.A.	13.5	13.1 (CDC)	10
R, C sensing Range ( $\Omega$ ), (F)	R: 270k – 1M C: 0 p – 27p	N.A.	N.A.	C: 0 – 8p	R : 10k – 10M
TSP channel	TX: 32 RX: 8	TX: 12 RX: 8	N.A.	N.A.	N.A.
Frame rate (Hz)	240	50 - 6400	N.A.	N.A.	N.A.
TSP SNR (dB)	44.36	40 @ OSR 32	N.A.	N.A.	N.A.
Body impedance frequency range (Hz)	50k – 750k	N.A.	1 – 20M	N.A.	N.A.

## 2.2 Analog-to-Digital Converter

Main role of ADC takes analog input and converts it to digital code. When used with a multiplexer for chip area and power budget, multiple input signals can be processed by a single ADC. Figure 10 presents the general block diagram of the ADC systems.



**Fig. 10.** The block diagram of the analog-to-digital converter system.

Application areas using ADC are widely utilized in the fields of communication, image signal processing, medical devices such as magnetic resonance imaging (MRI), computed tomography (CT), and computer fields such as voice recognition and video graphic controller sensors. Depending on the application, the architectures and specifications of the ADC are determined. In this chapter 2.2, I will describe the overview of ADC architecture and its operation.



## 2.2.1 ADC overview

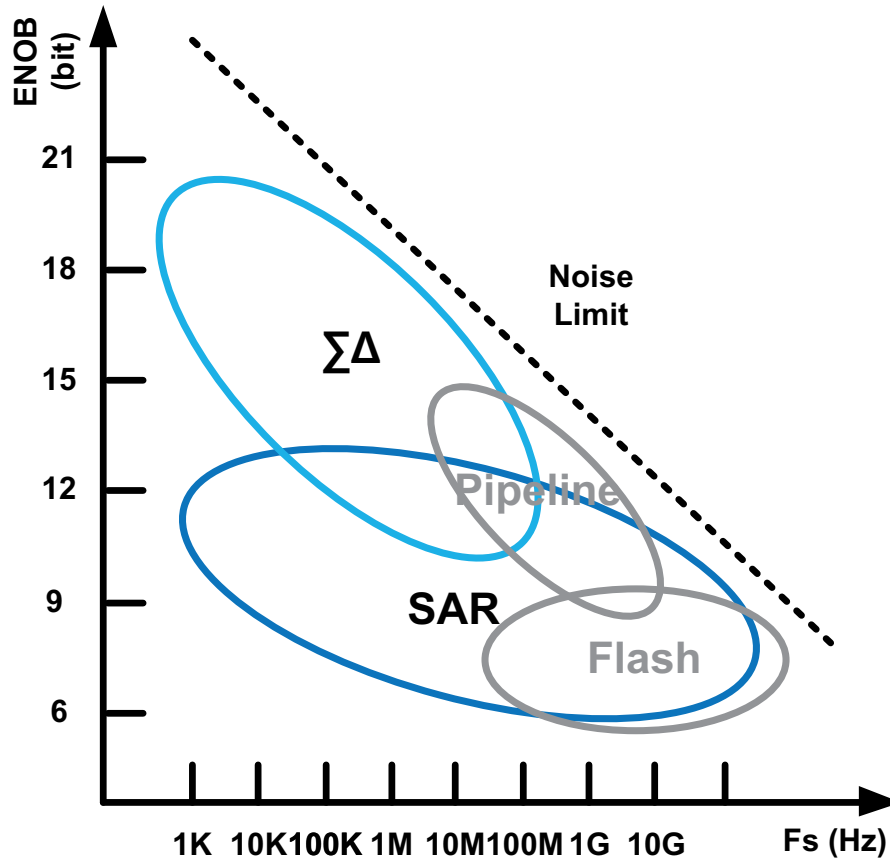


**Fig. 11.** The characteristics of each ADC architecture: sampling rate vs resolution.

In the Figure 11, suitable architecture of the ADC varies according to the desired specification, and there are many kinds from flash ADC being used at high speed to sigma-delta ADC mainly used for high resolution. Among these structures, the SAR ADC has an easy to design the structure with low-power consumption and can have intermediate resolution with moderate speed, so if it needs to increase the resolution through calibration, SAR ADC can be used as a suitable converter for sensor system. In the case of front-end, correlated double sampling (CDS) technique is utilized to remove the offset that may occur in the process of sampling by the ADC and stably transfer the sampled signal. The block and technique in the ROIC are explained, and the implementation is shown in the next chapter III.

a. The key specifications

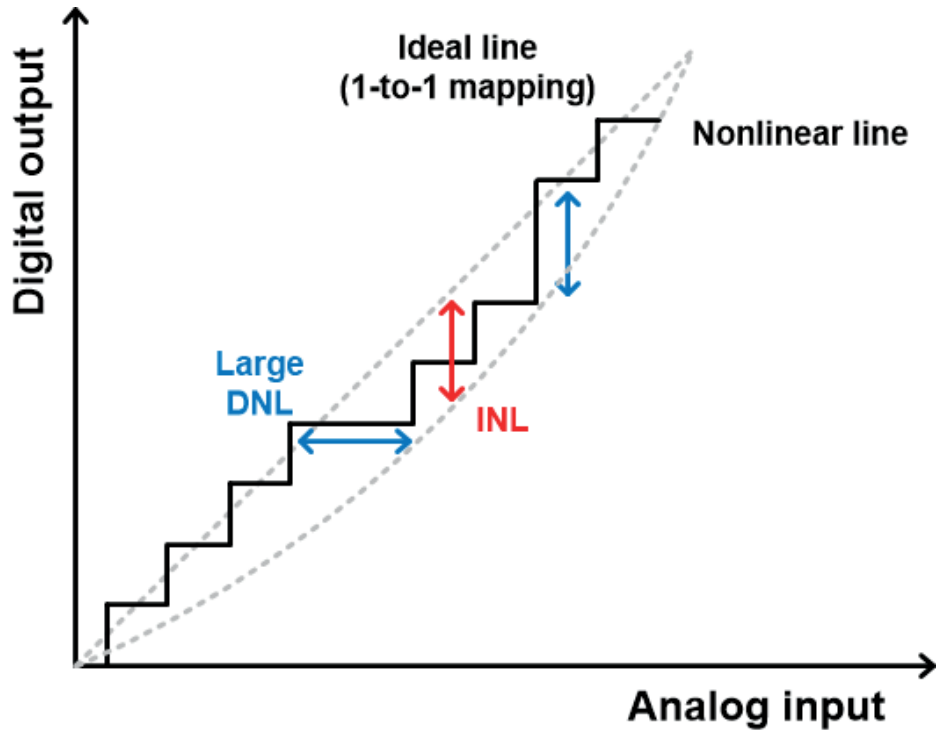
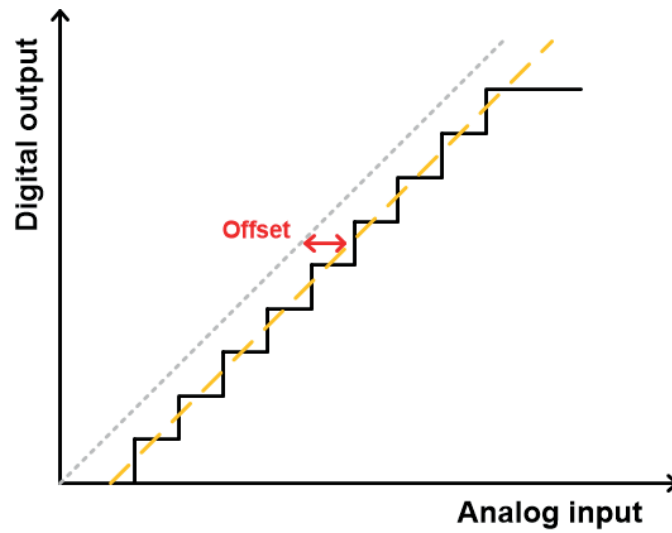


**Fig. 12.** The DC characteristics of ADC: Differential nonlinearity and Integral nonlinearity.

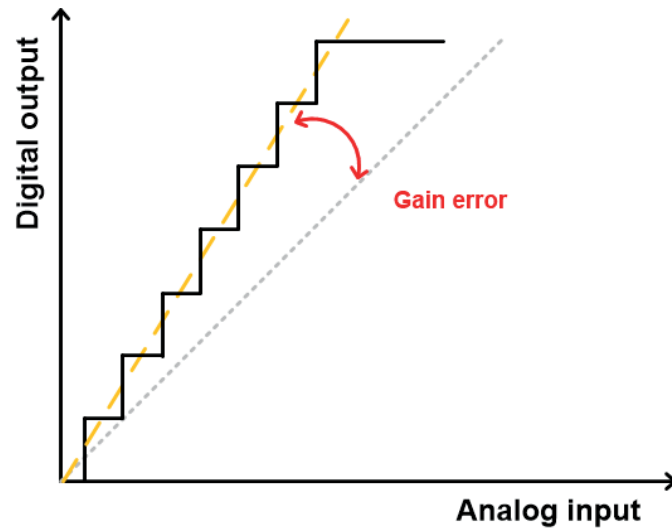
- Differential nonlinearity (DNL) : The difference between two consecutive input values is called the DNL as seen in Figure 12. If the error occurs less than 1 least significant bit (LSB), the ADC is permissible to convert the designed resolution. The largest difference is shown that the limitation of the ADC's performance.
- Integral nonlinearity (INL) : The INL is summation of the all of DNL error, it means that the error is cumulative factor from the initial point to any analog input. Therefore, the curve form of INL illustrates the symmetric of the overall system.
- Offset error : In the Figure 13 (a), the offset error is the distance from the point where the characteristic curve of the convert meets the analog input axis to the origin. Since the error is linear against the overall range, it can't affect the spectrum of the ADC. However, the dynamic range can be reduced after the correction the offset error.
- Gain error : The difference when the slope of the ADC characteristic curve is compared to the

ideal curve in Figure 13 (b).

- Full scale : The difference between the maximum and minimum values of the analog input signal step that the converter can be digitized.



(a)



(b)

**Fig. 13.** The main conversion errors : (a) offset error (b) gain error.

- Resolution : The number of different input levels corresponding to the output digital code is called by the resolution of its ADC. For example, a converter with N bits of resolution has  $2^N$  different analog levels. Thus, it is the number of bits of the output digital code usually in the ADC.
- Accuracy : The absolute accuracy of the ADC means the difference between the expected transfer function characteristic and the actual characteristic, including the offset error and the gain error. For 12 bits, the relative accuracy indicates that the converter error is less than the input full scale divided by  $2^N$ .
- Monotonicity : In terms of the transfer characteristic of the ADC, the output also increases as the input increases. Figure 14 is shown that the two cases of the satisfying the monotonicity and not.

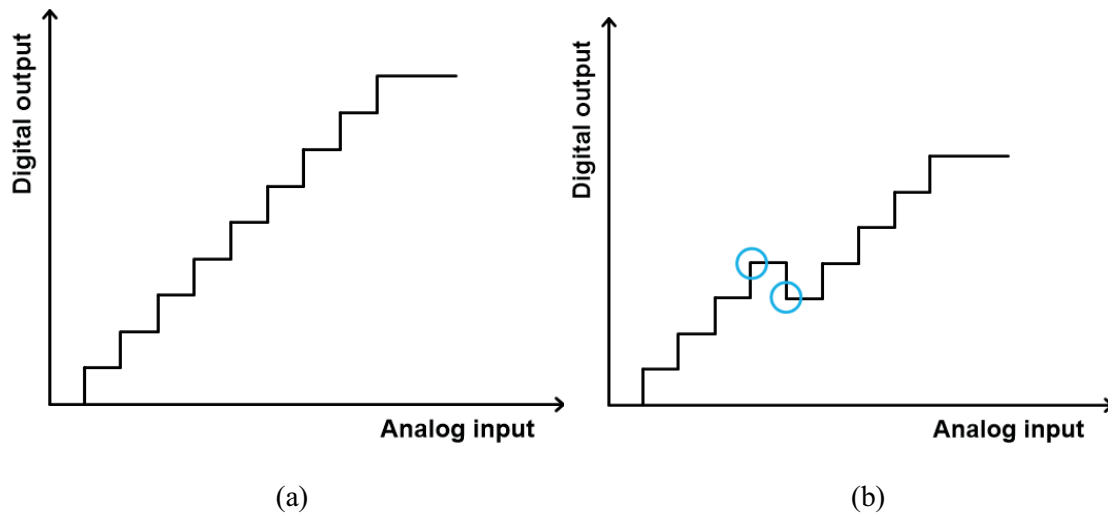


**Fig. 14.** (a) The case of satisfied the monotonicity and (b) not satisfied the monotonicity.

b. Main issues of performance degradation

Quantization noise is defined by the limitation that the ADC can digitize the minimum analog input level into Nyquist rate converter. Assume the ADC and digital-to-analog converter (DAC) are ideal converter, the quantization noise ( $V_Q$ ) is defined as:

$$V_Q = V_1 - V_{in} \quad (2.2)$$

Where  $V_1$  is analog output that regenerated by the ideal DAC.

When  $V_Q$  is defined as an arbitrary function,  $V_Q(\text{rms})$  is obtained statistically. When  $V_Q$  has a certain probability in the interval of  $\pm 1/2 V_{LSB}$ ,  $f_Q(x)$  is a probability density function of  $V_Q$ . Thus, the  $V_Q(\text{rms})$  express with  $f_Q(x)$  as follows :

$$V_Q(\text{rms}) = \left[ \int_{-\infty}^{\infty} x^2 f_Q(x) dx \right]^{\frac{1}{2}} = \left[ \frac{1}{V_{LSB}} \int_{-V_{LSB}/2}^{V_{LSB}/2} x^2 dx \right]^{\frac{1}{2}} = \frac{V_{LSB}}{\sqrt{12}} \quad (2.3)$$

Maximum SNR is calculated from this result. First, when the input is a sine wave and the input power is in the range of  $0 \leq V_{in} \leq V_{ref}$ , the power of the input is  $V_{ref}/2\sqrt{2}$ . Thus, the SNR can be defined as :

$$\text{SNR} = 20 \log \left( \frac{V_{in(\text{rms})}}{V_Q(\text{rms})} \right) = 20 \log \left( \frac{\frac{V_{ref}}{2\sqrt{2}}}{\frac{V_{LSB}}{\sqrt{12}}} \right) = 20 \log \left( \sqrt{\frac{3}{2}} 2^N \right) \approx 6.02N + 1.76 \text{ (dB)} \quad (2.4)$$

As shown in above equation, the SNR is decided its number of bits. Also, harmonic components due to input signal should be considered. Spurious free dynamic range (SFDR) is the difference in maximum spurious component magnitude with respect to the signal component magnitude on the frequency axis. And signal to noise and distortion ratio (SNDR) refers to the ratio of the sum of the noise and harmonic power to the signal power. Therefore, the ENOB is a performance measurement of the ADC's digital output signal that obtained by fast Fourier transform (FFT) analysis on the frequency axis and it can be express as :

$$\text{ENOB} = \frac{\text{SNDR} - 1.76}{6.02} \quad (2.5)$$

In addition, the uncertainty of the input signal due to aperture error as shown in Figure 15 can also affect the ADC performance. The time required for conversion is the aperture time, and its error is increased by clock jitter or noise as the frequency increases. Depending on the application, the following noise may be important and needs to be considered.

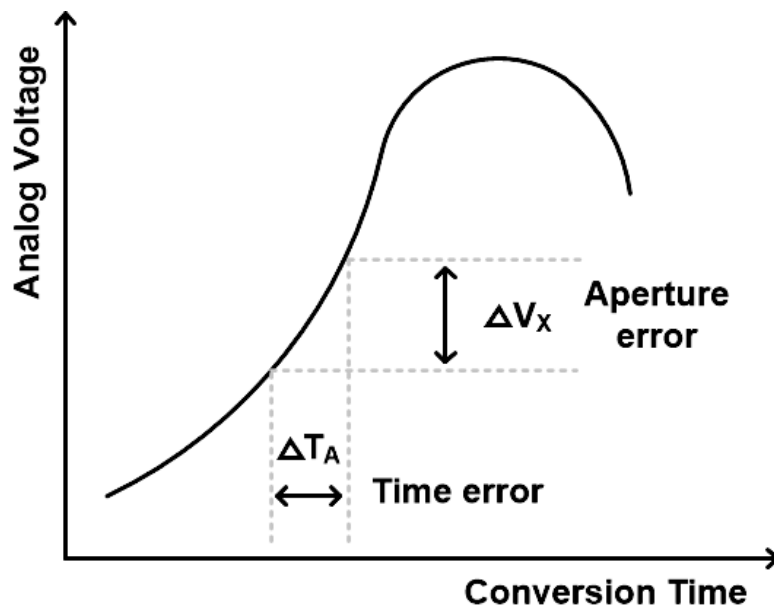


Fig. 15. Aperture error by clock jitter or noise.

## 2.2.2 Architecture

Various architectures of ADC have been researched and its structure is utilized the its suitable application. Popular architectures are introduced in this sub-chapter and their operations are reviewed shortly.

### a. Dual-slope ADC

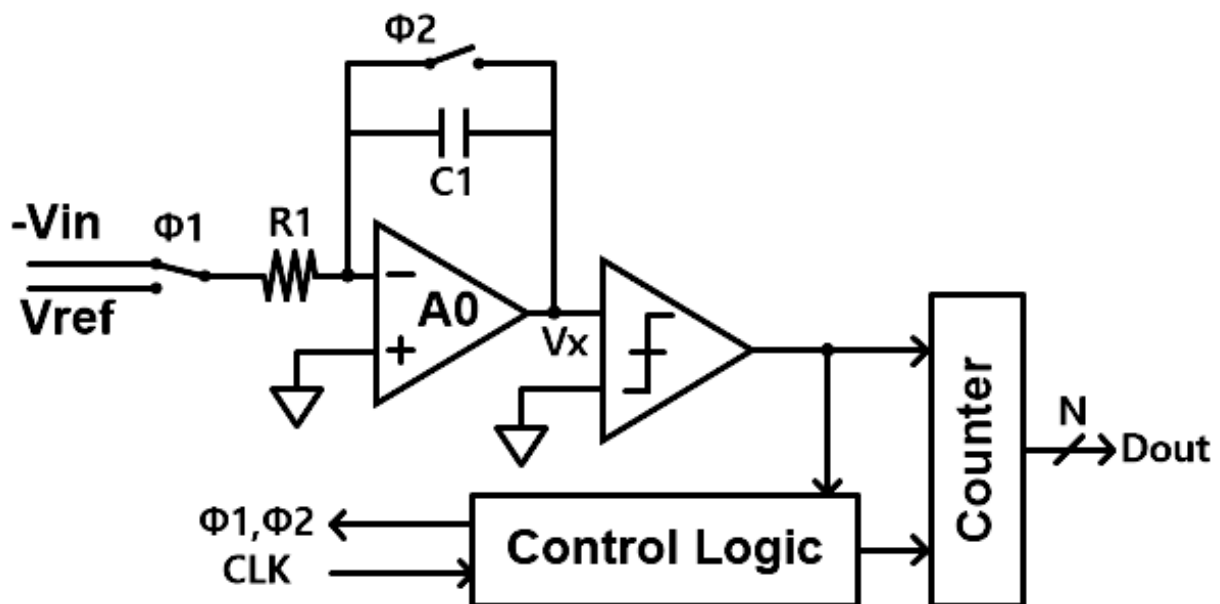
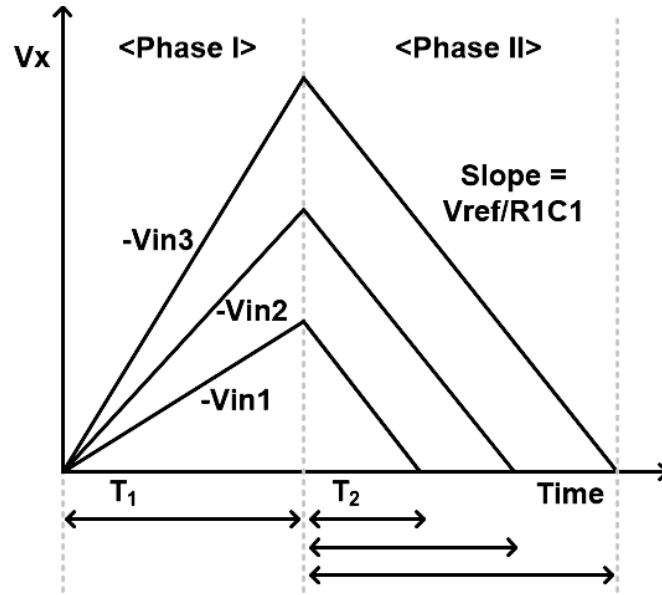


Fig. 16. Block diagram of dual-slope ADC

Integrating-type ADCs are widely used to convert for high-resolution and very slow signal acquisition, and it has a benefit into an accurate measurement or control system. It has also high accuracy, simple structure, easy to implement and low cost. In addition, integrating ADC is strongly immune to noise characteristic, and since the counter is operated by continuous digital counting over the reference voltage integration time, there is no missing code. Dual-slope ADC is one of efficient architecture and composed of integrator, comparator, clock generator, binary counter and control logic in figure 16.



**Fig. 17.** Integrator's output waveform of dual-slope ADC.

Firstly, the counter and integrator are reset before each conversion step. As shown in figure 17, the operation of dual-slope ADC is described by two phases that phase I during the time  $T_1$  and phase II during the time  $T_2$ . During Phase I, switch is connected to  $-V_{in}$ , and a ramp waveform appears in which the output  $V_x$  is proportional to the magnitude of  $V_{in}$ . The integrator voltage,  $V_x$  express as follows the equation (2.6):

$$V_x(t) = - \int_0^t \frac{(-V_{in})}{R_1 C_1} dt = \frac{V_{in}}{R_1 C_1} t \quad (2.6)$$

In the case of the phase II, switch is connected to  $V_{ref}$  and the counter is reset. The integrator output  $V_x$  begins to decrease with a slope of  $-V_{ref}/R_1 C_1$ . The voltage is decrease until  $V_x = 0$ , during which the digital binary number is counted. Then, the equation (2.7) is presented the variation of  $V_x$ .

$$V_x(t) = - \int_{T_1}^t \frac{(-V_{ref})}{R_1 C_1} dt + V_x(T_1) = - \frac{V_{ref}}{R_1 C_1} (t - T_1) + \frac{V_{in} \cdot T_1}{R_1 C_1} \quad (2.7)$$

Assume the  $T = T_1 + T_2$ , the integrator output is back to zero.



$$0 = -\frac{V_{ref}}{R_1 C_1} (T_2) + \frac{V_{in} \cdot T_1}{R_1 C_1} \quad (2.8)$$

$$\therefore \frac{T_2}{T_1} = \frac{V_{in}}{V_{ref}} \quad (2.9)$$

The digital code ( $T_2$ ) are figure out from the known value of the  $V_{ref}$  and  $T_1$ . Since the digital output is determined by the ratio of  $T_1$  and  $T_2$ , the accuracy is independent of the time constant of RC or the value of the clock frequency. Therefore, the dual-slope ADC has advantage against the mismatch of RC or clock frequency.

b. Flash ADC

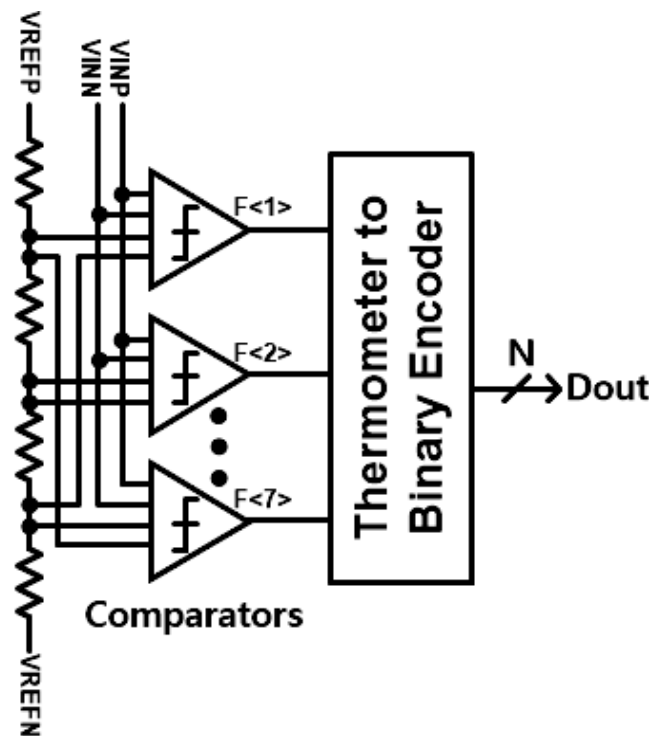


**Fig. 18.** Differential 3-bit Flash ADC structure with encoder logic. [17]

This flash ADC is needed the  $2^N$  of resistors,  $2^N-1$  of comparators and encoder for achieving the  $N$  bits resolution as seen in Figure 18. One side of the comparator has  $V_{in}$  and the other side has  $V_{ref}$ ,

which is converted into a digital code for one clock at the same time. Thus, when the input voltage is greater than the reference voltage, it is digitized as 1, and otherwise the comparator outputs are 0. This is regarded as a thermometer code. The ADC is necessary to convert the output code of N bits through thermometer code detector and encoder. Conversion rate is fast over the GS/s, but the area and power consumption of comparators and resistors are very high. The design is hard to overcome the 8 bits.

c. Pipelined ADC & Time-interleaved ADC

The pipeline scheme is an ADC that is widely used to improve signal processing speed. Pipelined ADCs are allowed the inputs continuously without having to wait for previous inputs to be fully converted to digital outputs, and multiple stages simultaneously operate on different inputs and output successive digital values. It is a structure that optimizes the overall system area and power consumption while achieving a high conversion rate. The figure 19 shows a block diagram of a pipelined ADC consisting of k stages. Each stage includes sample and hold amplifier (SHA), flash ADC, DAC and residue amplifier with fixed gain.

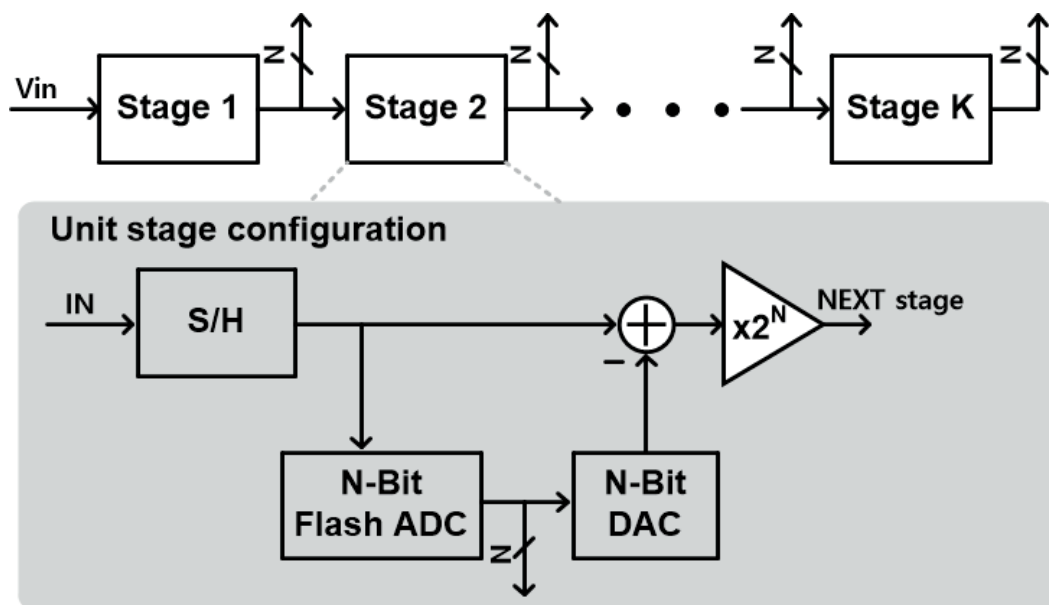


Fig. 19. Pipelined ADC block diagram.

First, each stage samples and holds the output of the preceding stage through the sample and hold (S/H). The upper ADC outputs a low-resolution digital signal for the holding input, and the output digital signal is again converted into an analog signal quantized by the DAC. Finally, the subtractor amplifiers the residue voltage, which is the difference between the signal held by the SHA and the DAC output, and sends it to the next stage. The next stage receives the amplified residual voltage from difference between the front-end and digital code outputs. At the same time, the front-end receives the next input and repeats the above operation. As these results, the first stage receives new input continuously, and the residue voltage generated at each stage is continuously transmitted up to the k-th stage, so that digital signals are converted to the output simultaneously to different inputs at every stage after a certain time. Since there is a time difference between the digital signals output from each stage for one input signal, a register is required to store the digital signals output first in order to obtain a complete output.

Generally, in the case of the pipelined ADC, DAC operation and residue voltage amplification are performed at one time through a multiplying DAC (MDAC) and use a non-overlapping clock to control the MDAC sampling and amplification modes. In the Figure 20 (a), it shows the sampling mode of MDAC, the input signal is stored in all capacitors and connects the input and output of the amplifier to remove the remained charge. And then, the flash ADC converts the analog input signal into a digital signal. In the clock phase that opposite to the sampling mode, MDAC operates in the amplification modes as shown in Figure 20 (b). Each capacitor is connected to positive or negative reference according to the output digital code of the flash ADC, and the difference between the analog input signal and the output signal of the DAC is amplified. In the sampling mode, the charge corresponding to the input is stored in the capacitor array, such as  $Q_i = 2^N C V_{in}$ , and the amount of charge due to the quantized input in the amplification mode is expressed as  $Q_i = 2^N C (D(1) * V_{ref}) + C V_0$ . From the charge are conserved during the conversion, so if both equations are set equally, the output of MDAC amplifies the residue voltage by  $2^N$ , as in  $V_O = 2^N (V_{in} - D(1) * V_{ref})$ . The  $D(1)$  is decided by the output of flash ADC. Because of the gain error and mismatch of the capacitor, the output of MDAC may be larger or smaller than ideally expected. To solve this problem, digital correction logic is usually used with  $2^N - 1$  instead of  $2^N$ . Assuming that the resolution of all the stage is the same in the pipelined ADC, the number of stages used and the resolution required in each stage have the relationship  $k = (N - x) / (n - x)$ , where  $N$  is overall resolution of pipelined ADC,  $k$  is the available stage,  $n$  is each stage resolution and  $x$  is marginal resolution for digital correction logic. Pipeline ADCs have advantages and disadvantages depending on the number of stages and resolution to be used. However, all blocks generate consecutive outputs for successive input signals, and area and power consumption can be reduced that compared with flash ADC.

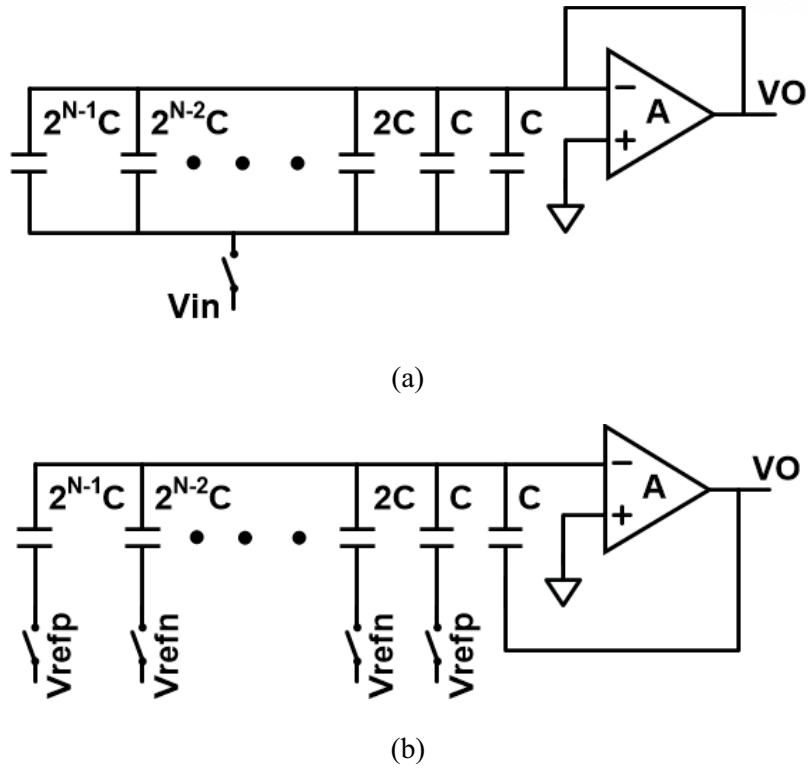


Fig. 20. MDAC operations : (a) sampling mode, and (b) amplification mode.

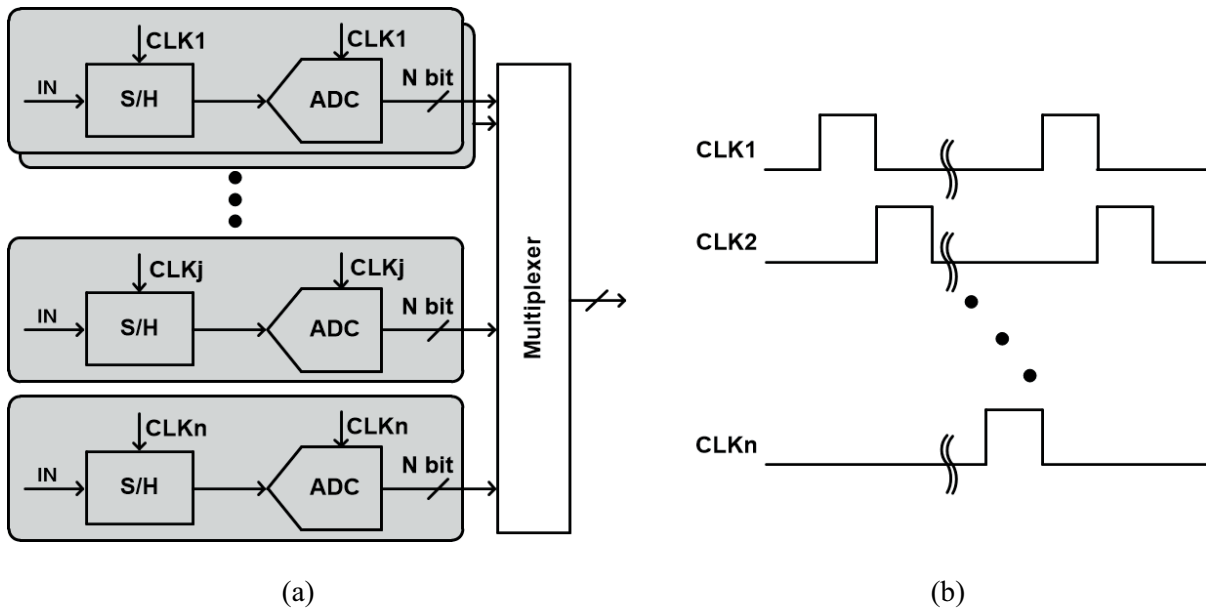


Fig. 21. Time-interleaved ADC and its clock timing diagram.

Furthermore, the various ADC structures described above have limitations in speed up. The researched architecture is a time-interleaved ADC in Figure 21. Time-interleaved ADCs with multiple independent ADCs connected in parallel can be operated as fast as the number of ADCs used, applying this technique suitable for high speed applications. However, there is mismatch between channel sampling timing. If the operation clock of each channel occurs timing skew, sampling between channels for the analog input signal is performed at unequal intervals. This problem is inevitable due to the asymmetry of the clock distribution between the channels in the layout, especially at higher frequencies, this phenomenon occurs more severely. Also, gain error and offset into each channel reduces the overall performance of the time-interleaved ADC.

d. Cyclic ADC

The cyclic ADC is called a serial converter. Because it needs the N times conversion cycle for N bit conversion. However, this architecture has small area and moderate resolution due to reuse the most of circuits. The flow chart of a typical cyclic ADC that determines one bit in one conversion cycle is shown in the Figure 22.

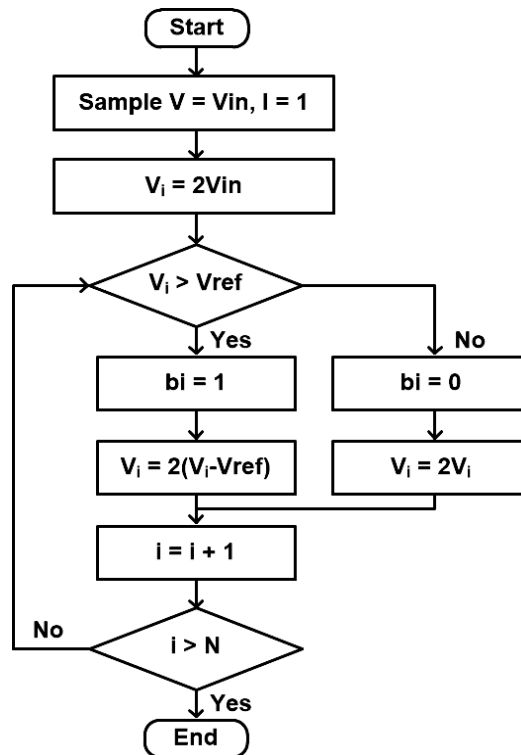


Fig. 22. Conversion flow chart of cyclic ADC.

First, the input voltage is sampled and amplified twice. Compared to the amplified value and  $V_{ref}$ , if the amplified value is greater than  $V_{ref}$ , the most significant bit (MSB) becomes 1. After that, it subtracts  $V_{ref}$  from the amplified signal, and the residue voltage amplify by twice. On the other hand, if the amplified value is smaller than  $V_{ref}$ , the MSB becomes 0, and this output value is doubled. This procedure is N times repeatedly for N bit conversion.

The Figure 23 presents a block diagram of the cyclic ADC. Switch S1 is connected to  $V_{in}$  to sample the input voltage at the SHA. If the digital codes is 1, switch S2 is connected to  $V_{ref}$  and  $V_{ref}$  is subtracted. This value is sampled in SHA<sub>2</sub>, applied to the input of SHA<sub>1</sub> by S1, and the above process is repeated.

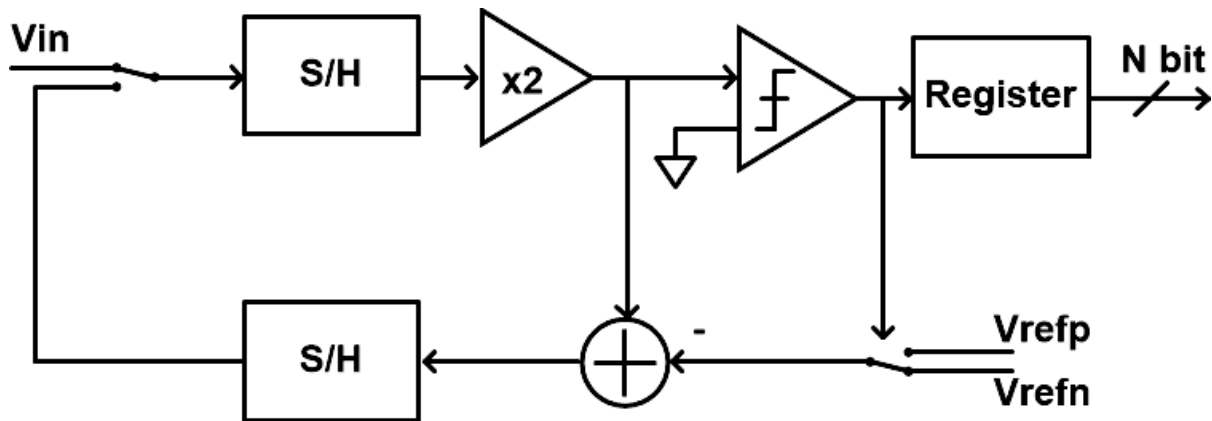


Fig. 23. Simple block diagram of cyclic ADC.

Since the cyclic ADC has a cyclic structure that repeats for several cycles during operation, the variation of the device size caused by the process such as device mismatch is accumulated compared to other structure. In order to minimize that mismatch, ratio independent technique, reference refreshing technique and digital error correction are utilized.

Cyclic ADC has very simple architecture and small chip area because of repeated use of same circuits. Therefore, it is possible to apply a system application requiring a low power and a portable small electronic product. However, a cyclic has slow operation because it should be repeated many times in order to determine N bits of digital code.

e. Successive approximation register (SAR) ADC

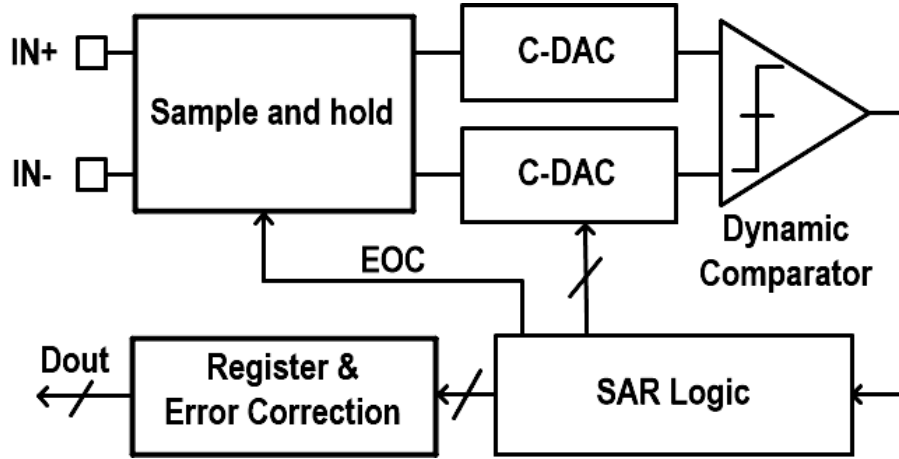


Fig. 24. Block diagram of SAR ADC.

Successive approximation register (SAR) ADC is effective architecture along the development of complementary metal-oxide-semiconductor (CMOS) process. As shown in Figure 24, SAR ADC consists of the capacitive-DAC(C-DAC), comparator, SAR logic and calibration circuit and it is possible to implement the low-power operation due to high-specification amplifier is not necessary and simple structure. The ADC determines the digital code corresponding to the analog input through binary search algorithm. Thus, SAR ADCs have relatively fast conversion speeds and high accuracy.

SAR ADCs are operated in charge-redistribution process. This converter uses a binary-weighted capacitor array with suitable their resolution. The operating principle is divided into three modes as shown in Figure 25. Firstly, in sampling mode, the switch SA is shorted as shown in Figure 25 (a), so that the top plate of the capacitor is connected to the ground, and the bottom plate of all the capacitors are connected to the analog input VA. Therefore, the charge on the whole capacitor is proportional to the analog input voltage and the charge amount can be express as :

$$Q_x = C_{total} \cdot V_A \quad (2.10)$$

where  $C_{total}$  is sum of all the capacitor. In the second hold mode, the switch SA is opened and the switch

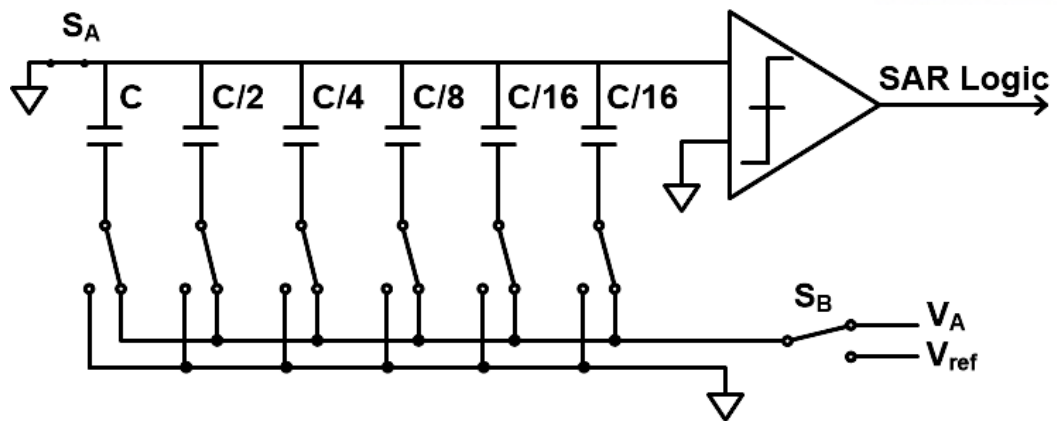
SB is connected to the reference voltage  $V_{ref}$  as shown in Figure 25 (b), and the bottom plate of all the capacitors is connected to the ground. At this time, the charges in the capacitor array are constant, and then the voltage  $V_x$  of the top plate has a value of  $-V_A$ . Finally, Figure 25 (c) presents charge-redistribution mode and binary searching begins. The switch S1 corresponding to the MSB is connected to  $V_{ref}$ , and the remaining switches are connected to the ground. The top plate voltage of  $V_x$  is increased by  $V_{ref}/2$ . Since the total charge amount is constant and the top plate voltage can be express as :

$$V_x = -V_A + V_{ref}/2 \quad (2.11)$$

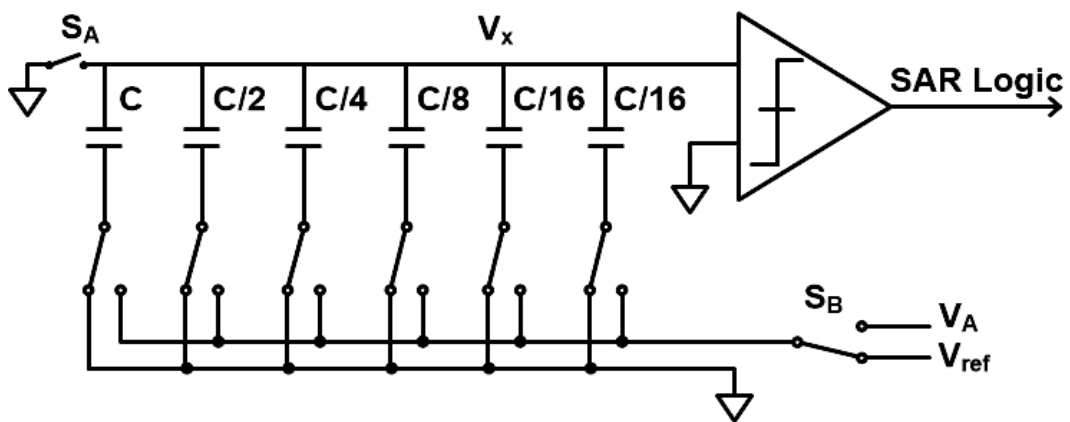
If the  $V_A$  is greater than  $V_{ref}/2$ ,  $V_x$  has a negative value, the output of the comparator is low, and switch S1 remains connected to  $V_{ref}$ . The results is shown that the MSB is 1. Conversely, if  $V_x$  has a positive value it means that  $V_A$  is less than  $V_{ref}/2$ , so switch S1 changes its connection from  $V_{ref}$  to ground. In this case, the MSB is determined as 0. After determining the MSB, the above process is repeated from switch S2 to switch S5 corresponding to LSB to determine remaining bits. The switch S6 corresponding to the termination capacitor used additionally remains connected to the ground during the whole charge-redistribution process. Figure 25 (c) shows the switch state indicating binary code 01100 after charge-redistribution mode has been completed.

SAR ADC is utilized for the system that requiring high linearity. Because the capacitors can be matched up to about 0.1 % in standard CMOS process. In order to improve the matching of the capacitor array, the segmented DAC is used in recent research. In addition, there is no static current in this architecture, it is advantages for low-power system implementation. However, the charge-redistribution ADC increases the ratio of the smallest capacitance to the largest capacitance and the total capacitance of the array as the resolution increases. For example, in the case of an N-bit converter, the size of the capacitor corresponding to MSB becomes  $2^{N-1}$  times of the unit capacitance. If the size of the capacitor is too large, the total area is increase and the operation speed decreases due to the increase of the input capacitance. In addition, there is a disadvantage that the arrangement of capacitors and the connection of signal lines becomes complicated during layout. Therefore, the SAR ADC has a limitation of resolution under the 10 bits and advanced techniques are researched in recent work such as noise shaping and calibration.

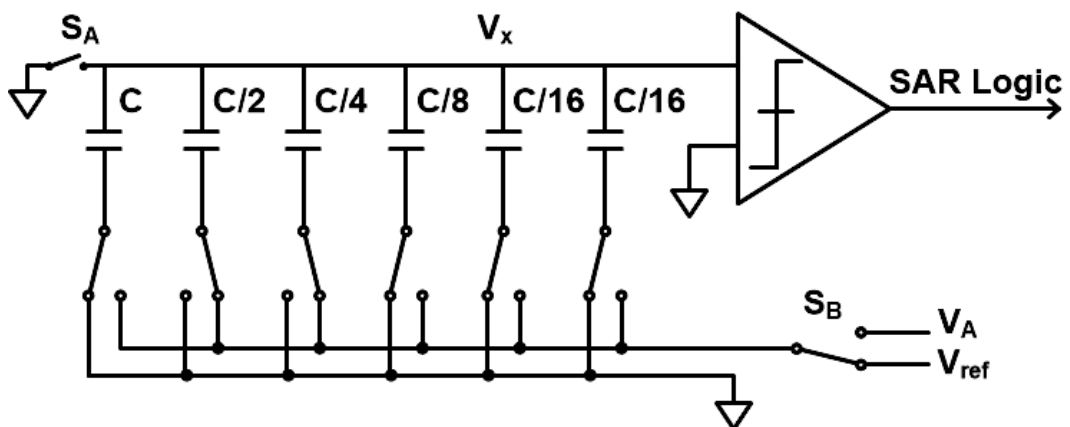




(a)



(b)



(c)

Fig. 25. 5 bits' SAR ADC conversion procedure (a) sampling, (b) hold, and (c) redistribution mode.

### 2.2.3 Improvement methodologies of SAR ADC

An Oversampling, laser trimming and self-calibration are essential techniques for the high-resolution SAR ADC design. The size mismatch of passive component of capacitor is design bottleneck for linearity of the ADC. The calibration can be attenuated the mismatch of capacitor binary weight that is occur with process variation from fabrication. An ADC employing an oversampling technique can convert one sample with multiple times conversion to obtain additional resolution, hut it has the disadvantage of lower conversion speed.

In case of C-DAC for design 10-bit SAR ADC,  $2^{10}$  unit capacitors are required, capacitor array limits the overall area and settling time due to MSB capacitance. The on-resistance of the switch is important to solve the settling problem and the sampling error due to the analog input, and the switch size for the driving strength become large. Previous research in JSSC 2016 [18] solve the switch driving power problem through using assist ADC, the upper bits are converted at once by parallel ADC. However, since the additional assist ADC is still need and the area of capacitor array problem has not been solved. Split C-DAC is used as a solution of this problem. When implementing 10-bits with split DAC, it can be configured in various MSB and LSB array combinations such as 5:5, 6:4, etc., and its structure can be selected in consideration of the immunity of capacitor mismatch by simulation in Figure 26. However, attenuation capacitor of split DAC is not an integer capacitance, adjusting the accurate capacitance is difficult to implement. Also, because of the parasitic that can occur during layout or fabrication, matching problems between MSB and LSB of C-DAC array may occur.

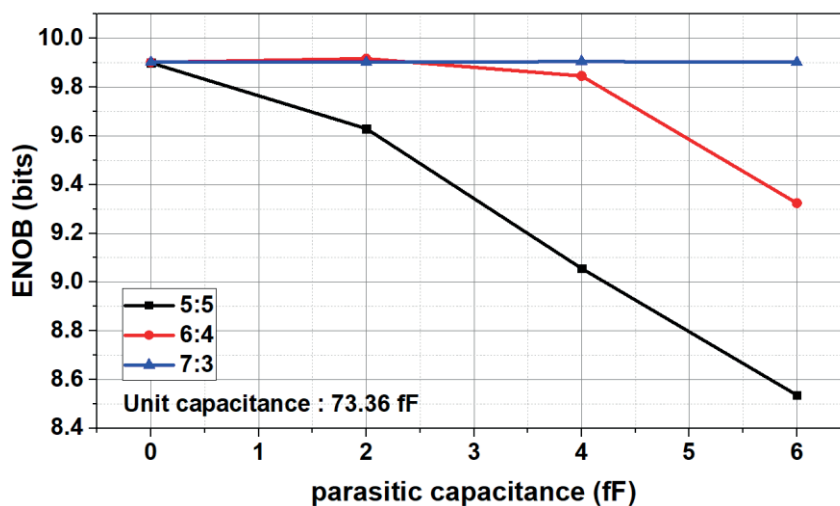
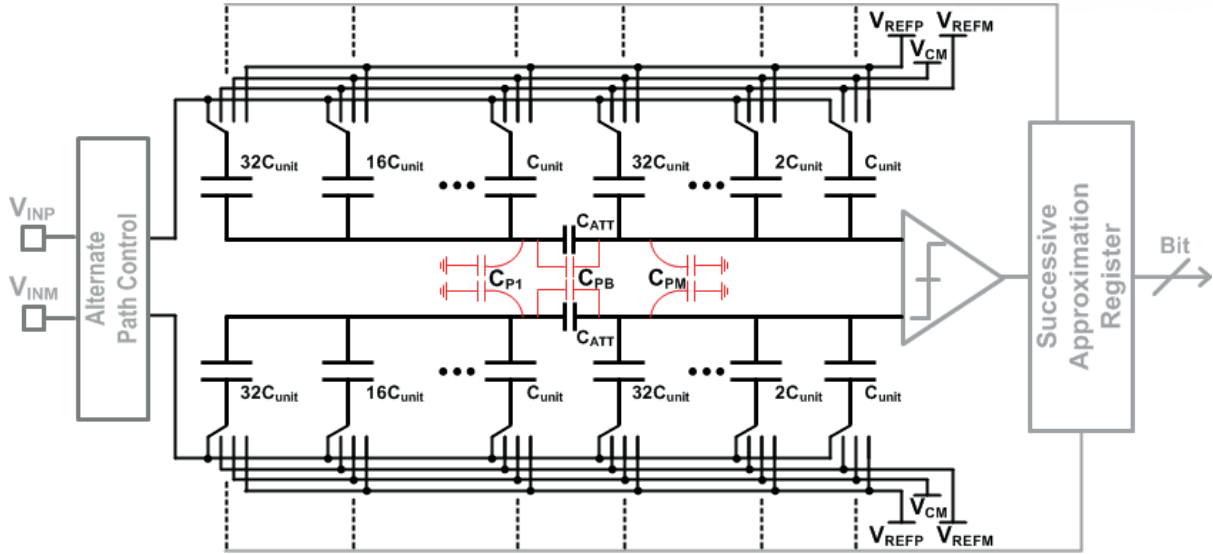


Fig. 26. Split DAC simulation results depending on combinations of MSB and LSB array.



**Fig. 27.** Effect of parasitic capacitance of split Capacitive DAC.

$C_{PM}$ ,  $C_{PB}$ , and  $C_{P1}$  are presented the parasitic capacitor that is produced to fabricate the chip in Figure 27.  $C_{PM}$  is not a big problem because this parasitic capacitor is affected to gain error, not linearity. However, since there arises a problem in linearity when  $C_{PL}$  occurs, calibration procedure is necessary to verify SAR ADC with 8-bits or more essentially. Actually, accurate resolution can be obtained without calibration up to 8-bits.

For instance, the general calibration method [19] that unit capacitance of MSB array is same with sum of LSB array capacitance in Figure 28. Two sets of capacitors are connected different voltage reference such as positive reference and negative reference. If the unit capacitance of MSB array is equal with total of LSB array capacitance, divided voltage is around common-mode voltage as half of difference between positive reference and negative reference. To implement higher resolution, MSB calibration is also necessary in Figure 28. Effective capacitance of left red box can express:

$$C_{EF} = \frac{(C_B + C_{P1}) \cdot 8C}{8C + C_L + C_{P1} + C_B + C_{PB}} \quad (2.12)$$

When  $C_{EF} = 1$ , if two sets of capacitors are perfectly matching.

$$C_L = 7 \cdot (C_B + C_{PB}) - 8 \cdot C - C_{P1} \quad (2.13)$$

Load capacitor  $C_L$  can be adjusted with sub-DAC array around that values. Also, dithering when sampling phase is utilized for C-DAC mismatch calibration [20]. The redundancy technique during conversion is used for linearity post-calibration, and time-interleaving or flash-assisted to increase the speed is also used [21]. In order to reduce power consumption, researches on switching energy of C-DAC are actively conducted [22,23].

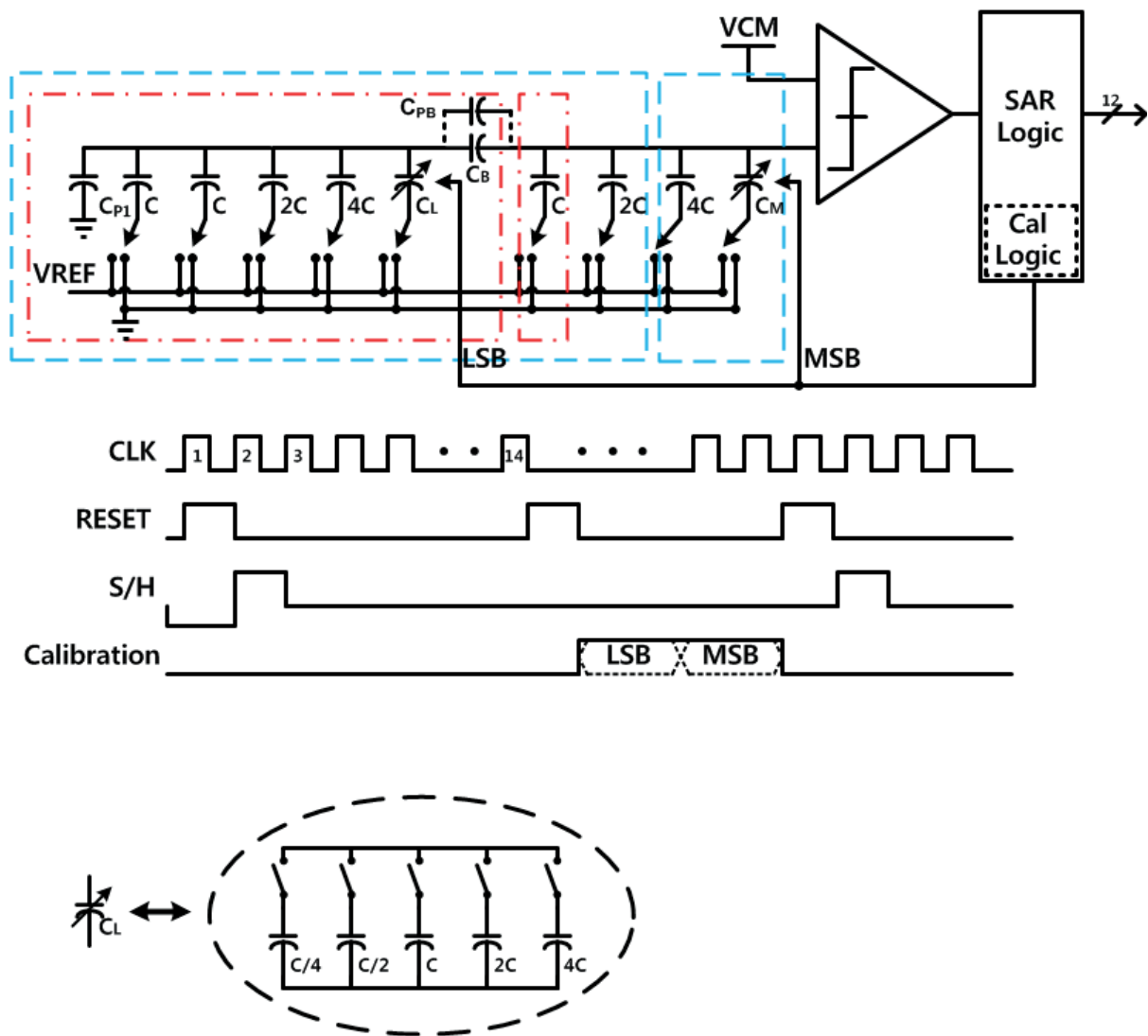


Fig. 28. The accurate split C-DAC mismatch calibration.

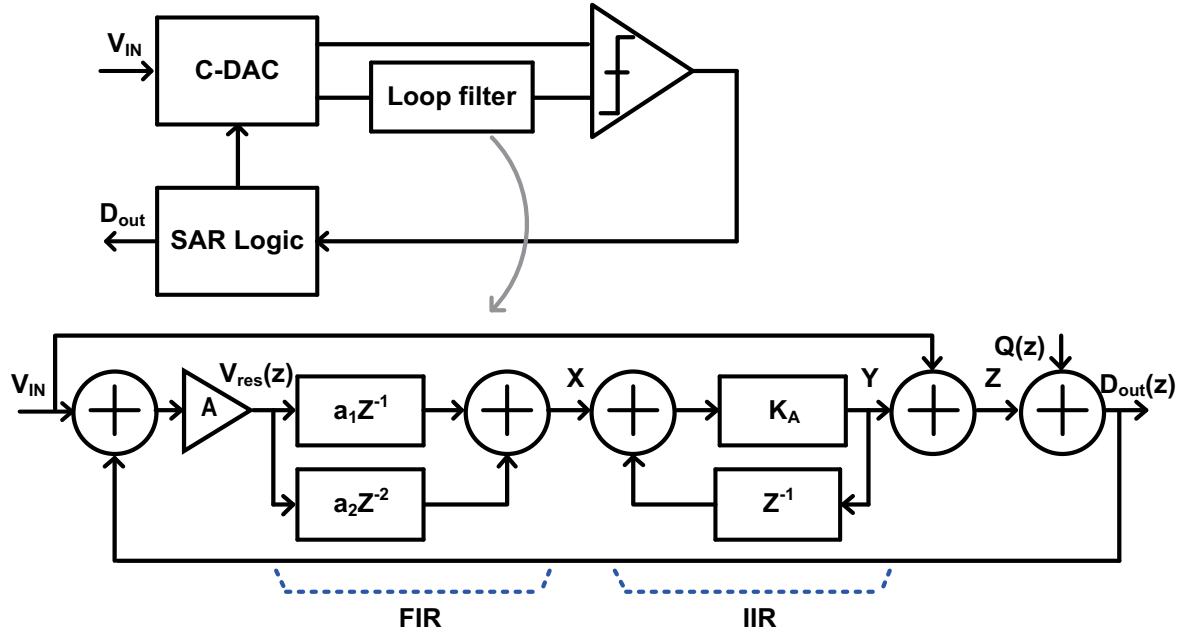


Fig. 29. SAR ADC with Noise shaping.

Adjusting the system specification can increase the efficiency of the system by using directly converting the digital code or ADC digital conversion. Noise shaping technology is being studied as a way to maximize selectivity and efficiency by supporting dual mode as low-power mode and high-resolution mode. In the case of existing SAR ADC, the resolution can be controlled. Since MSB is converted to LSB, it can be adjusted to the desired resolution. However, conventional method of resolution control is possible to configure only the resolution lower than the highest implementation resolution. Noise shaping is a way to get additional resolution with existing ADC. In the other words, ADC that consists of 10-bit C-DAC can be converted over the 10-bits with noise shaping.

Noise shaping circuit consists of integrator, comparator and 1-bit DAC as a method to get inspiration from sigma-delta modulation. In this case, a multi-bit DAC can be considered instead of a 1-bit DAC. The integrator can be implemented in an active form, but passive finite impulse response-infinite impulse response (FIR-IIR) filter can be obtained similar specification by using preamplifier [24]. Then, the residue voltage after SAR ADC conversion is integrated and compared at the comparator stage. In the Figure 29, SAR ADC with noise shaping architecture is expressed. Detailed equations are as follows:

$$V_{res}(z) = A(V_{in}(z) - D_{out}(z)) \quad (2.14)$$

$$X(z) = a_1 \cdot Z^{-1} \cdot V_{res}(z) + a_2 \cdot Z^{-2} \cdot V_{res}(z) \quad (2.15)$$

$$Y(z) = K_A(Z^{-1} \cdot Y(z) + X(z)) \quad (2.16)$$

$$\begin{aligned} D_{out}(z) &= Z(z) + Q(z) = V_{in}(z) + Y(z) + Q(z) \\ &= V_{in}(z) + K_A \cdot \frac{X(z)}{1 - K_A Z^{-1}} + Q(z) \end{aligned} \quad (2.17)$$

$$D_{out}(z) = V_{in}(z) + A \cdot \frac{1 - K_A Z^{-1}}{1 - K_A(a_1 - 1)Z^{-1} + K_A a_2 Z^{-2}} \cdot Q(z) \quad (2.18)$$

From the following equation results, the architecture was confirmed that there is a primary noise shaping effect. Also, passive loop filter can also obtain sufficient shaping effect through preamplifier's gain.

### 2.3 Prior arts of gas sensor system

Many kinds of hazardous gas sensing technique have been researched in [25]. A gas sensor is a device that detects a specific target gas in the air and converts it into an appropriate electrical signal according to the concentration. Gas sensors are used in a variety of applications such as gas detection, proactive diagnosis of food spoilage, and medical devices in environments where toxic gases are generated. In recent years, as the use of gas has increased from industrial sites to households, it is also used for hazardous substance sensing and risk management. Types of gas sensors classify sensing methods according to electrical signals [26-30]. There are infrared [26], photoionization [27], catalyst [28], electrochemical method [29], solid-state or metal-oxide semiconductor [30]. Because there are advantages and disadvantages to each gas sensing method, suitable structure for gas monitoring system are considered along their characteristics.

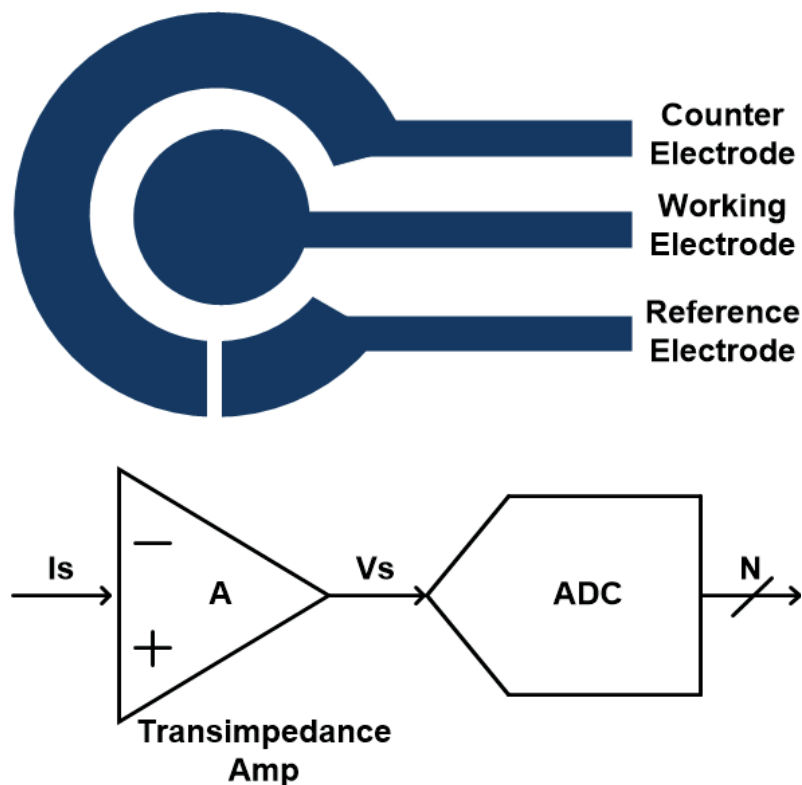


**Fig. 30.** The example of electrochemical gas sensing method.

The electrochemical gas sensor is a sensor that senses a change in the current value generated by the redox reaction between the anode and cathode in the electrolyte. An example of electrochemical gas sensor presents in the Figure 30. This sensing technique consists of a working and counter electrode where oxidation and reduction reaction are occurred, and a reference electrode for detecting the potentials that change with the redox reaction and keeping the potential constant. Electrochemical gas sensors can be classified into galvanic cell type and electrostatic type according to the operating principle. This sensing methodology shows superior properties in terms of response, sensitivity, selectivity, stability and reproducibility. However, there is a disadvantage that integration is difficult.

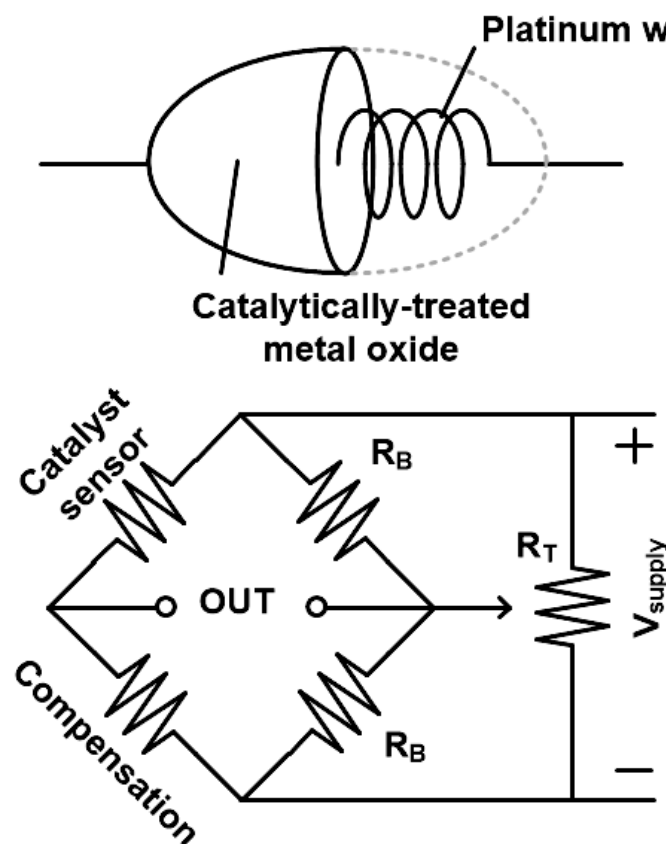
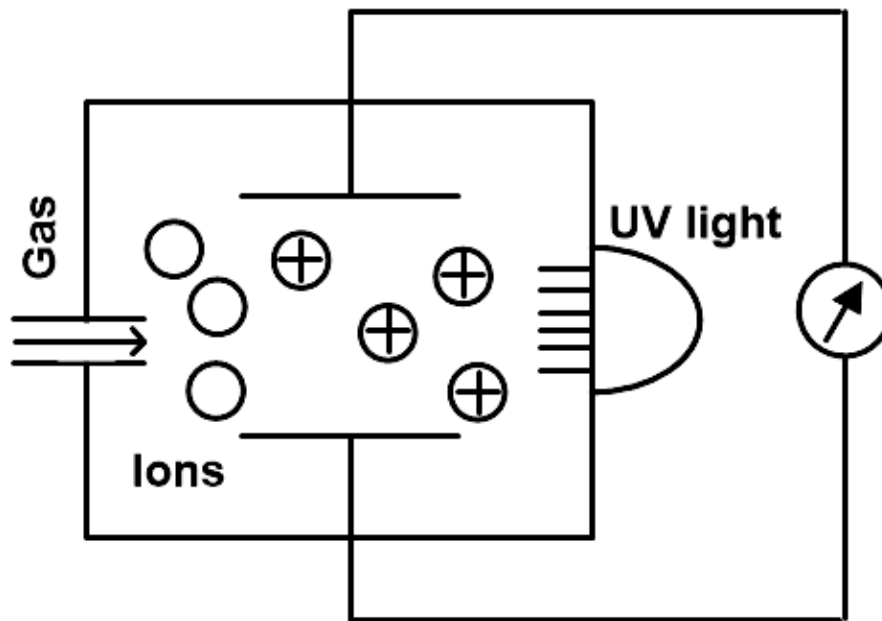


Fig. 31. The example of catalyst gas sensing method.

As shown in the Figure 31, the catalyst gas type and contact combustion type gas sensor are a method to detect the presence or concentration of gas by converting heat of reaction between combustible gas and oxygen into electrical signal. In the case of metal, the resistance increases as the temperature rises, and the gas concentration is sensed by detecting a change in the resistance of the metal due to heat



generated during the combustion reaction. The contact combustion sensor incorporates a metallic hot wire in the porous ceramics, and helps the catalyst react with the sensor in contact with the target gas. It is stable against ambient water vapor, humidity and temperature changes because it keeps temperature for chemical reaction. Although, the catalyst gas sensor is utilized for gas alarm, it has a disadvantage that it is difficult to detect a gas at high concentration.



**Fig. 32.** The example of photoionization gas sensing method.

Infrared or photoionization gas sensor are utilized to absorb the infrared light depending on its different gas types and concentrations as seen in Figure 32. Non-dispersive infrared (NDIR) is mainly used among these techniques. The NDIR method measures the gas concentration from the reduction of electrical signal according to the degree of infrared light absorption in a specific gas by using an infrared band-pass filter that existing between the infrared light source and the infrared sensor. Photoionization

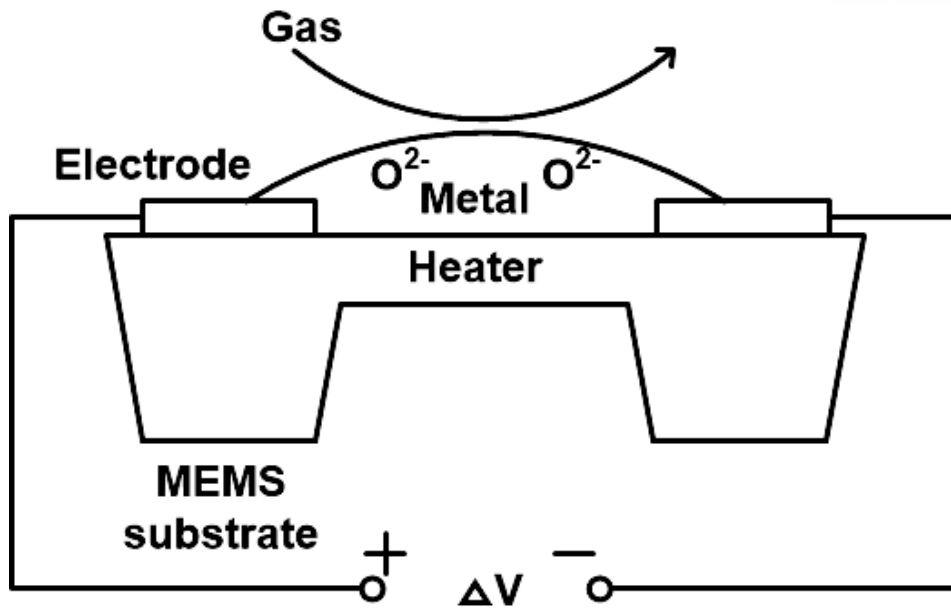


Fig. 33. The example of semiconductor gas sensing method.

gas sensors have measurement accuracy fast response time, but they are not suitable for portable application due to their large size.

As shown in the Figure 33, Semiconductor gas sensors detect the changing of electrical conductivity when gas contacts a semiconductor surface. The thickness of the depletion layer on the surface of the oxide semiconductor is changed due to the movement of electrons when a specific gas adsorbs at the oxide semiconductor, which causes a change in resistance. High temperature is required to shorten detection time, and  $SnO_2$  is used to make the structure. The semiconductor type gas sensor reacts with most toxic gas and combustible gas, and it is advantageous in that mass production is possible because the sensor is simple to manufacture due to the simple structure of the detection circuit. However, there is a drawback that the selectivity is deteriorated due to excellent reactivity.

Gas sensors suitable for IoT-based gas monitoring systems include electromechanical and semiconductor gas sensors. Especially, the semiconductor gas using the micro-electro-mechanical system (MEMS) technology is easy to integrate, mass-produce and realize low power. However, there is a disadvantage of poor selectivity, which I will show to improve pattern recognition with ROIC in the chapter III.

## Chapter III

### Readout Integrated Circuits and system Implementation

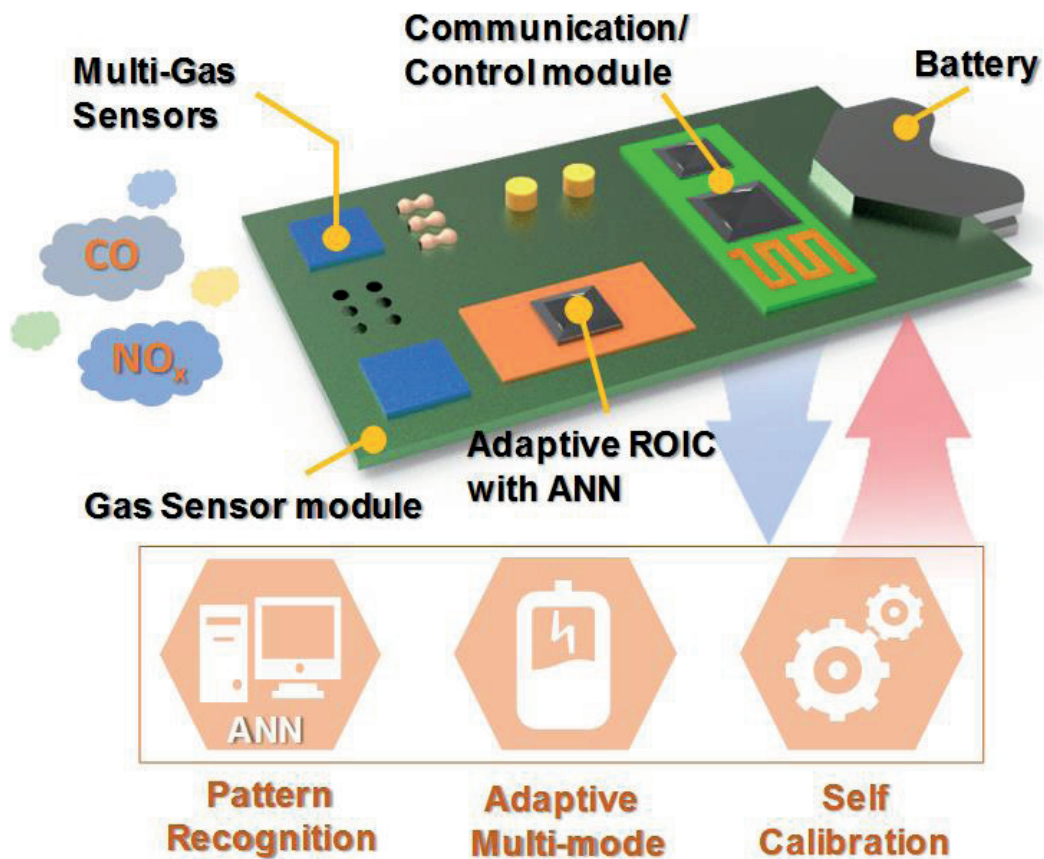


**Fig. 34.** Conceptual diagram of proposed gas sensor system.

In this chapter III, readout integrated circuits and gas monitoring system architecture are shown with detailed schematics and operations. ROIC can be divided into front-end part which senses the physical sensor signal as amplifier and filter and ADC which converts to digital code. MEMS-based gas sensor has resistance characteristics with the variation of gas types and concentrations. Thus, the RDC or resistive sensor interface is introduced with the pros and cons of their conversion method. In order to

improve the efficiency of the system, the ROIC is designed by adaptive multi-mode. Also, the ROIC is needed to support the sensing range and sensitivity calibration due to each sensor has different electrical characteristics. Therefore, 8-channels sensing are supported in the ROIC and external condition are gathered for pattern recognition and self-calibration technique. More detailed explanations are described in the chapter III.

### 3.1 Successive Approximation Register Analog-to-Digital Converter

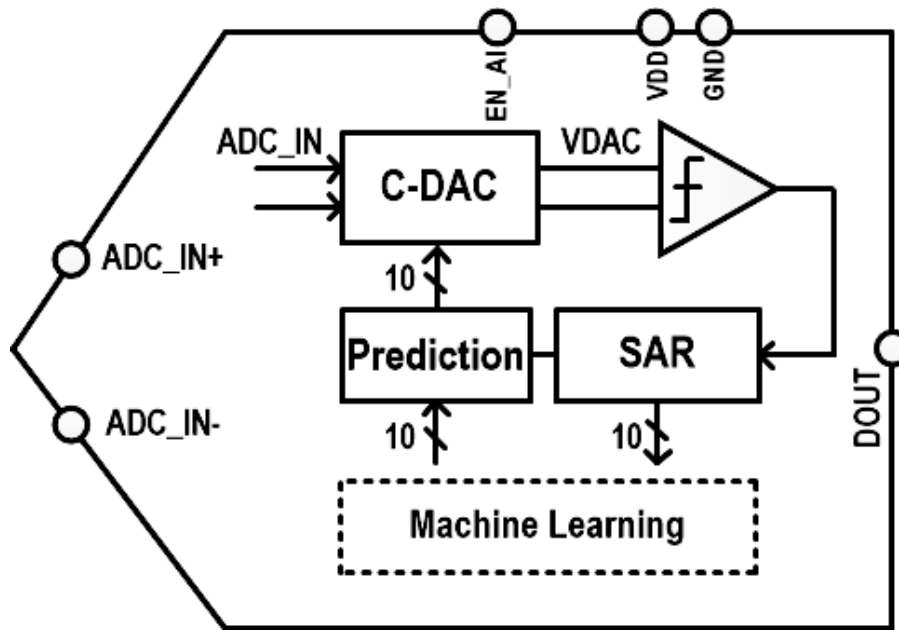
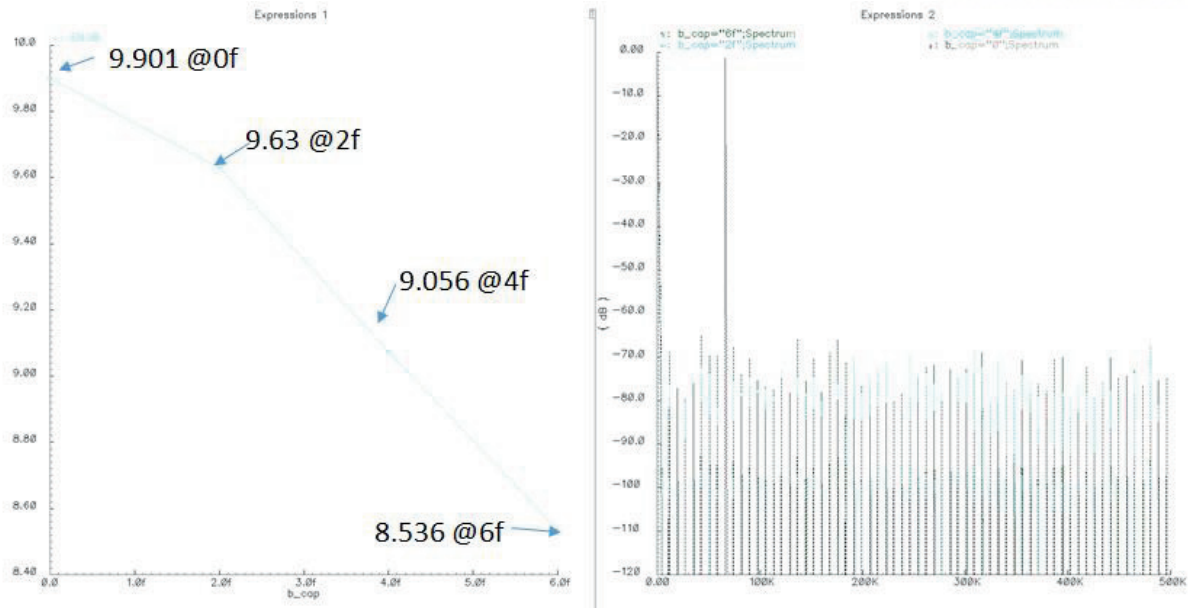


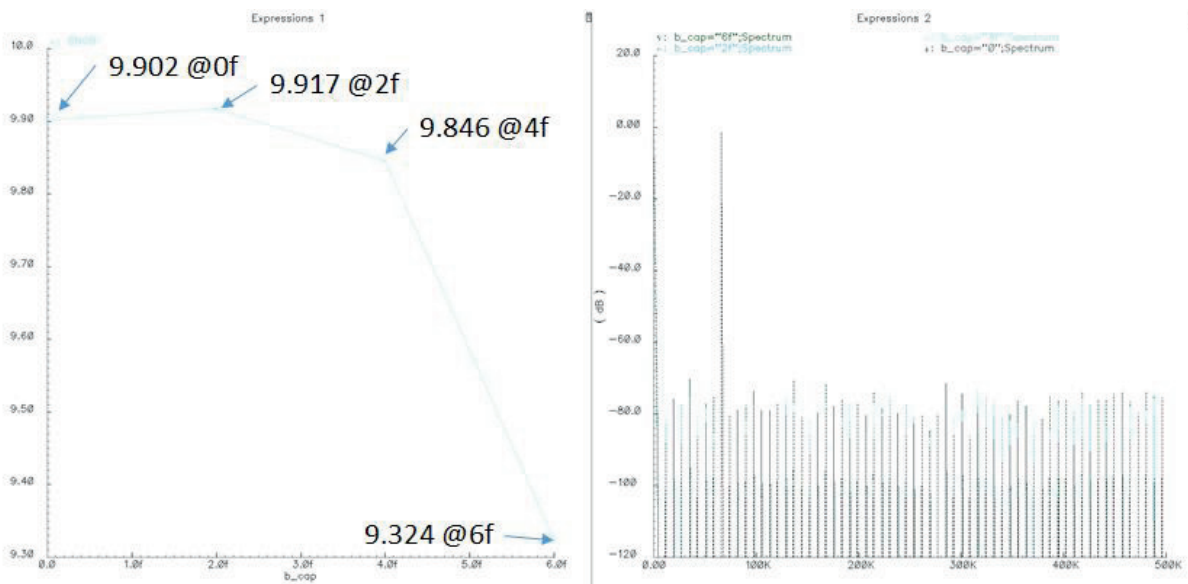
Fig. 35. Proposed prediction-based SAR ADC.

Figure 35 presents proposed prediction-based SAR ADC. The prediction-based SAR ADC is composed of C-DAC, comparator, SAR logic, and prediction logic. The prediction logic is utilized to control the C-DAC switching from the predicted code that generated in machine learning. The machine learning computation are operated into MATLAB and the wireless connectivity supports the transmitting and receiving their conversion and computation results.

With the prediction algorithm, SAR ADC is considered the C-DAC mismatch, settling problem in C-DAC, comparator offset for high performance implementation. Among of the design issues, the settling problem is important in high-speed application and comparator offset is not affect the spectrum because this error is constant. However, the mismatch is directly affected its effective resolution. In order to implement the high-resolution ADC, C-DAC needs the calibrate the mismatch. Usually, the



(a)



(b)

**Fig. 36.** Split-capacitor array and mismatch simulation with (a) 5:5 case, and (b) 6:4 case.

split capacitor array is utilized for the area and size mismatch over the 10-bit design. From simulation results, the Figure 36 shows the mismatch effect in the split capacitor DAC. The Figure 36 (a) consists of 5 bits MSB and 5 bits LSB and the Figure 36 (b) consists of 6 bits MSB and 4 bits LSB. The bridge capacitor of the split capacitor DAC is dominant parts for the overall linearity. The unit capacitor is 73.36fF in CMOS 180-nm process. We assume the mismatch up to 5 %. The simulation results present

the ENOB of ADC that composed of ideal component except the split capacitor DAC. From the results, the 5:5 case has about 1-bit degradation at 5 % mismatch and then the performance can't be guaranteed without additional calibration circuit. However, the 6:4 case has maximally 0.1-bit degradation into same condition the 5:5 case. Although the total capacitance of C-DAC is increased about x2, the 6:4 architecture has robustness to process variation. Additional parasitic that is occurred from layout are optimized into post-layout simulation. Also, the prediction-based SAR ADC logic and its conversion algorithm explains in the Section 3.4.3.

### 3.2 Correlated Double Sampling

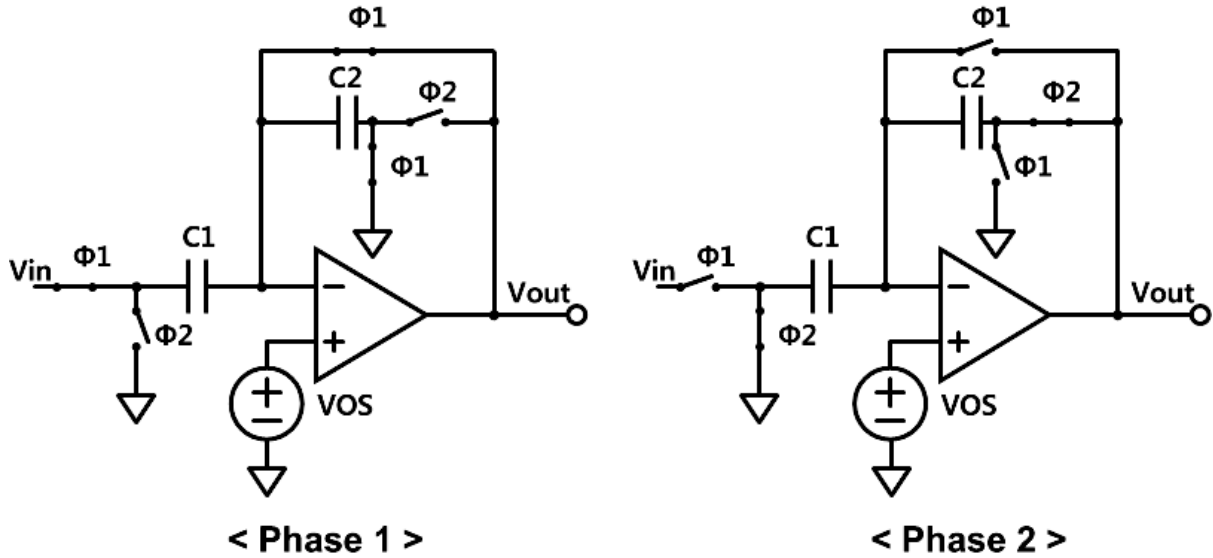


Fig. 37. Two phase operations of correlated double sampling.

Correlated double sampling is cancelled offset and sampled the electrical voltage [31]. This method is usually used to measure the output of sensor. CDS technique combine auto-zeroing with input sampling. Usually, CDS is procedure twice sampling. First, the only offset is sampled in phase 1. Secondly, phase 2 is sampling the desired input with the offset and subtracting the stored noise from the original signal. As a result, low-frequency noise can be reduced like DC offset, flicker noise. In the similar principle, chopper stabilization is a method of utilizing a carrier, modulating in a high frequency band with low-noise, and restoring the original signal through demodulation. CDS has a disadvantage of increasing the thermal noise in the high frequency band due to switching. In Figure 37, offset compensated gain stage with closed loop amplifier is explained the CDS operation. Charge conservation equation for phase 1 and phase 2 as follows:

$$Q_{1,i} + Q_{2,i} = Q_{1,f} + Q_{2,f} \quad (3.1)$$

$$C1 \cdot (VOS - Vin) + C2 \cdot VOS = C1 \cdot VOS + C2 \cdot (VOS - Vout) \quad (3.2)$$



$$- C1 \cdot V_{in} = - C2 \cdot V_{out} \quad (3.3)$$

$$\frac{V_{out}}{V_{in}} = \frac{C1}{C2} \quad (3.4)$$

However, most of offset is cancelled by CDS step, finite gain error and residual offset are remained.

### 3.3 Resistance-to-Digital Converter

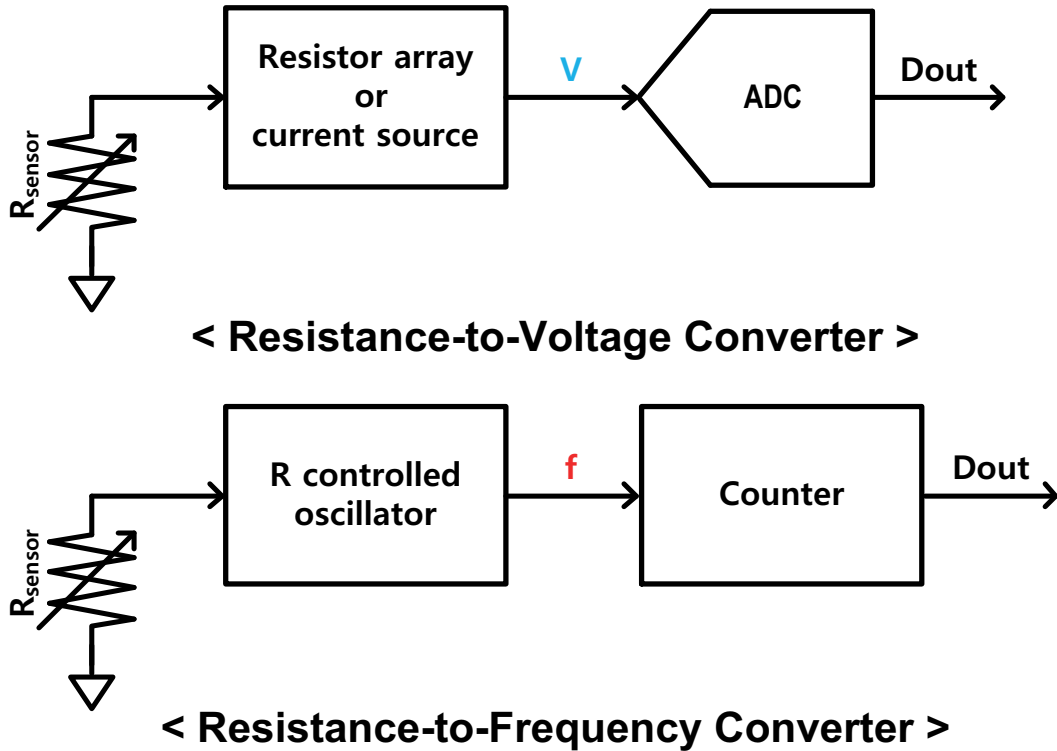


Fig. 38. Conventional block diagram of resistance-to-voltage and resistance-to-frequency converter.

In the case of an ADC, if it is converted an analog signal in the form of a voltage or a current to a digital code, the RDC senses the resistance and converts it into a digital code along with sampled value. In the Figure 38, RDC can be roughly divided into two types of resistance-to-voltage (R-to-V) and resistance-to-frequency (R-to-F) [2,32]. Generally, implementation of R-to-V creates a residue voltage with reference resistor or current source and generate a digital code using ADC. But, since the sensing range is limited by single reference, resistor array or current DAC is used to compensate the residue voltage. At this time, RDC is possible to directly utilize the generated digital code and can be sensed a wide range of resistance variation including ADC's conversion. Current source has higher precision than the resistor array, and then RDC with current DAC can be realized the high-resolution. Using such a combination resistor array with current source, RDC operates two step conversion as coarse conversion with resistor array and fine conversion with current DAC.

Another method, R-to-F is utilized difference in current generated by resistance to capacitive load via charge & discharge time. The generated frequency can be converted into a digital code by counting the time. The R-to-F converter does not require a complicated DAC and is mostly composed of digital block, which can reduce power consumption. However, the resolution is lowered due to the non-linearity in charge-discharge process following exponential characteristic.

### 3.3.1 Resistive DAC

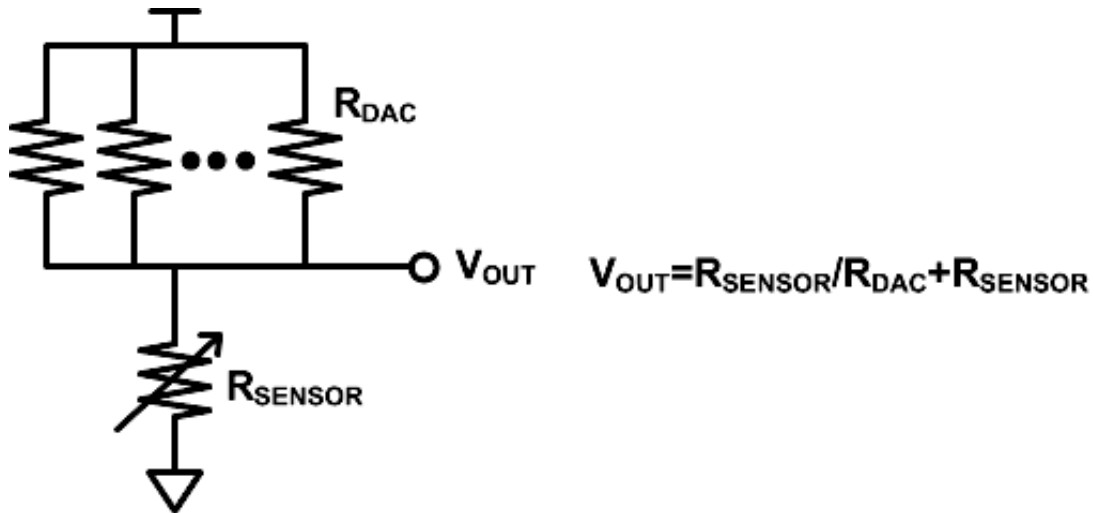


Fig. 39. RDC with resistive DAC circuit and divided output voltage.

If the voltage is converted to a voltage using the resistance of one reference, linearity is guaranteed without mismatch the resistance and high sensitivity can be obtained. However, the performance may be degraded suddenly beyond a certain range, and the desired voltage value can't be obtained properly. If the resistive DAC has a configuration of about 8-bits, wide range conversion is provided.

When dividing by using the resistance of the sensor and the resistance of the reference array, the voltage is generated due to the difference of both resistances. Divided voltage and resistive DAC circuit are presented in Figure 39. By comparing with the reference that is usually common mode voltage according to the high or low voltage of the residue voltage, the resistance of the reference array is adjusted by control logic and the reference voltage is approached to common mode voltage. This scheme is similar with SAR searching algorithm. The results can be obtained by comparing the approximate range to the precise range while changing from a high resistance to a low resistance. In this method, as the value of the sensing resistor increases, the current flowing decreases, which makes it susceptible to noise and the sensitivity deteriorates. Also, the resistance of the LSB in resistive DAC is decided the minimum sensing range that can be compared. If the unit resistance is reduced, there is a disadvantage that the accuracy can be increased but the sensing range is reduced. In addition, the static current flowing during sensing also increases.

### 3.3.2 Current DAC

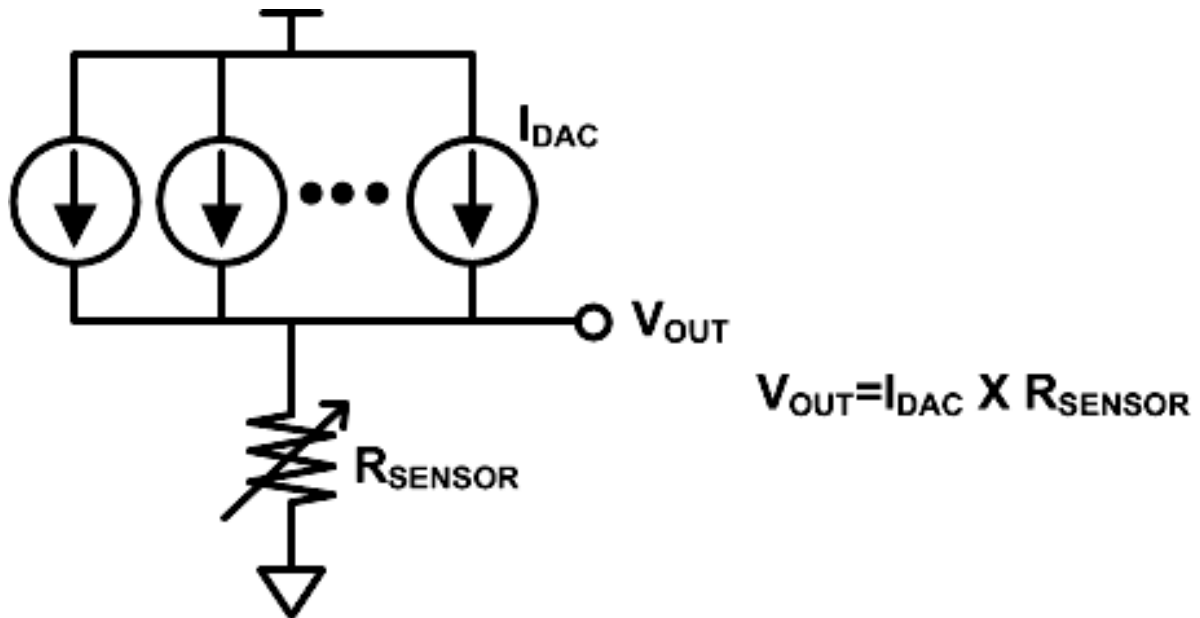


Fig. 40. Operation of RDC with current DAC.

Another way which generated residue voltage is to use current DAC to flow the current through the resistor in Figure 40. Conventionally, resistance finds from a high current source to a low current source, it that case the residue voltage at which resistance can be exceed the supply voltage depending on the situation. In the worst case, there is a risk that the transistor is destroyed because gate voltage of the comparator is over the limitation. Therefore, LSB first comparison algorithm can be eliminate the break-down of transistor [33].

### 3.4 Proposed Gas monitoring system

Gas sensor senses the concentration of gas and produces the electrical signals along its concentration. The sensor provides useful information through the signal processing and communication module in the environmental system. The gas monitoring system can be utilized environmental pollution monitoring, food corruption diagnosis, medical treatment and indoor/outdoor air quality management at homes, automotive application and industrial field. Recently, as the use of various gases in industrial field and home appliances has increased, the development of portable sensor systems is required. In addition, a monitoring system is necessary to prevent the hazardous gases during breathing in daily life. The world gas sensor market is expected that the global annual growth rate (CAGR) will increase by 6.45% and will increase to 3.4 billion USD in 2022 [34]. Detection of air quality and environmental contamination can also prevent diseases related to respiratory organs and can also reduce the risk of explosion and fatal hazardous gases at industrial area [35].

Conventional gas sensors can be sensed in various methods such as electrochemical measurement, photoionization detectors, solid state/metal oxide semiconductor, laser, infrared and etc. Since various kinds of gases such as CO, CO<sub>2</sub>, NO<sub>x</sub>, SO<sub>x</sub>, VOC, methane exists in the surroundings, sensor system which capable of sensing various kinds of gases are needed. However, the gas sensor monitoring system has problem of implementation as power consumption and module size. I already mentioned about various gas sensing methodology in Section 2.3. Gas sensors have different pros and cons and they are utilized to follow their application. In addition, sensing gas types are widely supported to prevent the unpredicted situation with multiple hazardous gas. Energy efficient conversion and various kinds supported sensor are important for daily sensed systems.

Among the multiple techniques of sensing gas, the electrochemical and MEMS methodology is more efficient by comparing its reactivity, power consumption and size. The electrochemical method is to detect the gas concentration by sensing the current or voltage generated by the chemical reaction of the gas. In the MEMS sensing method, the gas reacts with the substance coated on the nanowire to change the resistance of the wire and measures the change of resistance. Both systems are suitable for miniaturization, low power consumption and moderate selectivity. Especially, MEMS sensors are possible to integrate with ROIC, and then module has miniaturization, reconfigurability of sensor and specification and MEMS sensor is also reduced the static heating current to utilize the micro heater. Miniaturized gas sensor system based on the MEMS sensor is not only free to install, but it can be mounted in a portable form. Low-power consumption ROIC implementation and efficient operation

algorithm are required with micro heater of sensor for low-power system. As monitoring systems generate continuous and huge data, the construction of data-based algorithms is efficient. An artificial intelligence (AI) algorithm with training can help the ROIC operation efficiently, and it is possible to implement a smart sensor system for pattern recognition of gas. Based on the data, the ROIC can operate dual-mode as low-power and high-resolution mode, and the conversion cycle of analog-to-digital converter (ADC) can be reduced by using the prediction algorithm.

### 3.4.1 System Architecture

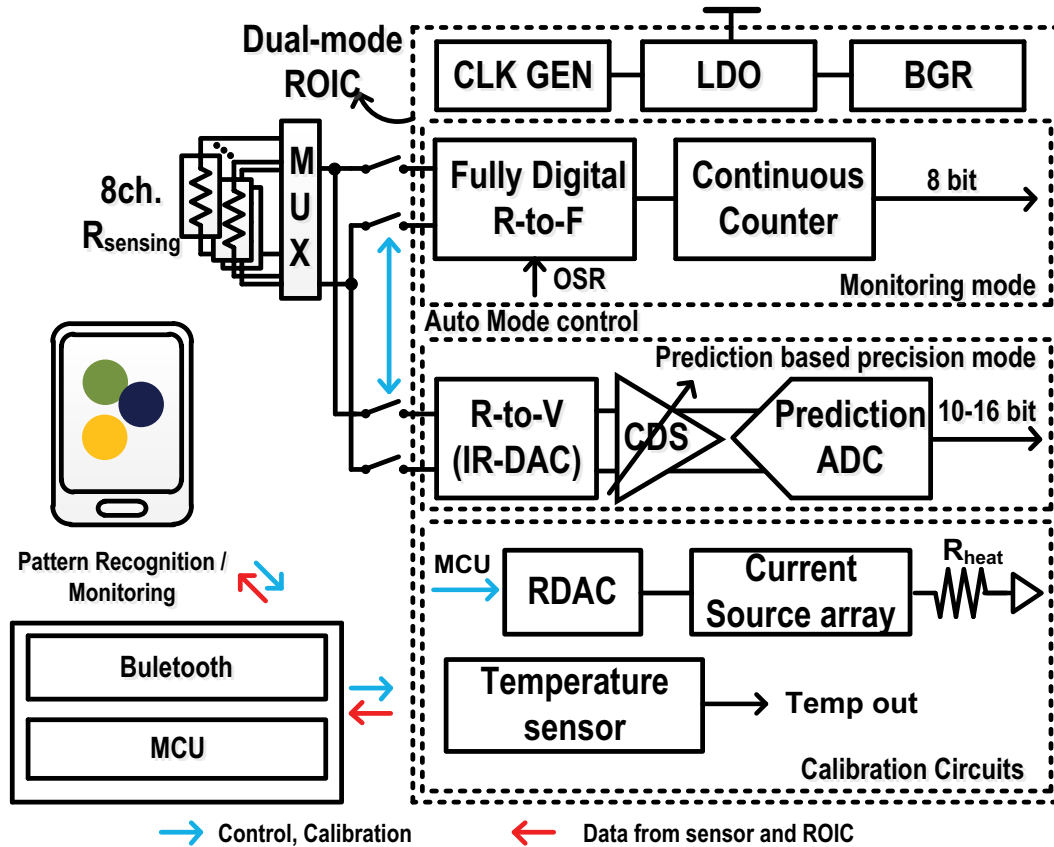


Fig. 41. Proposed gas sensor system block diagram.

Figure 41 shows a proposed multi-channel wireless gas sensor system which consists of a ROIC, MEMS sensor, sensing devices, a MCU, and communication module. MEMS types of gas sensors have various kind of gases depending on its coating substance. Bluetooth provides the wireless connectivity with mobile, and laptop. Also, pattern recognition, adaptive mode control and prediction code for SAR ADC are communicated through Bluetooth.

Depending on the type of hazardous gas, the effect on the human body and the permissible concentration is different. For example,  $H_2S$  may be dangerous by immediate reaction and may be a problem when exposed to CO for a long time. Thus, exposure level and permissible concentration of the different gases are judged by TWA and STEL. In the Figure 42, the TWA is set at an acceptable concentration and an exposure time of 8 hours for each gas type, and in the case of STEL, it represents



the unprotected concentration within 15 minutes and immediately judges the dangerous gas. Therefore, since the permissible concentration and the exposure time vary depending on the type of gas and dual-mode gas monitoring system provides the efficient method for recognizing the both TWA and STEL. Also, the proposed system that contained the battery is improving the portability and protecting the worker in dangerous environment.

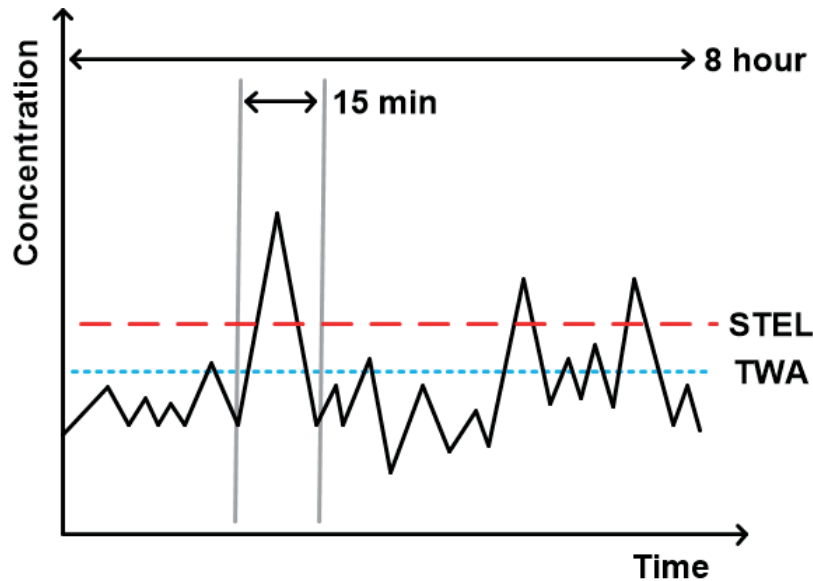


Fig. 42. Definition of the time weighted average and the short time exposure limits. [4]

In addition, the IoT can be applied to the wide-field applications through the characteristics which is the intelligent processing, reconfigurable sensing and effective management. For the monitoring the worker's environment or personal daily life, the gas monitoring system requires the long-term monitoring, portable, low cost and low maintenance. At least 8 hours running time is required to measure the TWA. In this system, the coin battery is embedded to support the wireless functionality and it has 120mAh capacity. 3.5 working days are supported in the worst-case of precision mode ROIC and the only monitoring mode operates during over the 5 years. Therefore, the long-term monitoring is satisfied by utilizing the proposed dual-mode design and its optimization algorithm with ANN. The efficient and intelligent operation improves the performance further against the conventional system-level design.

Figure 43 presents operational flow with learning-based scheme. The neural network is computed into MATLAB based on the channel information of adaptive ROIC, its digital output code and

temperature/humidity from the sensors. At the beginning of the sensing, monitoring mode starts with low-power consumption and minimum accuracy. The learning algorithm analyzes its monitoring-mode's outputs through the pattern recognition technique. According to the results, the system is decided the switching to precision mode or not.

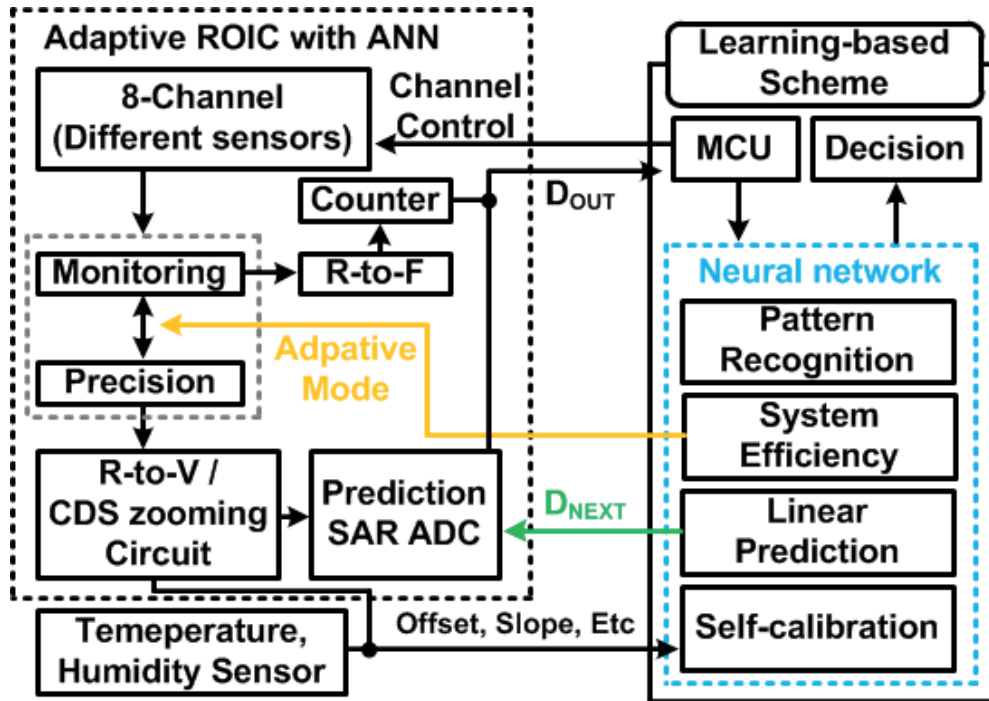


Fig. 43. Operational flow for performance optimization and self-calibration.

### 3.4.2 Dual-mode ROIC implementation

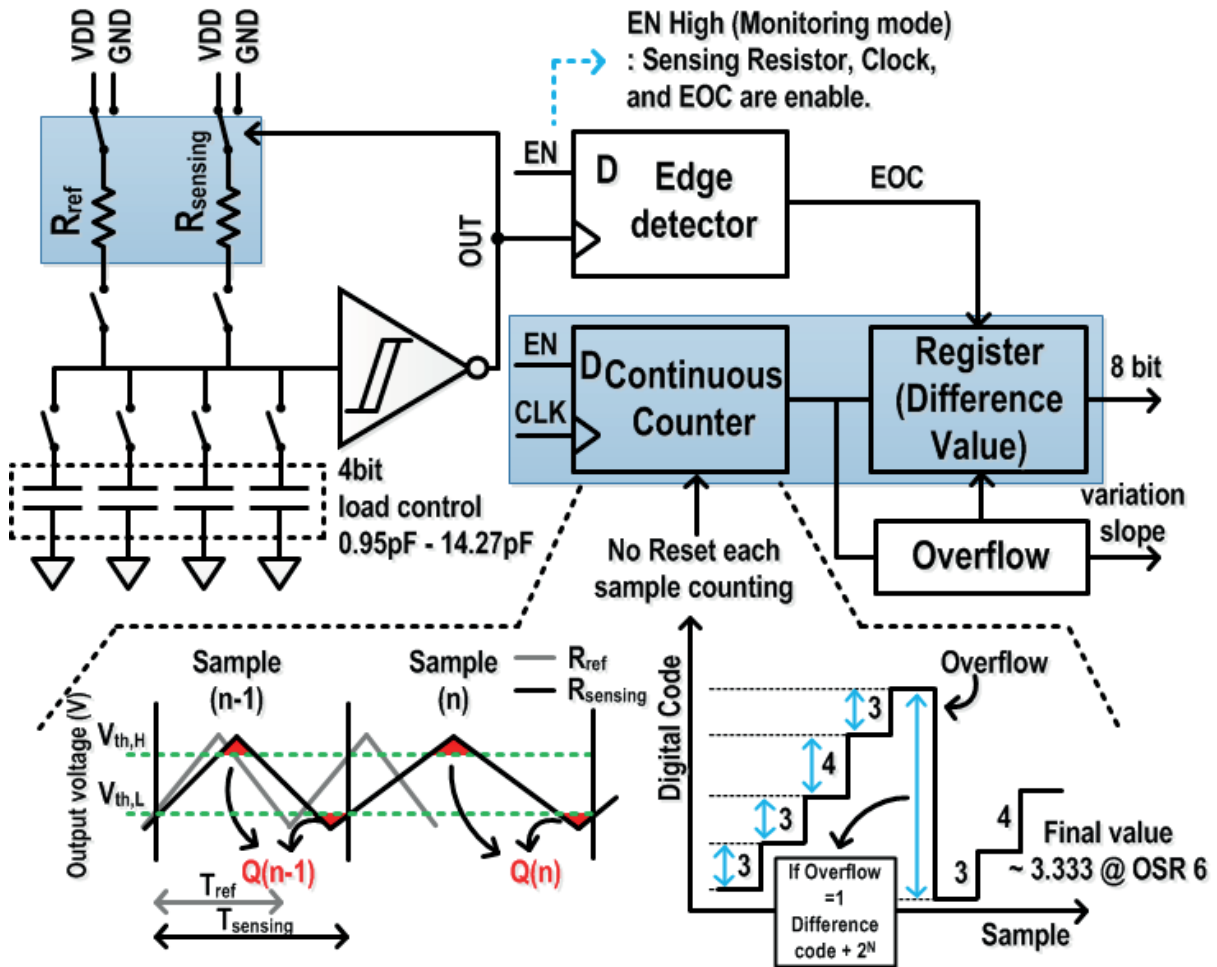


Fig. 44. Proposed oscillation-based RDC block diagram.

This dual-mode gas sensor system is implemented to support a real-time mobile interface, providing wireless connectivity to smartphone by utilizing the Bluetooth. It includes in-house MEM sensing devices that has significant advantages of low power, fast response, and miniaturization, compared with other types of gas sensors. Based on a common device structure of the suspended carbon nanowire, they can detect various gases such as dihydrogen ( $H_2$ ), methane ( $CH_4$ ), carbon monoxide (CO), nitrogen oxides ( $NO_x$ ), and sulfur oxide ( $SO_x$ ) by changing their coating materials. In addition, using a micro heater, measurement can be performed by heating with micro ampere instead of a conventional sensor

that consumes static several mA to tens of mA. The integrated MEMS sensor is less sensitive to change in temperature and humidity than commercially available sensors, but its value may change depending on temperature and humidity. For calibrating their device characteristics depending temperature and humidity, a commercial sensor component for temperature and humidity is included together in the sensor interface.

The oscillation-based RDC, which is an R-to-F method, converts the charging-discharging time according to the resistance value into a digital code. In the case of oscillation-based RDC in [7], fully charging and discharging time are measured with delay cell. The charging-discharging time of capacitor load can be expressed by exponential function. When converting the digital code along with whole resistance range, linearity of RDC is slightly decreased.

Figure 44 shows a proposed fully digital RDC circuit inside the ROIC and its monitoring mode operation. It is a kind of R-to-F converter based on the relaxation oscillator, implementing charge reusing scheme for low power. Since its inherent charging operation is relatively nonlinear, it is designed to utilize partial linear range that is set by two threshold voltages of  $V_{th,H}$  and  $V_{th,L}$ . Initially, small current through a reference resistance ( $R_{ref}$ ) is charged to a load capacitor whose charge is reused for the following discharging waveform by switching the supply with the ground. The resistance of the gas sensor device ( $R_{sensing}$ ) replaces the  $R_{ref}$ , and then the same operation is repeated. Monitoring mode is operated by rational scheme that is express as:

$$\frac{R_{sensing}}{R_{reference}} = \frac{T_{sensing}}{T_{reference}} \quad (3.5)$$

The rational relation is provided the robustness characteristics about variation of process, voltage and temperature. Because resistors have same variation about that external environment changes. Both R-to-F waveform's periods are compared by utilizing a continuous counter which does not reset for every sample period, but keeps counting, giving the deviation from the previous value as the output. During this continuous counting, instant RDC measurement errors are suppressed by quantization noise integration and oversampling. For supporting wide range of sensor resistance from  $250\Omega$  to  $2M\Omega$ , the load capacitor is designed to be adjustable from  $0.96\text{ pF}$  to  $14.27\text{ pF}$  by utilizing a 4-bit capacitor array. Up to 9 bits can be resolved by overflow signal. The current flowed in the part excluding the resistor of sensor can be processed with extremely small  $\mu\text{W}$  and it can be a suitable structure for monitoring

system.

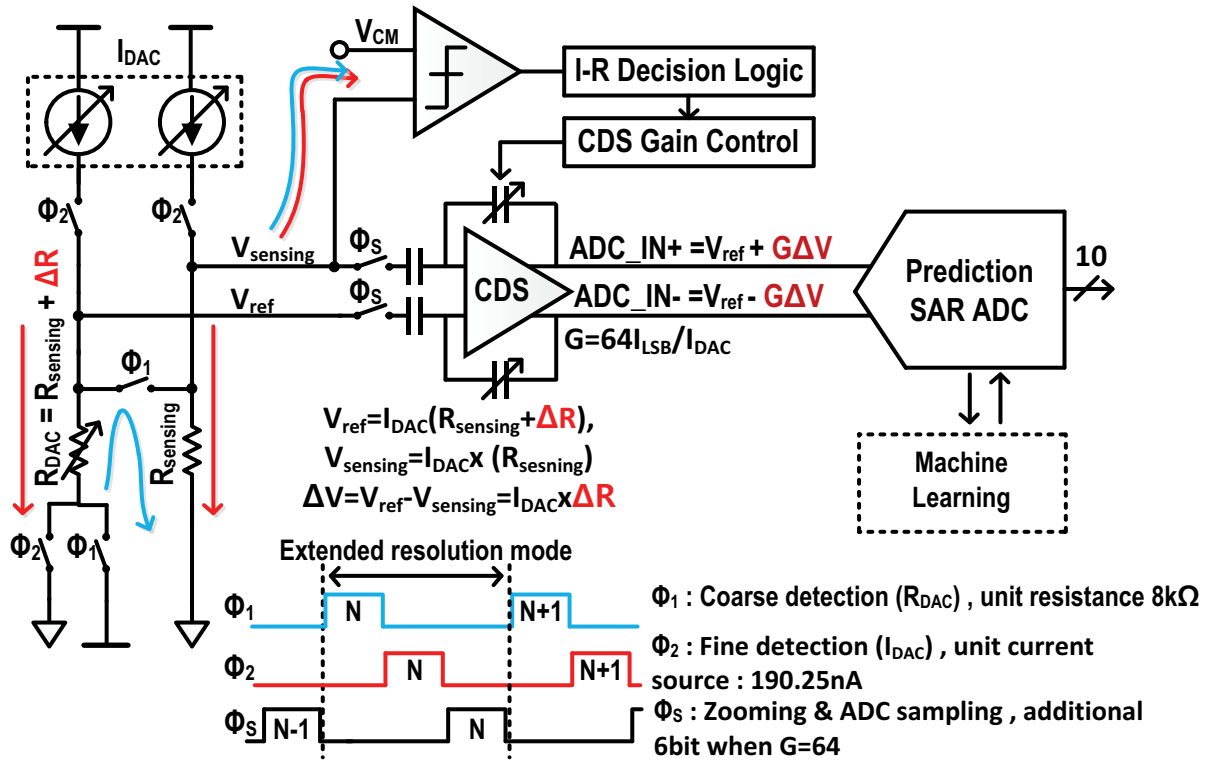


Fig. 45. Block diagram of precision mode and CDS zooming scheme.

Figure 45 presents circuit implementation and operation for the precision mode. The resolution extension of the R-to-V detection is implemented by a proposed differential CDS zooming structure, being augmented by adopting the prediction-based SAR ADC. For calibration of resistive sensors, their offset (or base resistance) and characteristic curve slope (or sensitivity) need to be adjusted properly. Firstly, in terms of the base resistance calibration, the proposed front-end circuit is designed to perform low-resolution RDC by utilizing a resistive divider that is composed of the resistive DAC and the resistive sensor. A SAR-based binary search algorithm is performed, and then this RDC result gives detection result on the base resistance of the sensor. Secondly, for high-precision detection, this work utilizes the current-source-based R-to-V conversion in the front-end circuit, and two programmable current sources are applied to the resistive DAC and the sensor so that it can provide pseudo-differential linear detection on the resistive variation information from the base resistance,  $I_{DAC} \times (R_{SENSOR} - R_{DAC})$ , achieving better linearity and noise immunity. And this current source is also automatically programmed to locate the output voltage around the common voltage through another binary-search routine. Thirdly,

this pseudo-differential output is amplified in the following CDS zooming circuit, and then digitally converted in the following differential ADC. Therefore, the characteristic curve slope can be calibrated by adjusting the current source for fine calibration, and the CDS-zooming gain is adjusted to control the sensor sensitivity depending on its applications. These procedures are also indicated in Figure. 45, where three-phase operations of base resistance detection, fine detection and zooming are included.

The detail operation consists of three phases. First, the coarse detection of  $R_{\text{sensing}}$  is performed by resistive SAR operation which is based on the comparison between a common-mode voltage ( $V_{\text{CM}}$ ) and a voltage-divider output of an 8-bit resistive digital-to-analog converter ( $R_{\text{DAC}}$ ) and a target sensor ( $R_{\text{sensing}}$ ). Then, from this coarse detection results, two current sources of 8-bit current digital-to-analog converters ( $I_{\text{DAC}}$ ) are optimally programmed to locate  $R_{\text{DAC}}$  around  $R_{\text{sensing}}$  whose difference ( $\Delta R$ ). Conventional sensing ROIC is necessary for higher resolution ADC than resolution of front-end due to sense and convert the difference of residue in ADC directly. To relax the design requirement of ADC, variable gain CDS can help to zoom the residue and give an additional margin for converting. The difference is zoomed in the following CDS amplification and digitized in next following ADC. The CDS gain of the zooming amplifier is decided by utilizing the fine detection results to give it range extension. At the same time, a single-ended resistance variance is converted to a differential voltage signal, achieving good immunity against various noises. After gas concentrations are sensed with the precision mode, measured resistance can be express depending on its digital code of  $I_{\text{DAC}}$ . If the digital code of  $I_{\text{DAC}}$  is exceed the 63, measured resistance can be converted into equation as

$$R_{\text{measured}} = D_{\text{RDAC}} \cdot R_{\text{LSB}} + \frac{(V_{\text{CM}} - D_{\text{ADC}} \cdot V_{\text{LSB,ADC}}) \cdot 63}{D_{\text{IDAC}} \cdot I_{\text{LSB}} \cdot 64} \quad (3.6)$$

Also, the digital code of  $I_{\text{DAC}}$  is less than 63, measured resistance can express as equation such as

$$R_{\text{measured}} = D_{\text{RDAC}} \cdot R_{\text{LSB}} + \frac{(V_{\text{CM}} - D_{\text{ADC}} \cdot V_{\text{LSB,ADC}}) \cdot D_{\text{IDAC}}}{D_{\text{IDAC}} \cdot I_{\text{LSB}} \cdot 64} \quad (3.7)$$

$$R_{\text{measured}} = D_{\text{RDAC}} \cdot R_{\text{LSB}} + \frac{(V_{\text{CM}} - D_{\text{ADC}} \cdot V_{\text{LSB,ADC}})}{I_{\text{LSB}} \cdot 64} \quad (3.8)$$

In the case of upper equation,  $D_{IDAC}$  can be eliminated as final equation. Thus, CDS zooming can be implemented with high resolution by reducing the influence of  $I_{DAC}$ .

Conventional resistive gas sensors have different base resistances and characteristic curve-slopes, their front-end detection circuits such as resistive-divider or Wheatstone-bridge front-end circuits utilize the variable resistor to locate the output voltage around the common-mode voltage, resulting in calibrations for better linearity. Then, their small resistive variations due to sensing operations are converted into digital codes through the following ADC. However, these conventional variable-resistor-based calibration methods are not easy to include various ambient effects including temperature and humidity, and additional calibration adjustments need to be manually performed with respect to each sensor. This is why the self-calibration is necessary to support various sensors and also to make sensor maintenance much easier. In this way, the offset (or base resistance) and the slope (or sensitivity) can be calibrated. Then, the system-level pattern recognition algorithm gives the gas-type information and also environmental information on temperature and humidity, and the final concentration is self-calibrated by correcting the overall results. In realizing the pattern recognition, the training procedure is performed including temperature and humidity information and gas concentration.

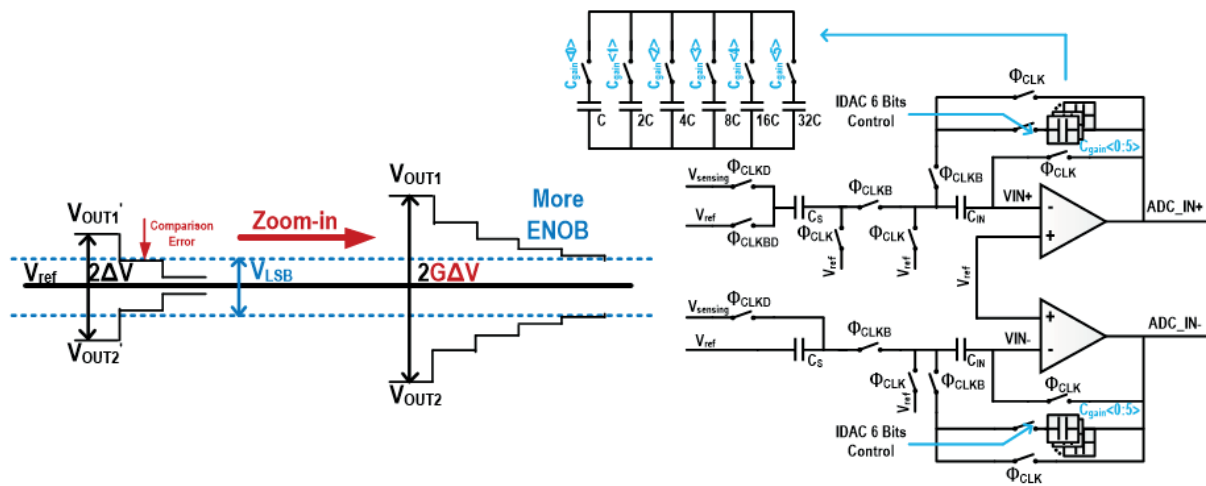


**Fig. 46.** Effect and Operation principle of CDS zooming.

In the Figure 46, circuit-level implementation of CDS zooming amplifier is presented. Since the range of residue is known according to the digital code of current DAC, it is used to control CDS gain.

This code avoids the situation where the amplifying signals saturate to supply voltage or ground after CDS zooming. Only 6 bits of the 8 bits current DAC provide 1 to 64 times gain of CDS. The MCU is collected the digital codes of resistive DAC, current DAC, and ADC, and then measured resistance is obtained finally. This proposed differential CDS zooming operation is designed to give additional 6-bit resolution versus conventional R-to-V conversion.



### 3.4.3 Prediction SAR ADC algorithm

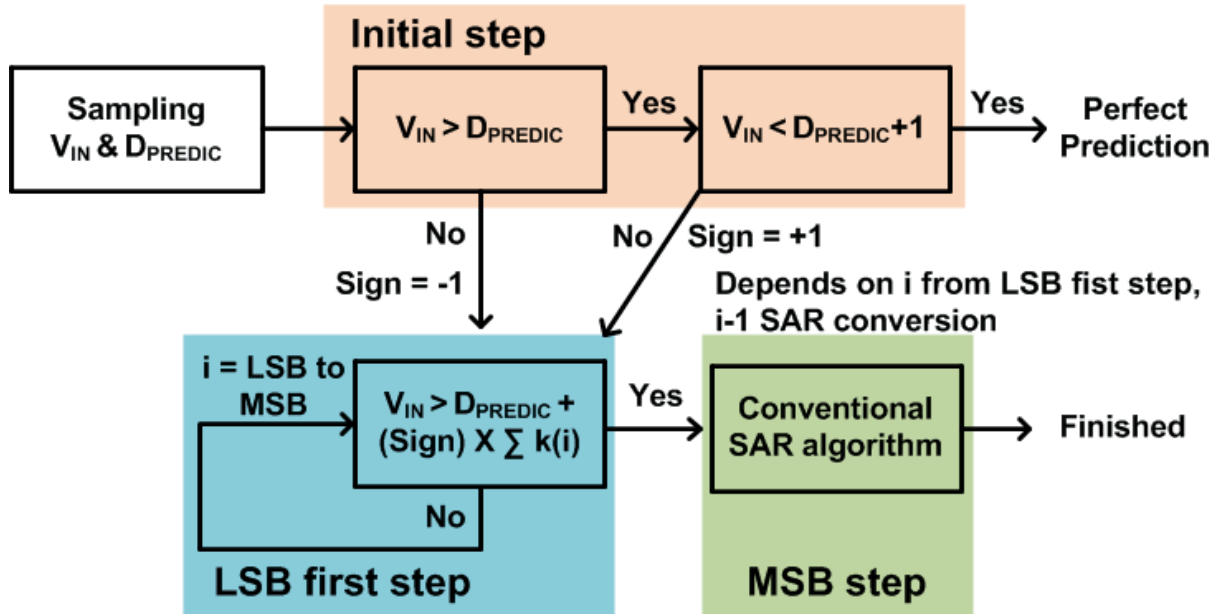
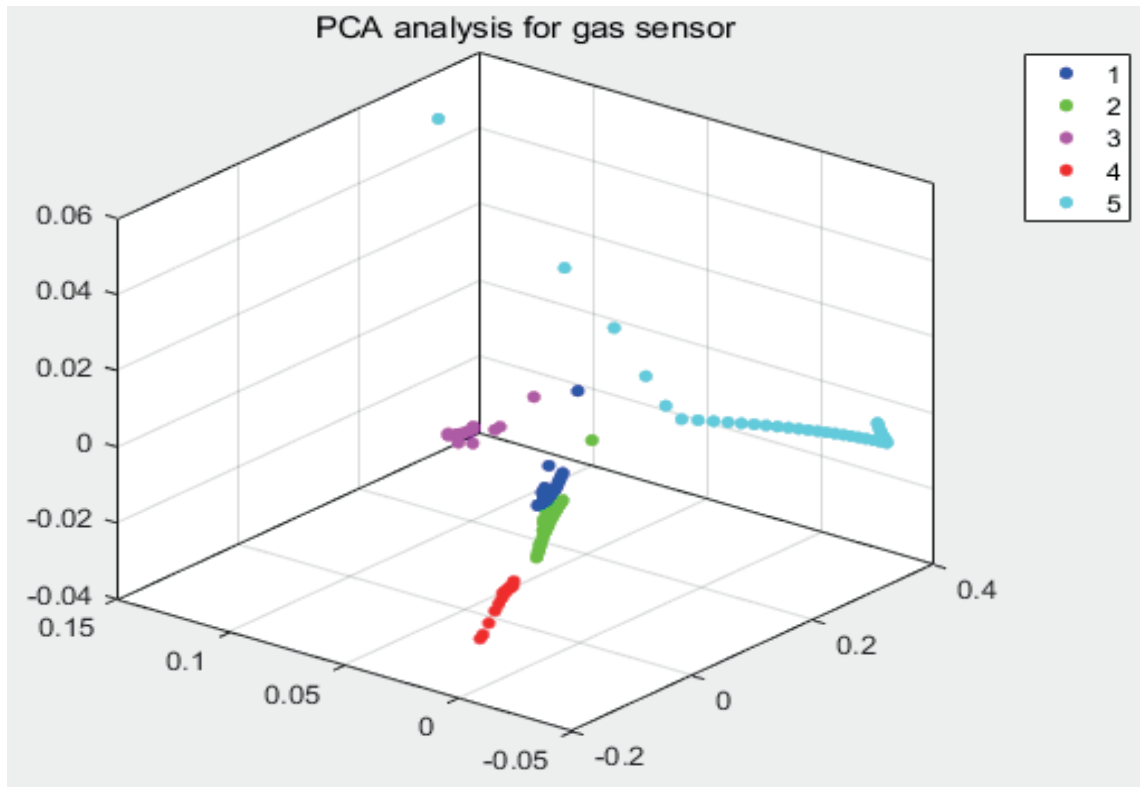


Fig. 47. ANN-based prediction SAR conversion algorithm.

Since conventional fixed-cycle SAR conversion wastes energy sometimes, the LSB-first algorithm [36] is become a solution of energy efficiency. Previous LSB-first algorithm has partially advantage to the small variation of signals. In the order words, if the signal activity is small, the algorithm provides dramatically effect to the conversion cycle and power consumption. In order to improve the accuracy of the prediction value, the conventional methods such as linear fitting and multi-stage curve fitting have some limitations that its real-time processing is not easy and the accuracy varies depending on signal characteristics. The prediction algorithm with ANN can support the real-time prediction based on last digital output code. The ANN was trained by utilizing last five samples, where the weights and the bias of the hidden layer was updated. Thus, this prediction-based algorithm is more powerful with various input signal and more robust with input fluctuations. For the learning step, the accumulated digital code of SAR ADC is utilized to analyze the inherent output characteristics such as input frequency, signal's amplitude, conversion rate, and random external effects from the environment. The prediction value ( $D_{\text{PREDIC}}$ ) is well defined after enough accumulations and training process. And then the conversion cycle is reduced into minimal 2-cycle conversion. Data is analyzed using MATLAB by connecting with PC through Bluetooth communication module for data transmission. Also, the next

prediction is generated according to the updated data in real time and transmitted to the chip, so that the next ADC conversion is performed.

### 3.4.4 Pattern recognition



**Fig. 48.** Principle component analysis without artificial neural network.

Conventionally, gas sensors are classified by only principle component analysis (PCA) analysis. However, the method is hard to distinguish the gas types as shown in Figure 48. 1 and 2 are CO and H<sub>2</sub>, and there is overlapping area. The area causes performance degradation in pattern recognition. Therefore, ANN is providing the more accurate classification and solving the complex variation depending the external condition or parameter.

Figure 49 explains the proposed pattern recognition scheme to improve the selectivity of MEMS gas sensors. Before the neural network computation for pattern recognition, a PCA that kind of a pre-processing is applied with 8-channel gas data. PCA is a method of pre-processing to find the eigenvectors that maximize variance through feature extraction and dimensionality reduction. Therefore, if the variation of gas concentration has great different range, the gas type can be easily found by PCA scheme. The existing gas sensor platform improved the gas selectivity using only PCA, but it has a

limitation because of the difficulty to detect the correct gas type when there is a small variation in a concentration. However, the neural network algorithm can learn a pre-processed gas data and can distinguish different gas type even if it has a small change. The neural network process is divided in two steps, the training part and the decision part. First, in the training process the training data for the input and the gas type for the results is given to the network and the hidden layer try to calculate the optimal weight and the offset in order to distinguish the different gas type. After this step, the neural network has an optimal threshold to decide the different gas type when the gas signal is given to the input. The variation of the weigh and the offset depend on the amount of the training data and the repetition of the training process. Finally, when the hidden layer is set with the optimal value, the neural network is able to determine the gas type which was difficult when using only the PCA.

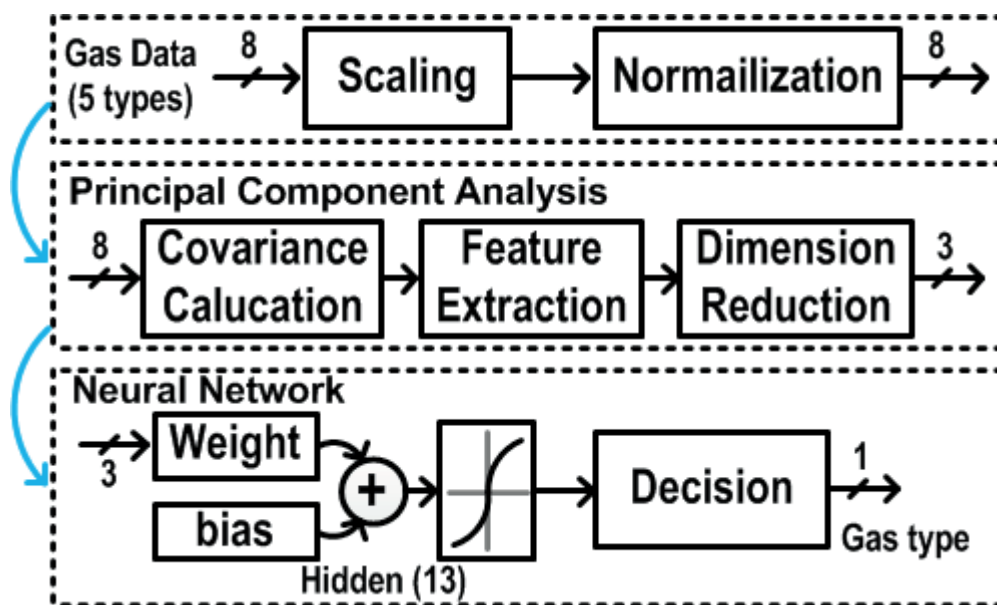


Fig. 49. Proposed pattern recognition with artificial neural network.

## **Chapter IV**

### **Experimental results**

To verify the proposed circuits and schemes, a gas monitoring system prototype was implemented including an adaptive ROIC in a 180 nm CMOS process. Real-time gas monitoring supports through smartphone application with Bluetooth communication. Any devices that have Bluetooth connectivity can monitor the gas concentration and types. Furthermore, the proposed pattern recognition is utilized this wireless interface. The performance of dual-mode ROIC and the system efficiency with real-gas injection are verified in this Chapter IV.

## 4.1 System prototype

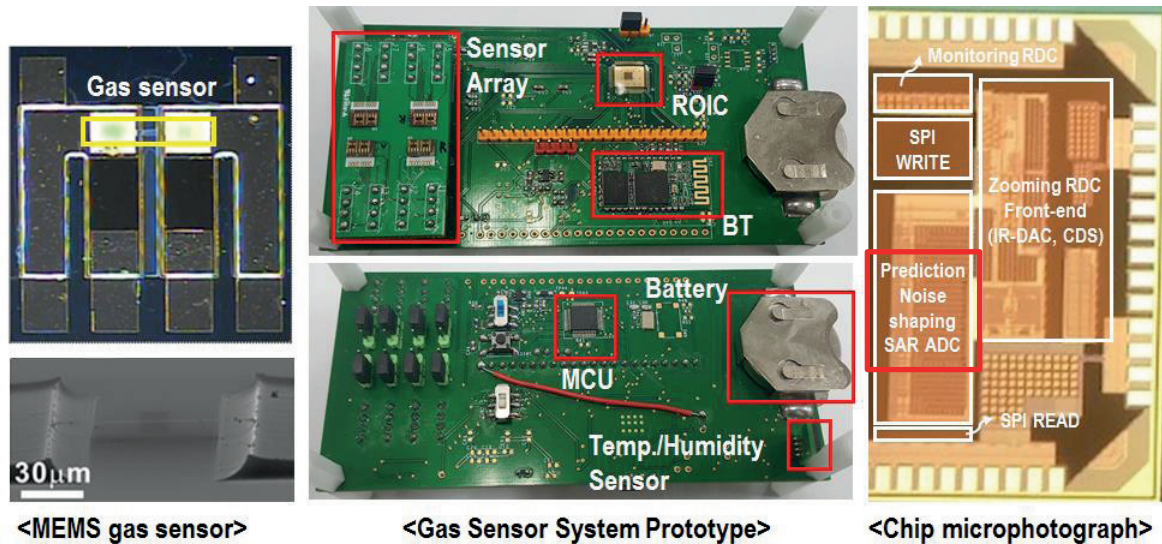


**Fig. 50.** Gas monitoring system prototype and microphotographs of the designed ROIC.

Figure 50 presents proposed gas monitoring system prototype and microphotographs of the designed ROIC. The dual-mode ROIC was implemented including monitoring RDC, zooming RDC, CDS, prediction SAR ADC, and serial peripheral interface (SPI) write/read. The dual-mode operation and functionality of whole chip are controlled by SPI write and digital output is connected by SPI read with MCU. The SPI read converts the parallel data to serial data. The pads of chip are reduced along the parallel 16bit to serial 1bit. The core area of the ROIC is 0.9 mm x 1.3 mm.

A system-level prototype module was implemented in 11.8 cm x 5.7 cm and it includes a MCU, a Bluetooth module, MEMS gas sensors, and two coin batteries. The overall chip and module operation is controlled by MCU and wireless connectivity is supported by Bluetooth module. The embedded batteries give a portability and installation anywhere. 8-channel resistive MEMS-based gas sensor devices are designed to be 5.05 mm x 3.95 mm per two sensors. 8-gas sensors are bonded on the sub-board with several pin header and it has a comfortable for other gas sensors replacement.

The monitoring mode gave low-power operation of 2.95  $\mu$ W, and the precision mode provided 16-bit accuracy through the front-end circuits, the proposed CDS-zooming and the SAR ADC, which is comparable to that of conventional gas sensor systems with sigma-delta ADCs. The energy per

conversion of the proposed system is more efficient than conventional systems [37]. This multi-mode gas sensor system was implemented to support a real-time mobile interface, where real-time gas monitoring results are displayed on a smartphone application that based on Android as shown in Figure 51.

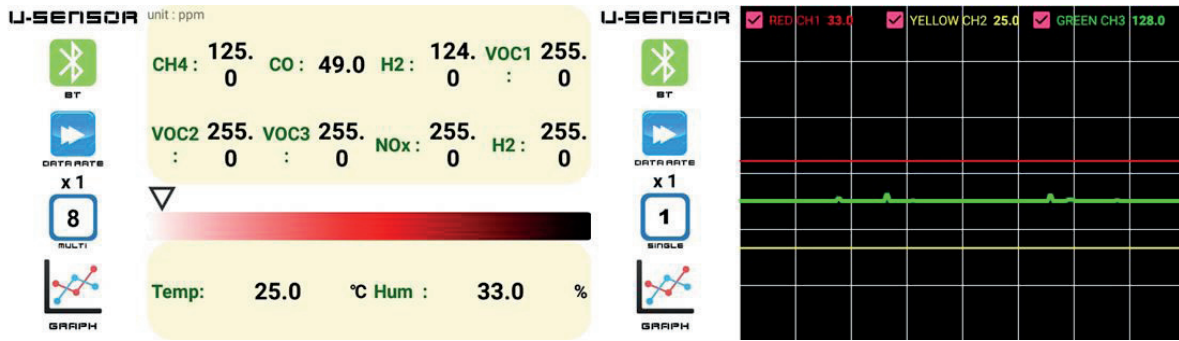
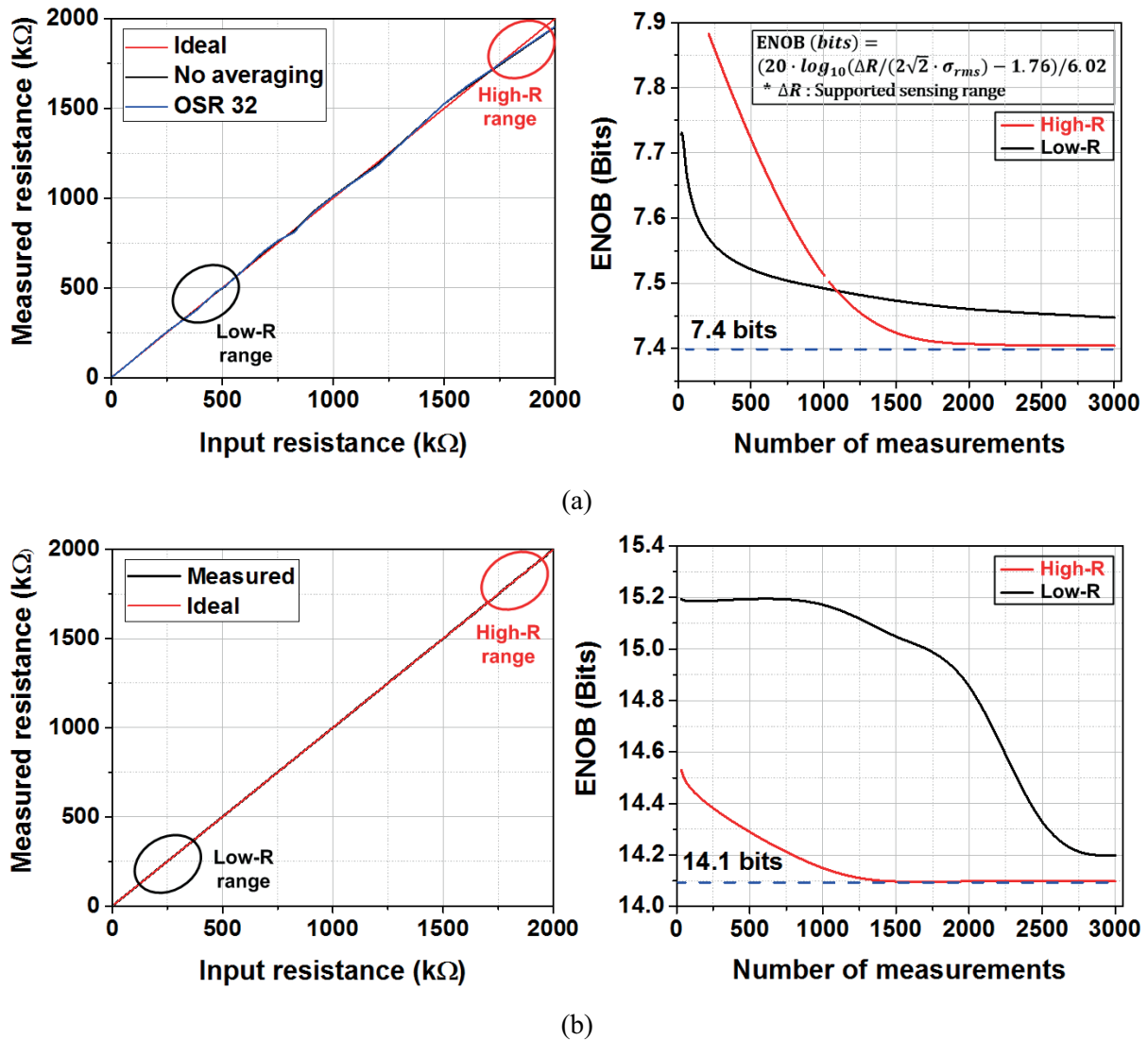


Fig. 51. Real-time monitoring in smart phone.

## 4.2 Dual-mode ROIC performance



**Fig. 52.** The range and accuracy of proposed dual-mode ROIC : (a) monitoring mode and (b) precision mode.

The conventional method to evaluate the measurement error [2, 32] is to utilize high-precision external resistors. However, higher-precision measurement error is not easy to be evaluated by utilizing external resistors, this work adopted the high-precision measurement method where the standard deviation of the ROIC output bit-stream is measured and translated into an equivalent rms noise level.



Another conventional method [38] is utilized to evaluate high-precision measurement. According to this high-precision measurement method, the ENOB becomes

$$\text{ENOB (bits)} = (20 \cdot \log_{10} \left( \frac{\Delta R}{2\sqrt{2}\sigma_{rms}} \right) - 1.76) / 6.02 \quad (4.1)$$

where  $\Delta R$  is the supported sensing range and  $\sigma_{rms}$  is standard deviation from the ROIC's digital output bit-streams. In this work, sufficient measurement samples over 2500 ROIC output data were accumulated for reasonable evaluation to consider various time-varying environmental noises. The accumulated measured ENOBs of the monitoring mode and the precision mode are settled to 7.4 bits and 14.1 bits, respectively. These measurements for the accumulated ENOB were performed with single sensor resistance in two sensor resistances. Their results are shown into Figure. 52 (a) and (b).

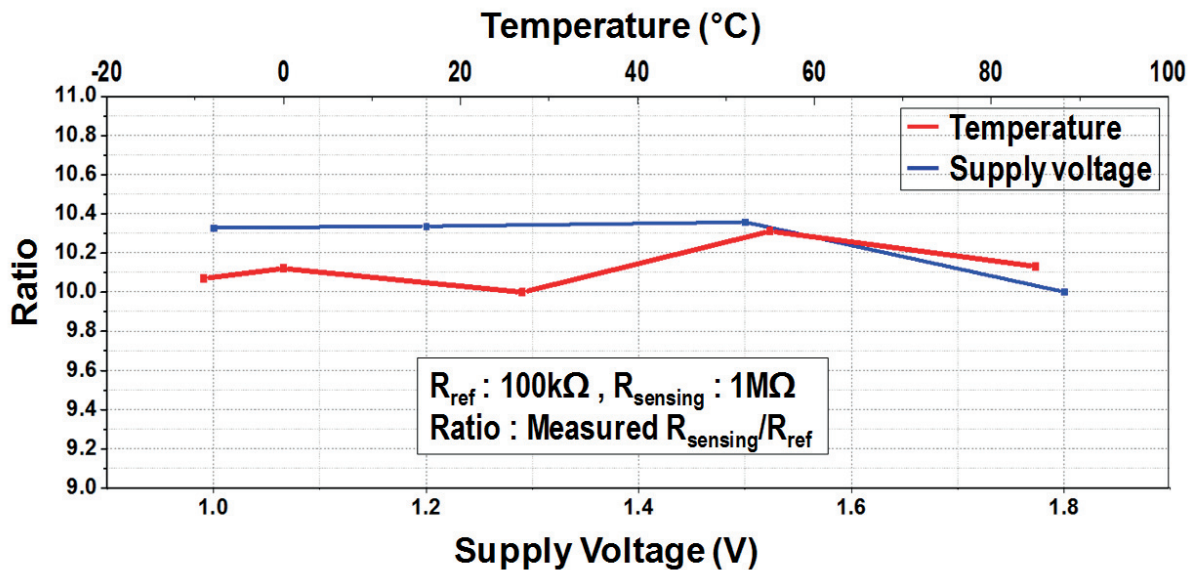


**Fig. 53.** Voltage and temperature characteristics in monitoring mode.

Figure 53 presents the robustness characteristics against voltage and temperature variation in monitoring mode. The ratio between the reference resistance and sensing resistance was kept below 0.36 when the voltage changed from 1.0 V to 1.8V and temperature varied from -9 to 85 degrees Celsius.

The monitoring mode is immune to the variation of voltage and temperature due to inherent characteristics that ratio conversion.

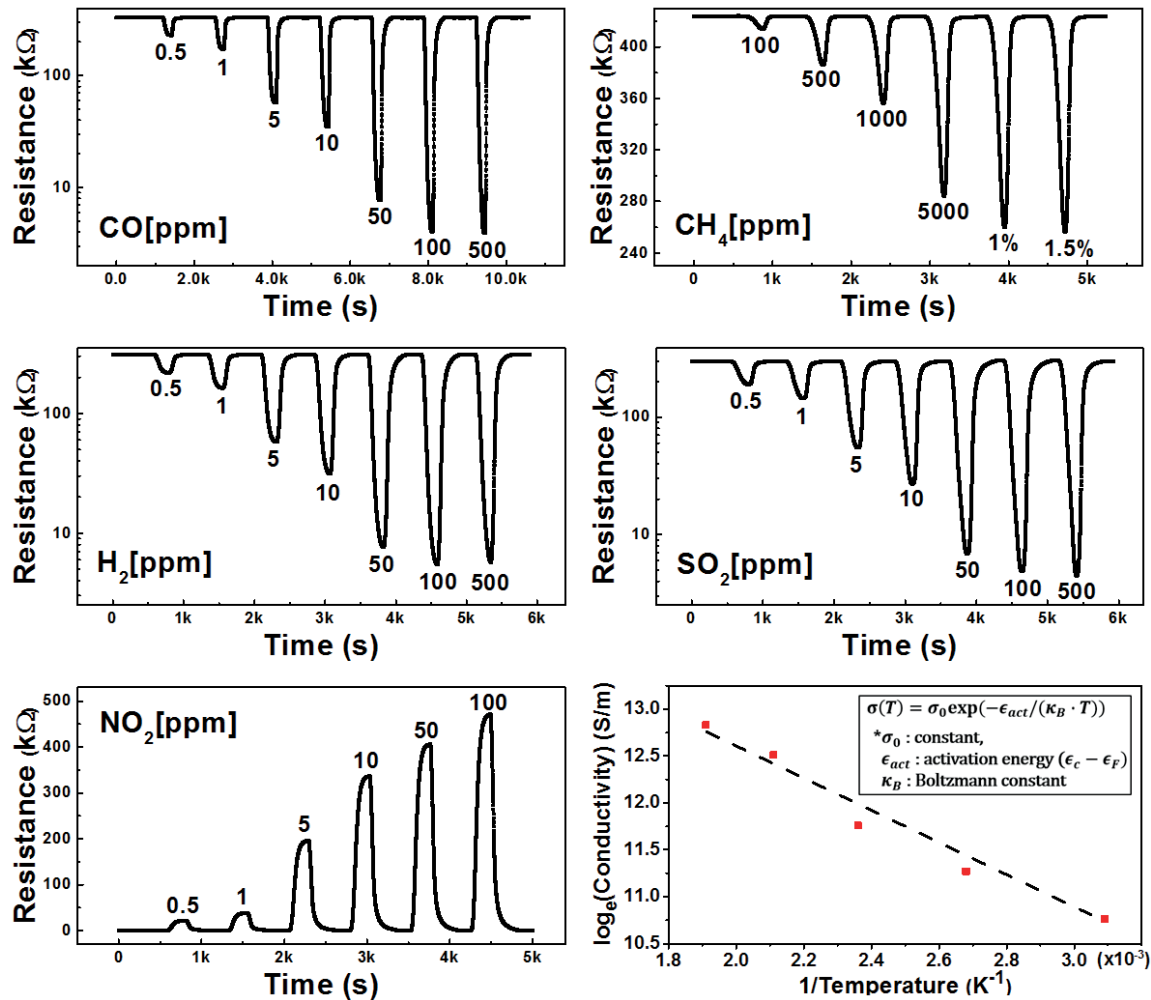


Fig. 54. MEMS sensors' characteristics measurements with five types of hazardous gases and temperature variation.

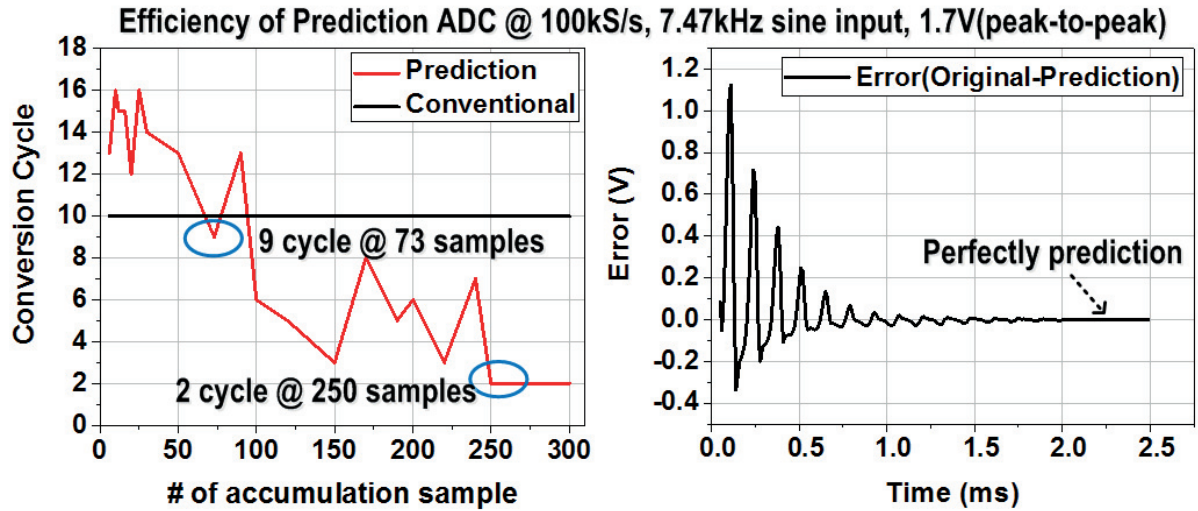
The MEMS gas sensor has two different types of nanowires such as zinc oxide (ZnO) and copper oxide (CuO). In the case of the CuO sensor, it only reacts with SO<sub>2</sub> and CH<sub>4</sub>, but the ZnO sensor reacts to all the five gases. When eight sensor arrays are composed of two kind of nanowire of ZnO and CuO, the different reaction of each channel is used as an index to gauge the gas type. This index can increase the accuracy of the pattern recognition in the post-processing.

Figure 54 shows the gas concentration measurement using the ZnO-nanowire gas sensor. The MEMS gas-sensor resistance is changed by reacting the gases with sensor's substances. The chemical phenomenon is oxidation-reduction reaction. The sensor has different reaction depending on each gas types and then the resistance variation is direct or inverse proportion to the gas concentration. This MEMS gas sensor experiences its characteristic variations due to external environmental changes. In the designed suspended MEMS gas sensor, its sensor resistance reduces with respect to temperature. The electrical properties are explained by a hopping-based mechanism at low temperature and a thermally activated mechanism at higher temperature. Conductivity-temperature relationship of the suspended MEMS gas sensor is defined following equation as:

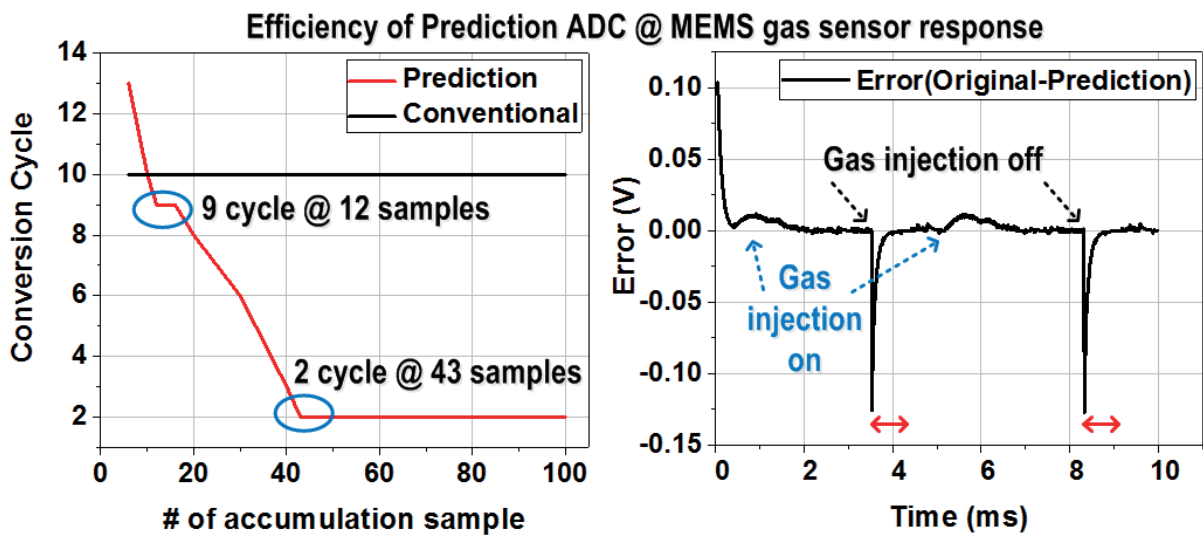
$$\sigma(T) = \sigma_0 \exp\left(-\frac{\epsilon_{act}}{\kappa_B \cdot T}\right) \quad (4.2)$$

where  $\sigma_0$  is a constant,  $\epsilon_{act}$  is the activation energy from the difference the conduction band edge and Fermi level, and  $\kappa_B$  is Boltzmann constant. The measured characteristic of sensor resistance over temperature was appended into Figure 54.

### 4.3 Prediction SAR algorithm with gas injection



(a)



(b)

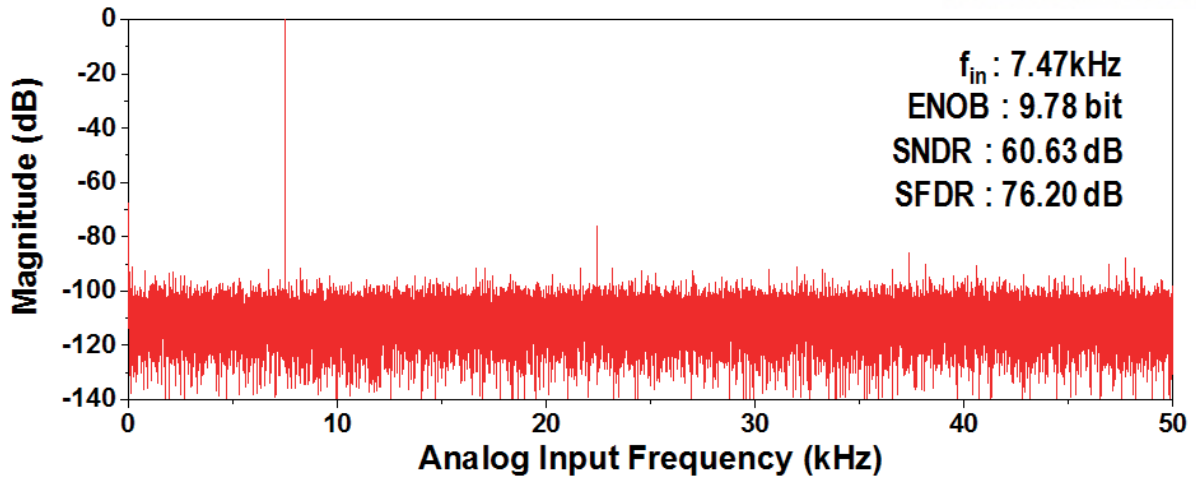
**Fig. 55.** Efficiency of prediction-based SAR ADC and error with (a) sine input and (b) CO-gas sensor input.

The conventional methods such as linear fitting and multi-stage curve fitting have some limitations that its real-time processing is not easy and the accuracy varies depending on signal characteristics. The prediction algorithm with ANN can support the real-time prediction based on last digital output code.

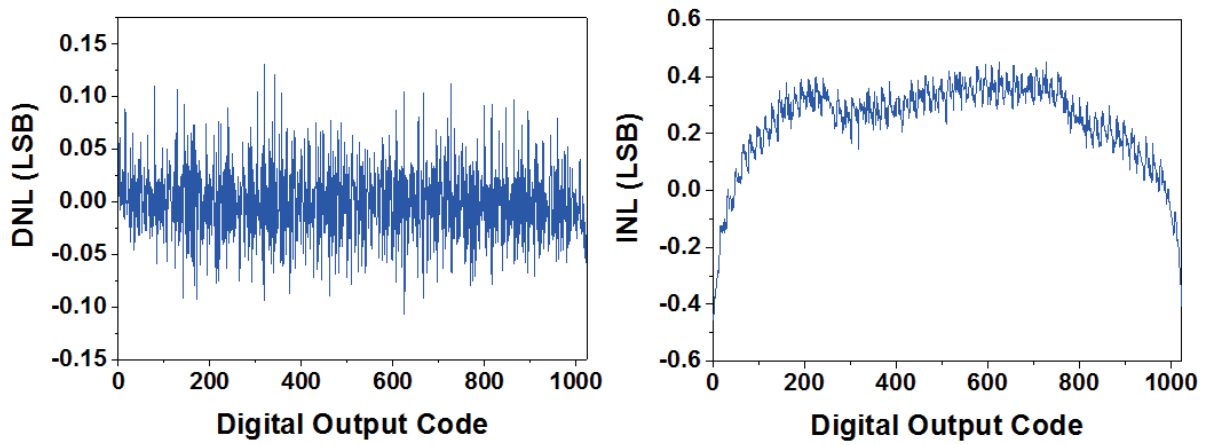
The ANN was trained by utilizing last five samples, where the weights and the bias of the hidden layer was updated. Thus, this prediction-based algorithm is more powerful with various input signal and more robust with input fluctuations. The Figure 55 (a) is shown that 1.7 V peak-to-peak, 7.47kHz sine input are applied in the proposed SAR ADC and verified efficiency with prediction algorithm.

The predictive algorithm should work with real sensor data. Therefore, the measurement and verification of the prediction-based SAR ADC operation with real-gas injection were presented as Figure 55 (b), where transient CO gas injections were performed repeatedly to evaluate its effectiveness. While previous result with sinusoidal inputs took 250 samples for the conversion time to settle into two cycles, new experiment with real sensors data resulted in 43 cycles for the settling. When the CO gas density was abruptly changed, the conversion time increased to 13 cycles instantly. But, after 13-sample accumulation, it reduced below 9 cycles, and then it continuously reduced to two cycles after 43 samples. This prediction-based SAR ADC scheme was proposed to support gas-monitoring applications where gas densities and air compositions changes or diffuses relatively very slowly. Depending on environment conditions or sensing patterns, the initial settling time is required for settling of the conversion time, and then fast conversion performance can be provided. If the gas density changes slowly, earlier settling would be achieved. Therefore, we believe that this prediction-based scheme could improve the effectiveness of the overall system performances meaningfully, considering inherent slow-varying characteristic of gas monitoring systems.

Figure 56 presents prediction SAR ADC and its specification. The prediction ADC operates normally at 100kS/s and the spectrum for sine input 7.47kHz is confirmed. SNDR, ENOB and SFDR were achieved 60.63 dB, 9.78 bits and 76.20 dB respectively. The measured DNL and INL were  $-0.11$  to  $0.13$  LSB and  $-0.45$  to  $0.45$  LSB, respectively. The area of the ADC is  $0.36 \text{ mm}^2$ , the comparator and C-DAC are consumed 0.28 mW, and the digital blocks as logic, clock generator, buffer and etc. consume 0.52 mW. By utilizing fully-differential CDS-zooming circuits, overall effective system resolution was improved to be around 16-bits (10-bit ADC + 6-bit CDS zooming).



(a)



(b)

Fig. 56. Measured characteristics of prediction-based SAR ADC: (a) spectrum analysis and (b) DNL/INL.

#### 4.4 Pattern recognition with artificial neural network

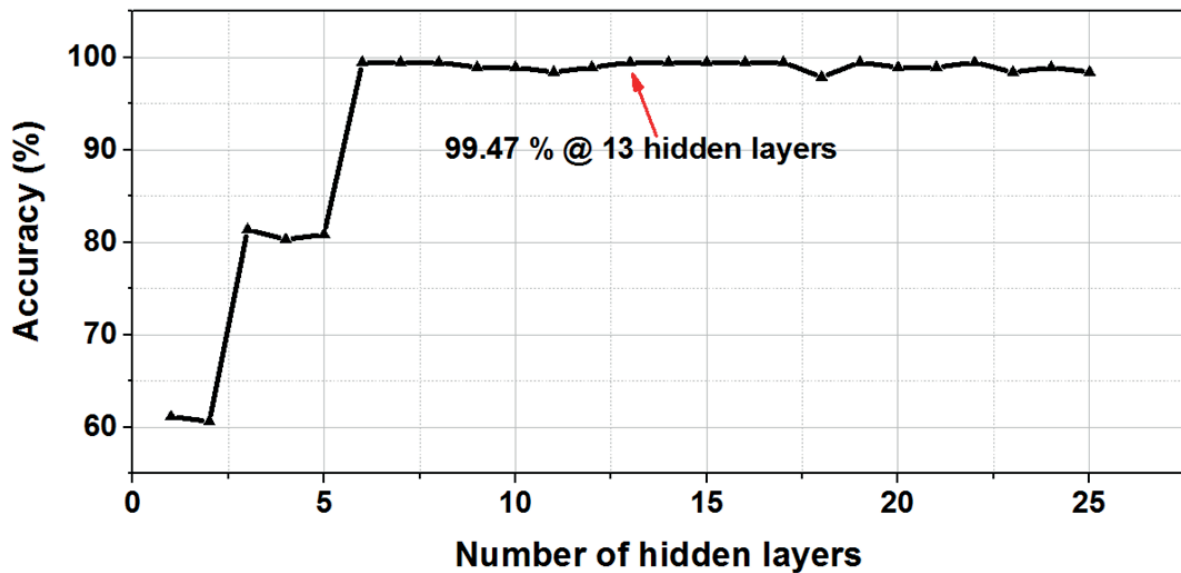


Fig. 57. Confusion matrix in training step of pattern recognition.

This work utilized in-house MEMS devices for IoT gas-sensor devices. The MEMS-based gas sensors have inherent characteristic advantages that are small size, low-power consumption, and multi-gas sensing capability. However, their disadvantage is poor selectivity so that it needs to be supplemented to improve recognition capability on various gas kinds. Conventionally, the PCA is utilized to figure out the gas type and its concentration, but it shows limited performances in terms of

the precision and the real-time monitoring capability.

Therefore, this paper suggests the pattern-recognition method through the ANN that is also augmented by the PCA. For classification of the gas type and concentration, test samples containing gas-composition information are necessary for training the ANN engine. For this purpose, 251 test samples were gathered, and new experiments were performed to verify the sensor system prototype in seen as Figure 57 251 gas sensing data prepare from 8 MEMS gas sensors. The concentration was changed from 0.5 ppm to 100 ppm for CO, H<sub>2</sub>, and SO<sub>2</sub>. NO<sub>2</sub> was measured to have the concentration from 0.5 ppm to 50 ppm and CH<sub>4</sub> was measured from 100 ppm to 10,000 ppm.



**Fig. 58.** Optimization procedure of the number of hidden layers.

During the training step, optimization procedure is needed for the improvement of pattern recognition’s accuracy. One hundred eighty-eight data excluding previous training data were utilized to optimize the number of hidden layers. The gas types and concentration were well recognized as seen in Figure 58. Therefore, the proposed pattern recognition was verified 99.47 % accuracy with 13 hidden layers provided.



## 4.5 Summary

TABLE II. PERFORMANCE SUMMARY AND COMPARISON WITH RECENT WORKS

	This Work	[2]	[32]	[39]	[37]
Technology ( $\mu\text{m}$ )	0.18	0.18	0.13	0.16	0.35
Wireless interface	Smart Phone / PC	Not available	Not available	Not available	Smart phone / PC
Supply Voltage (V)	1.8 / 1.0	1.2 / 0.6	0.5	1.8	3.0
Readout-Method	R-to-F / R-to-V (dual)	R-to-V (current)	R-to-V (CDS)	R-to-V (TC)	R-to-V (current)
Input range ( $\Omega$ )	250 – 2M (Monitoring) 8k – 2M (precision)	10k – 10M	23k – 4.6M	500 – 9000 ppm (CO <sub>2</sub> )	1M – 10M
Effective number of bits (ENOB) (bits)	7.4 (Monitoring) 14.1 (Precision)	10 (ADC resolution)	11.2	15.3	9.4
Conversion rate (kS/s)	100 (Maximum 1MS/s)	1.2	1	-	100
Power consumption	2.95 $\mu\text{W}$ (Monitoring) 2.51mW–2.61mW (Precision)	1.7 $\mu\text{W}$	11.3 $\mu\text{W}$	0.4mW	0.93mW
Figure-of-Merit (pJ/Conv. step)	0.53 (Monitoring) 1.43–1.49 (Precision)	1.39	4.8	-	13.77
Chip Area (mm <sup>2</sup> )	1.17	1.32	2.8	0.7	12.05

The precision mode including the predictive SAR ADC was characterized to give the ranged performance from the best case to the worst case, since the conversion cycle varies depending on the prediction result. Since the prediction-based SAR ADC can be programmed to work like the conventional SAR ADC, the worst-case performance becomes similar to that of the conventional SAR ADC. Additionally, the computation power consumption in Matlab was not considered in this work because the prediction algorithm is occasionally executed when its prediction error becomes larger than a critical value. Furthermore, the comparison index of the energy per conversion was re-defined to include the resolution, and it was replaced with the conventional ADC figure-of-merit ( $\text{FOM} = \text{Power}/2^{\text{ENOB}} \cdot \text{F}_s$ ). Following these modified comparisons, the worst-case performance of the precision

mode became similar with a recent record [2], and the monitoring mode gave 2.6 times better FOM.

## Chapter V

### Conclusion

This doctoral dissertation describes energy efficient gas monitoring system. Also, it presents the synergies that can be achieved by combining artificial intelligence computation with a readout integrated circuit, along with the development of sensors and communication technologies. As IoT technology is growth, more sensors can be integrated in the system and communication functions will continue to grow, so extensive data can be accumulated and applied in various fields. Learning-based scheme with sensor data is utilized to improve the overall efficiency and can perform evolved functionality of the system. In order to enhance the expeditious operation, the suitable ROIC was fabricated with adaptive mode control, pattern recognition and prediction SAR algorithm. Firstly, the control of dual-mode which consist of low-power or high-resolution mode can be tailored to the situation and the sensor system can be modified to increase overall system efficiency. The design specification of high-performance ADC can be also effectively attenuated using CDS zooming while maintaining high resolution of the system. Secondly, machine learning technique is possible to distinguish the type of gas and concentration based on the learned data and multi-channel interface. Third, by predicting the conversion results of the previous sample, the conversion cycle of the SAR ADC can be reduced to 2 cycles at maximum and power saving is possible.

Furthermore, other types of ADCs and sensor interfaces can be studied and used in a more developed form in order to increase the efficiency of the system. The conjunction with chip and artificial neural network can be extended future research area.

## REFERENCES

1. A. Zanella, N. Bui, A. Castellani, L. Vangelista and M. Zorzi, "Internet of Things for Smart Cities," in *IEEE Internet of Things Journal*, vol. 1, no. 1, pp. 22-32, Feb. 2014.
2. M. Choi, J. Gu, D. Blaauw, and D. Sylvester, "Wide Input Range 1.7 $\mu$ W 1.2kS/s Resistive Sensor Interface Circuit with 1 cycle/sample Logarithmic Sub-Ranging," *IEEE symp. VLSI Circuits*, pp. C330-C331, Jun. 2015.
3. B. Li, L. Sun, C. Ko, A. K. Wong and K. Pun, "A High-Linearity Capacitance-to-Digital Converter Suppressing Charge Errors From Bottom-Plate Switches," in *IEEE Transactions on Circuits and Systems I: Regular Papers*, vol. 61, no. 7, pp. 1928-1941, July 2014.
4. Biosystems, Appl. Note AN20010827, pp 1-1.
5. P. F. Wambach, "Variation in Exposure Levels for High Hazard Frequently Monitored Agents," *AIHA Journal*, vol 63, pp.424-429, Jun. 2010.
6. N. Ramgir, et al, "Metal oxide nanowires for chemiresistive gas sensors: Issues, challenges and prospects," *Colloids and Surfaces A : Physicochem. Eng. Aspects*, vol. 39, pp. 101-116, Dec 2013.
7. K. Park, et al., "A Reconfigurable Readout Integrated Circuit for Heterogenous Display-Based Multi-Sensor System," *Sensors*, vol. 17, no. 4, pp. 759-771, Apr 2017.
8. H.-S. Kim, et al., "High-SNR capacitive multi-touch sensing technique for AMOLED display panels," *IEEE Sensors Journal*, vol. 16, no. 4, pp. 859-860, Feb 2016.
9. K. Kwon, et al., "A fully-differential correlated double sampling readout circuit for mutual-capacitance touch screens," *J. Semicond. Technol. Sci.*, vol. 15, no. 3, pp 349-355, Jun 2015.
10. M. Yusefpor, et al., "Fingerprint Sensor in an Electronic Device," U.S. Patent Application No 15/451, 076; U.S. Patent Publication No 2015/0036065 A1, 5, Feb 2015.
11. U. G Kyle, et al., "Bioelectrical impedance analysis—Part I: Review of principles and methods," *Clin. Nutr.* 2004, 23, 1226–1243.
12. J. Park, D. Lim and D. Jeong, "A Reconfigurable 40-to-67 dB SNR, 50-to-6400 Hz Frame-Rate, Column-Parallel Readout IC for Capacitive Touch-Screen Panels," in *IEEE Journal of Solid-State Circuits*, vol. 49, no. 10, pp. 2305-2318, Oct. 2014.

13. N. Van Helleputte et al., "A 345  $\mu$ W Multi-Sensor Biomedical SoC With Bio-Impedance, 3-Channel ECG, Motion Artifact Reduction, and Integrated DSP," in *IEEE Journal of Solid-State Circuits*, vol. 50, no. 1, pp. 230-244, Jan. 2015.
14. Y. He, Z. Chang, L. Pakula, S. H. Shalmany and M. Pertijs, "27.7 A 0.05mm<sup>2</sup> 1V capacitance-to-digital converter based on period modulation," *2015 IEEE International Solid-State Circuits Conference - (ISSCC) Digest of Technical Papers*, San Francisco, CA, 2015, pp. 1-3.
15. C. Chan et al., "A 0.011mm<sup>2</sup> 60dB SNDR 100MS/s reference error calibrated SAR ADC with 3pF decoupling capacitance for reference voltages," *2016 IEEE Asian Solid-State Circuits Conference (A-SSCC)*, Toyama, 2016, pp. 145-148.
16. J. Tsai et al., "A 0.003 mm<sup>2</sup> 10 b 240 MS/s 0.7 mW SAR ADC in 28 nm CMOS With Digital Error Correction and Correlated-Reversed Switching," in *IEEE Journal of Solid-State Circuits*, vol. 50, no. 6, pp. 1382-1398, June 2015.
17. K. Park, C. Park, J. J. Kim, "A 4b/cycle flash-assisted SAR ADC with comparator speed-boosting technique," *Journal of Semiconductor Technology and Science*, Vol. 18, No. 2, pp. 281-286, April, 2018.
18. W. Kim, et al., "A 0.6 V 12 b 10 MS/s Low-Noise Asynchronous SAR-Assisted Time-Interleaved SAR (SARTI-SAR) ADC," *IEEE J. Solid State Circuits*, vol. 51, no. 8, pp. 1826-1839, Jun 2016.
19. Y. Chen, et al., "Split capacitor DAC mismatch calibration in successive approximation ADC," *Custom Integrated Circuits Conference*, pp. 279-282, Sep 2009.
20. R. Xu, et al., "Digitally Calibrated 768-kS/s 10-b Minimum-size SAR ADC Array With Dithering," *IEEE J. Solid State Circuits*, vol. 47, no. 9, pp. 2129-2140, Sep 2012.
21. B.-R.-S. Sung, et al., "A 6 bit 2 GS/s flash-assisted time-interleaved (FATI) SAR ADC with background offset calibration," *A-SSCC*, pp. 281-284, Nov 2013.
22. Z. Zhu, et al., "V<sub>cm</sub>-based monotonic capacitor switching scheme for SAR ADC," *Electronics Letters*, vol. 49, no. 5, pp. 327-329, Feb 2013.
23. Y. Zhang, et al., "Energy-efficient switching method for SAR ADCs with bottom plate sampling," *Electronics Letters*, vol. 52, no. 9, pp. 690-692, Apr 2016.
24. J. A. Fredenburg, et al., "A 90-MS/s 11-MHz-Bandwidth 62-dB SNDR Noise-Shaping SAR ADC,"

- IEEE J. Solid State Circuits*, vol. 47, no. 12, pp. 2898-2904, Dec 2012.
25. X. Liu, S. Cheng, H. Liu, S. Hu, D. Zhang, and H. Ning, "A Survey on Gas Sensing Technology," *Sensors*, vol. 12, no. 7, pp. 9635–9665, Jul. 2012.
  26. Y. Cai, H. Gao, B. tong, et al., "Measurement of trace ethane using a mid-IR LED," in Proc. *IEEE 6th Int. Conf. Photon. (ICP)*, pp. 1-3, Mar. 2016.
  27. S. Manchukutty, N. J. Vasa, et al., "Dual Photoionization Source-Based Differential Mobility Sensor for Trace Gas Detection in Human Breath," *IEEE Sensors Journal*, vol. 15, no. 9, pp. 4899-4904, Sep. 2015.
  28. J. B. Miller, "Catalytic Sensors for Monitoring Explosive Atmospheres," *IEEE Sensors Journal*, vol. 1, no. 1, pp. 88-93, Jun. 2001.
  29. H. Wan, H. Yin, L. Lin, et al., "Miniaturized planar room temperature ionic liquid electrochemical gas sensor for rapid multiple gas pollutants monitoring," *Sensors and Actuators B: Chemical*, vol. 255, pp. 638-646, Feb. 2018.
  30. Y. Lim, et al., "Monolithic carbon structures including suspended single nanowires and nanomeshes as a sensor platform." *Nanoscale Research Letters*, vol. 8, Nov. 2013.
  31. C. C. Enz, et al., "Circuit techniques for reducing the effects of op-amp imperfections: autozeroing, correlated double sampling, and chopper stabilization," *Proc. IEEE*, vol. 84, no. 11, pp. 1587-1614, Nov 1996.
  32. H. Ha, et al., "A 0.5V, 11.3-  $\mu$ W, 1-kS/s Resistive Sensor Interface Circuit with Correlated Double Sampling," *IEEE Custom Integrated Circuits Conf. (CICC)*, pp. 1–4, Sep 2012.
  33. S. Choi, et al., "A Three-Step Resolution-Reconfigurable Hazardous Multi-Gas Sensor Interface for Wireless Air-Quality Monitoring Applications," *Sensors*, vol. 18, no. 3, pp. 761-773, Mar 2018.
  34. Crystal Market Research, Global Gas Sensors Market is Estimated to Reach \$3.40 Billion by 2022. Available: <https://globenewswire.com/news-release/2017/11/03/1174502/0/en/Global-Gas-Sensors-Market-is-Estimated-to-Reach-3-40-Billion-by-2022-Says-Crystal-Market-Research.html>
  35. V. Ramya, et al., "Embedded system for Hazardous Gas detection and Alerting," *International Journal of Distributed and Parallel System*, vol. 3, no. 3, pp. 287-300, May 2012.
  36. F. M. Yaul, et al., "A 10 bit SAR ADC With Data-Dependent Energy Reduction Using LSB-First

Successive Approximation,' *IEEE J. Solid-State Circuits*, vol. 49, no. 12, pp. 2825-2834, Dec 2014.

37. T.-H. Tzeng, et al., "A Portable Micro Gas Chromatography System for Volatile Compounds Detection with 15ppb of Sensitivity," *ISSCC Dig. Tech. Papers*, pp.388-390, Feb. 2015.

38. R. Yang, et al., "A Precision Capacitance-to-Digital Converter With 16.7-bit ENOB and 7.5-ppm/°C Thermal Drift," *IEEE J. Solid-State Circuits*, vol. 52, no. 11, pp. 3018-3031, Nov. 2017.

39. Z. Cai, et al., "A Ratiometric Readout Circuit for Termal-Conductivity-Based Resistive CO<sub>2</sub> Sensors," *IEEE J. Solid-State Circuits*, vol. 51, no. 10, pp. 2463-2474, Oct. 2016.

## ACKNOWLEDGEMENTS

I would like to thank my advisor Prof. Jae Joon Kim, who has been a highly respectable person and mentor. When faced with difficulties in my research, he always encouraged and gave a lot of help to my research with logical thinking and instructions. I would also like to thank prof. Yunsik Lee, Prof. Heungjoo Shin, Prof. Jeong Min Baik and Prof. Hoon Eui Jeong for their advice and critical feedback. Their wide perspectives have help me to strengthen my research.

Thank you to Subin and Hee Young who discussed and shared their thinking with me. Thank you to Chan Sam who helped me a lot. I am also very thankful to the members of my laboratory, Sung-Woo, Kwang Muk, Byungjoo, Myeong Woo, Jun Young, Jeonghoon and Hyun Joong. Dong-Uk, Kihyun, Dae-Woong, Seung Mok and Jong Gyu, who have already graduated, thank you for your help during graduate school.

Especially, I thank my parents for always believing and growing me up. I would also like to thank Hyun Soo, who supporting me.



## CURRICULUM VITAE

### EDUCATION

PhD., Electrical Engineering, Ulsan National Institute of Science and Technology, June 2019

Advisor: Jae Joon Kim

M.S., Electrical Engineering, Ulsan National Institute of Science and Technology, 2015

Advisor: Jae Joon Kim

B.S., Electrical Engineering, Ulsan National Institute of Science and Technology, 2013

### PUBLICATION

1. **K. Park**, S. Choi, H. Y. Chae, C. S. Park, S. Lee, Y. Lim, H. Shin, J. J. Kim, "An Energy-Efficient Multi-Mode Multi-Channel Gas-Sensor System with Learning-Based Optimization and Self-Calibration Schemes," *IEEE Transactions on Industrial Electronics*, doi: 10.1109/TIE.2019.2905819.
2. **K. Park**, S. M. Kim, W.-J. Eom, J. J. Kim, "A Reconfigurable Readout Integrated Circuit for Heterogeneous Display-Based Multi-Sensor Systems," *Sensors*, 17(4), 759; doi:10.3390/s17040759, April, 2017.
3. **K. Park**, C. Park, J. J. Kim, "A 4b/cycle flash-assisted SAR ADC with comparator speed-boosting technique," *Journal of Semiconductor Technology and Science*, Vol. 18, No. 2, pp. 281-286, April, 2018.
4. S. Choi, D. J. Kim, Y. Y. Choi, **K. Park**, S.-W. Kim, S. H. Woo, J. J. Kim, "A Multi-Sensor Mobile Interface for Industrial Environment and Healthcare Monitoring," *IEEE Transactions on Industrial Electronics*, Vol. 64, Issue 3, pp. 2344-2352, March, 2017.
5. W.-J. Eom, S.-W. Kim, **K. Park**, F. Bien, J. J. Kim, "Multi-Purpose Fingerprint Readout Circuit Embedding Physiological Signal Detection," *Journal of Semiconductor Technology and Science*, Vol. 16, No. 6, pp. 793-799, December, 2016.
6. K. Lee, Y. Y. Choi, D. J. Kim, H. Y. Chae, **K. Park**, Y. M. Oh, S. H. Woo, J. J. Kim, "A Wireless ExG Interface for Patch-Type ECG Holter and EMG-Controlled Robot Hand," *Sensors*, 17(8), 1888; doi:10.3390/s17081888, August, 2017.

7. S. Choi, **K. Park**, S. Lee, Y. Lim, B. Oh, H. Y. Chae, C. S. Park, H. Shin, J. J. Kim, "A Three-Step Resolution-Reconfigurable Hazardous Multi-Gas Sensor Interface for Wireless Air-Quality Monitoring Applications," *Sensors*, 18(3), 761; doi:10.3390/s18030761, March, 2018.
8. C. S. Park, J. Jeon, B. Oh, H. Y. Chae, **K. Park**, H. Son, J. J. Kim "A Portable Phase-Domain Magnetic Induction Tomography Transceiver with Phase-Band Auto-Tracking and Frequency-Sweep Capabilities," *Sensors*, 18(11), 3816; doi:10.3390/s18113816, November, 2018.
9. B. Oh, **K. Park**, J. J. Kim, "A Triple-Mode Performance-Optimized Reconfigurable Incremental ADC for Smart Sensor Applications," *IEEE Access*, Vol. 7, pp. 19013-19023; doi:10.1109/access.2019.2896756, January 31th, 2019.